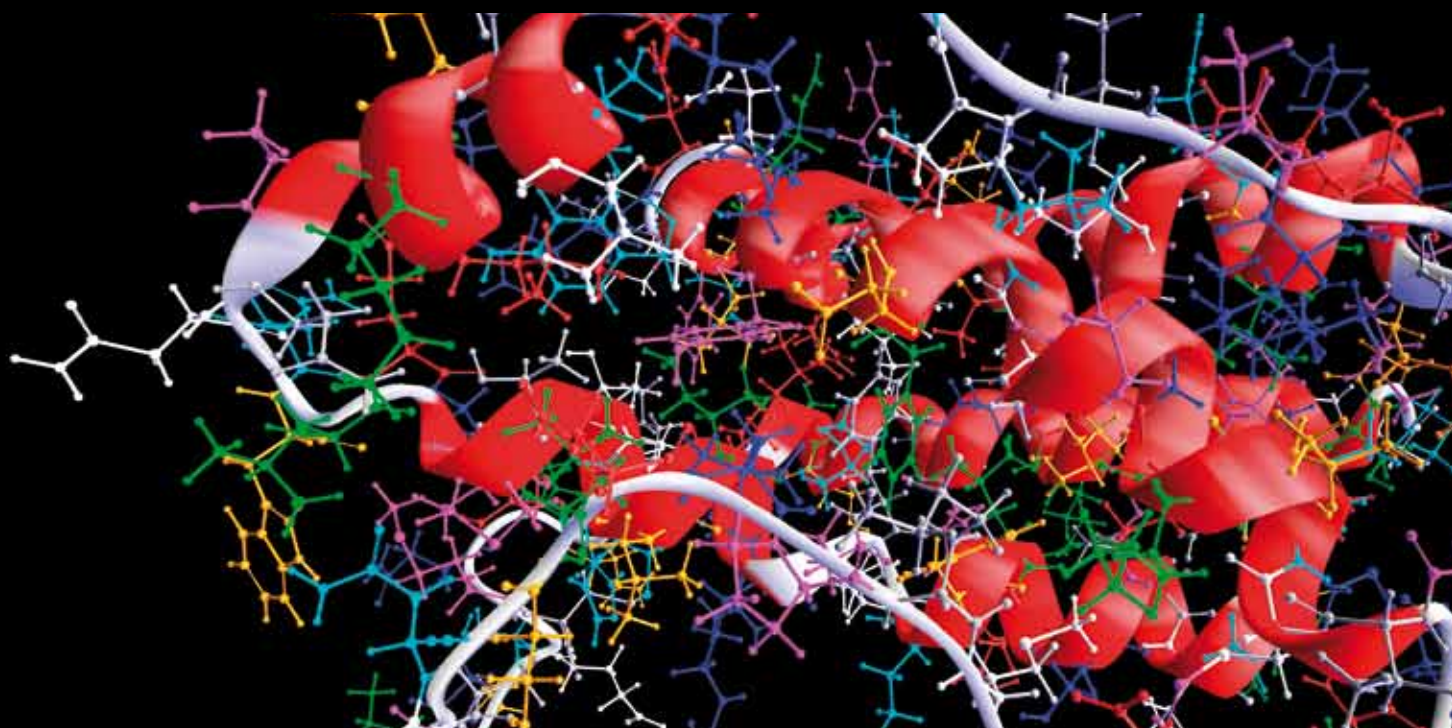


IMMUNE SYSTEM MODELING AND RELATED PATHOLOGIES

GUEST EDITORS: FRANCESCO PAPPALARDO, VLADIMIR BRUSIC, AND HOLGER FRÖHLICH





Immune System Modeling and Related Pathologies

Immune System Modeling and Related Pathologies

Guest Editors: Francesco Pappalardo, Vladimir Brusic,
and Holger Fröhlich



Copyright © 2012 Hindawi Publishing Corporation. All rights reserved.

This is a special issue published in “Computational and Mathematical Methods in Medicine.” All articles are open access articles distributed under the Creative Commons Attribution License, which permits unrestricted use, distribution, and reproduction in any medium, provided the original work is properly cited.

Editorial Board

Zvia Agur, Israel
Emil Alexov, USA
Gary C. An, USA
Georgios Archontis, Cyprus
Pascal Auffinger, France
Facundo Ballester, Spain
Dimos Baltas, Germany
Chris Bauch, Canada
Maxim Bazhenov, USA
Niko Beerenwinkel, Switzerland
Philip Biggin, UK
Michael Breakspear, Australia
Thierry Busso, France
Carlo Cattani, Italy
Bill Crum, UK
Timothy David, New Zealand
Gustavo Deco, Spain
Carmen Domene, UK
Wim Van Drongelen, USA
Frank Emmert-Streib, UK
Ricardo Femat, Mexico
Alfonso T. García-Sosa, Estonia
Kannan Gunasekaran, USA

Damien R. Hall, Japan
William F. Harris, South Africa
Vassily Hatzimanikatis, USA
Tasawar Hayat, Pakistan
Volkhard Helms, Germany
J.-H. S. Hofmeyr, South Africa
Seiya Imoto, Japan
Bleddyn Jones, UK
Lawrence A. Kelley, UK
Lev Klebanov, Czech Republic
Ina Koch, Germany
David Liley, Australia
Quan Long, UK
Yoram Louzoun, Israel
Jianpeng Ma, USA
C.-M. C. Ma, USA
Reinoud Maex, France
Francois Major, Canada
Simeone Marino, USA
Ali Masoudi-Nejad, Iran
Ramit Mehr, Israel
Seth Michelson, USA
Michele Migliore, Italy

Karol Miller, Australia
Ernst Niebur, USA
Kazuhisa Nishizawa, Japan
Martin Nowak, USA
Markus Owen, UK
Hugo Palmans, UK
Lech S. Papiez, USA
Jean Pierre Rospars, France
David James Sherman, France
Sivabal Sivaloganathan, Canada
Elisabeth Tillier, Canada
Nestor V. Torres, Spain
Anna Tramontano, Italy
Nelson J. Trujillo-Barreto, Cuba
Kutlu O. Ulgen, Turkey
Nagarajan Vaidehi, USA
Edelmira Valero, Spain
Jinliang Wang, UK
Jacek Waniewski, Poland
Guang Wu, China
X. George Xu, USA
Henggui Zhang, UK

Contents

Immune System Modeling and Related Pathologies, Francesco Pappalardo, Vladimir Brusic, and Holger Fröhlich
Volume 2012, Article ID 274702, 2 pages

Modeling Innate Immune Response to Early *Mycobacterium* Infection, Rafael V. Carvalho, Jetty Kleijn, Annemarie H. Meijer, and Fons J. Verbeek
Volume 2012, Article ID 790482, 12 pages

Computational Modeling of Microabscess Formation, Alexandre Bittencourt Pigozzo, Gilson Costa Macedo, Rodrigo Weber dos Santos, and Marcelo Lobosco
Volume 2012, Article ID 736394, 16 pages

Time-Course Analysis of Main Markers of Primary Infection in Cats with the Feline Immunodeficiency Virus, B. Ribba, H. El Garch, S. Brunet, E. Grenier, F. Castiglione, H. Poulet, and P. Vanhems
Volume 2012, Article ID 342602, 9 pages

Relaxation Estimation of RMSD in Molecular Dynamics Immunosimulations, Wolfgang Schreiner, Rudolf Karch, Bernhard Knapp, and Nevena Ilieva
Volume 2012, Article ID 173521, 9 pages

How the Interval between Prime and Boost Injection Affects the Immune Response in a Computational Model of the Immune System, F. Castiglione, F. Mantile, P. De Berardinis, and A. Prisco
Volume 2012, Article ID 842329, 9 pages

Understanding Immunology via Engineering Design: The Role of Mathematical Prototyping, David J. Klinke II and Qing Wang
Volume 2012, Article ID 676015, 9 pages

A Mathematical Model of Immune-System-Melanoma Competition, Marzio Pennisi
Volume 2012, Article ID 850754, 13 pages

Editorial

Immune System Modeling and Related Pathologies

Francesco Pappalardo,¹ Vladimir Brusic,² and Holger Fröhlich³

¹ *Dipartimento di Scienze del Farmaco, Università degli Studi di Catania, Viale Andrea Doria, 6, 95125 Catania, Italy*

² *Cancer Vaccine Center, Dana-Farber Cancer Institute, 77 Avenue Louis Pasteur, HIM 401, Boston, MA 02115, USA*

³ *University of Bonn, Bonn-Aachen International Center for IT (B-IT), Algorithmic Bioinformatics, Dahlmannstr. 2, 53113 Bonn, Germany*

Correspondence should be addressed to Francesco Pappalardo, francesco.pappalardo@unict.it

Received 25 November 2012; Accepted 25 November 2012

Copyright © 2012 Francesco Pappalardo et al. This is an open access article distributed under the Creative Commons Attribution License, which permits unrestricted use, distribution, and reproduction in any medium, provided the original work is properly cited.

Revolutions in biotechnology and information technology have produced enormous amounts of biomedical data. Processing and analysis of these data are accelerating the expansion of our knowledge of biological systems. These advances are changing the way biomedical research, development, and applications are done. Clinical data complement the basic biology data, enabling detailed descriptions and modeling of various healthy and diseased states, disease progression, and the responses to therapies. The availability of data representing various biological states, processes, and their time dependencies enables the study of biological systems at various levels of organization, from molecule to whole organism, and even at population levels. Multiple sources of data support a rapidly growing body of biomedical knowledge; however, our ability to analyze and interpret these data lags far behind data generation and storage capacity. Computational models are increasingly used to help interpret biomedical data produced by high-throughput genomics, proteomics, and immunomics projects [1–3]. Advanced applications of computer models that enable the simulation of biological processes are used to generate hypotheses and plan experiments [4–7]. Appropriately interfaced with biomedical databases, computational models enable rapid access to higher-level knowledge and its sharing through data mining and knowledge discovery approaches.

In this special issue, we take an interest in the investigation of the physiology and pathology of the immune responses, particularly the cellular and molecular processes.

The paper contributed by R. Carvalho et al. presents an approach in which a computational model represents the interaction of mycobacterium infection with the innate

immune system in zebrafish. They use the Petri Net formalism to model interaction between key host elements involved in granuloma formation and infection dissemination, defining a qualitative model for the understanding and description of causal relations within this dynamic process. Their systems in biology framework incorporates mathematical modeling to generate and test hypotheses, to perform virtual experiments, and to make experimentally verifiable predictions. This work demonstrates the use of mathematical models that support the study of mechanisms of tuberculosis infection.

The immune system is able to respond more vigorously to the secondary contact with a given antigen than to the priming contact. Vaccination protocols generally include at least two doses, in order to obtain high antibody titers. In particular, studies performed in transgenic mouse models of Alzheimer's disease have demonstrated that antibodies against beta-amyloid are able to reduce plaques and improve cognition. In mouse models as well as in clinical trials in Alzheimer's disease patients, induction of high titers of anti-beta-amyloid antibodies correlates with the therapeutic efficacy of vaccination. F. Castiglione et al. have analyzed relations between the time elapsed from the first dose (priming) and the second dose (boost) on the antibody titers, coupling *in vivo* experiments with computer simulations to assess the effect of delaying the second injection.

A major challenge in immunology is the translation of data into knowledge given the inherent complexity and dynamics of human physiology. The physiology and engineering communities have rich histories in applying computational approaches to translate data obtained from complex

systems into knowledge of system behavior. J. Klinken and Q. Wang review how two related engineering concepts, specifically prototyping and “fitness for use,” can be applied to overcome the pressing challenge in translating data into higher-level knowledge of basic immunology for use in practical applications, such as improvement of therapies. These concepts are illustrated using two immunology-related examples: behavior of beta cell mass at the onset of type 1 diabetes and the dynamics of dendritic cells in the lung.

M. Pennisi presents a mathematical model developed to reproduce the immune response entitled with the combined administration of activated OT1 cytotoxic T lymphocytes (CTLs) and AntiCD137 monoclonal antibodies. This treatment is directed against melanoma in B16 OVA mouse models exposed to a specific immunotherapy strategy. In this paper, two compartments have been modeled: the injection point compartment where the treatment is administered and the skin compartment where melanoma tumor cells proliferate. The outcomes of the mathematical model are in good agreement with the *in vivo* results. In particular the sensitivity analysis highlighted the key role of OT1 CTLs and suggests that a possible reduction of the number of injected antibodies should not affect substantially the treatment efficacy.

Bacterial infections can be acute or chronic. The chronic bacterial infections are characterized by a large bacterial load or by an infection where bacteria grow rapidly. In these cases the immune response is not capable of completely eliminating the infection, leading to the formation of a pattern known as microabscess (or abscess). The microabscess is characterized by an area comprising fluids, bacteria, immune cells (mainly neutrophils), and many types of dead cells. This distinct pattern of formation can only be numerically reproduced and studied by models that capture the spatio-temporal dynamics of the human immune system. B. Pigozzo et al. developed and implemented a computational model to study the process of microabscess formation during bacterial infection.

Cats infected with the feline immunodeficiency virus (FIV) develop an acquired immunodeficiency syndrome (AIDS), similarly to humans infected with HIV. FIV infection causes an acute viremia, which decreases after several weeks, and the appearance of a subpopulation of activated CD8⁺ T cells that we refer to as CD8^{βlow} cells. The expansion of this activated T cell population is recognized as an important marker of FIV infection and disease. Characterization of the CD8^{βlow} population's complex pattern of expansion, including its correlation with other disease markers such as viral load, is likely to increase researchers' understanding of FIV infection and AIDS pathogenesis. B. Ribba et al. propose two simple independent mathematical equations to analyze the time evolution of CD8^{βlow} population size and of viral load during primary infection in cats with FIV. They developed the models using a population approach and mixed-effects regression techniques, based on repeated measurements in more than 100 cats infected with FIV.

Molecular dynamics (MD) simulations have to be sufficiently long to draw reliable conclusions. However, no method exists to prove that a simulation has converged.

In the paper contributed by W. Schreiner et al. a method named “lagged RMSD-analysis” is proposed to determine if an MD-simulation has provided a sufficiently precise model. The analysis is based on RMSD values between pairs of configurations separated by variable time intervals Δt .

In summary, these contributions present state of the art modeling of the immune system. The research papers appearing in this special issue will serve as a guide to current developments and a guide to emerging applications in the fascinating field of immune system modeling.

Ultimately, the utility of computational/mathematical and other quantitative approaches will help provide better healthcare. The seven papers in this volume demonstrate various aspects of modeling of immune processes and preclinical studies of immune responses.

Francesco Pappalardo
Vladimir Brusic
Holger Fröhlich

References

- [1] S. Motta and F. Pappalardo, “Mathematical modeling of biological systems,” *Briefings in Bioinformatics*. In press.
- [2] S. Motta and V. Brusic, “Mathematical modelling of the immune system,” in *Modelling in Molecular Biology*, G. Ciobanu and G. Rozenberg, Eds., Natural Computing Series, pp. 193–218, Springer, New York, NY, USA, 2004.
- [3] N. Petrovsky, D. Silva, and V. Brusic, “The future for computational modelling and prediction systems in clinical immunology,” *Novartis Foundation Symposium*, vol. 254, pp. 23–42, 2003.
- [4] F. Pappalardo, M. D. Halling-Brown, N. Rapin et al., “Immuno-Grid, an integrative environment for large-scale simulation of the immune system for vaccine discovery, design and optimization,” *Briefings in Bioinformatics*, vol. 10, no. 3, pp. 330–340, 2009.
- [5] A. Palladini, G. Nicoletti, F. Pappalardo et al., “In silico modeling and *in vivo* efficacy of cancer-preventive vaccinations,” *Cancer Research*, vol. 70, no. 20, pp. 7755–7763, 2010.
- [6] V. Brusic and N. Petrovsky, “Immunoinformatics and its relevance to understanding human immune disease,” *Expert Review of Clinical Immunology*, vol. 1, no. 1, pp. 145–157, 2005.
- [7] F. Pappalardo, I. M. Forero, M. Pennisi, A. Palazon, I. Melero, and S. Motta, “SimB16: modeling induced immune system response against B16-melanoma,” *PLoS ONE*, vol. 6, no. 10, Article ID 002652, 2011.

Research Article

Modeling Innate Immune Response to Early *Mycobacterium* Infection

Rafael V. Carvalho,¹ Jetty Kleijn,¹ Annemarie H. Meijer,² and Fons J. Verbeek¹

¹Leiden Institute of Advanced Computer Science, Leiden University, Niels Bohrweg 1, 2333 CA Leiden, The Netherlands

²Institute of Biology, Leiden University, Einsteinweg 55, 2333 CC Leiden, The Netherlands

Correspondence should be addressed to Fons J. Verbeek, fverbeek@liacs.nl

Received 15 June 2012; Revised 24 September 2012; Accepted 8 October 2012

Academic Editor: Francesco Pappalardo

Copyright © 2012 Rafael V. Carvalho et al. This is an open access article distributed under the Creative Commons Attribution License, which permits unrestricted use, distribution, and reproduction in any medium, provided the original work is properly cited.

In the study of complex patterns in biology, mathematical and computational models are emerging as important tools. In addition to experimental approaches, these modeling tools have recently been applied to address open questions regarding host-pathogen interaction dynamics, including the immune response to mycobacterial infection and tuberculous granuloma formation. We present an approach in which a computational model represents the interaction of the *Mycobacterium* infection with the innate immune system in zebrafish at a high level of abstraction. We use the Petri Net formalism to model the interaction between the key host elements involved in granuloma formation and infection dissemination. We define a qualitative model for the understanding and description of causal relations in this dynamic process. Complex processes involving cell-cell or cell-bacteria communication can be modeled at smaller scales and incorporated hierarchically into this main model; these are to be included in later elaborations. With the infection mechanism being defined on a higher level, lower-level processes influencing the host-pathogen interaction can be identified, modeled, and tested both quantitatively and qualitatively. This systems biology framework incorporates modeling to generate and test hypotheses, to perform virtual experiments, and to make experimentally verifiable predictions. Thereby it supports the unraveling of the mechanisms of tuberculosis infection.

1. Introduction

Tuberculosis (TB) is an infectious disease responsible for 1.5 million deaths annually. About one-third of the world's population is infected with the pathogen that causes this disease, *Mycobacterium tuberculosis* (*Mtb*). Most infections are controlled by the host's immune system and remain asymptomatic. However, the *Mtb* is capable to persist in the host inside granulomas, highly organized structures characterized by the presence of differentiated macrophages, lymphocytes, and other immune cells that contain, but fail to eradicate, the pathogen [1, 2]. The key to success of *Mtb* infection lies, at least in part, with the ability of the bacteria to proliferate inside host macrophages despite the antimicrobial properties of these cells. Some of the infecting bacteria can survive for extended periods within macrophages and in a granuloma, establishing long-term infections that may resurface later, for example, when the

host's immune system is compromised due to malnutrition, HIV coinfection, or immunosuppressive treatment. Insight in the mechanisms that contribute to this long and complex relationship between the pathogen and the host is essential to the understanding of the fundamental aspects of TB [3].

Various animal models are used to mimic *Mtb* pathogenesis in humans, each having their specific strengths as well as limitations. In the recent years, the zebrafish has emerged as a valuable addition to the mammalian models. They are genetically tractable and have an immune system with innate and adaptive branches, very similar to the human immune system. A particularly useful property is the transparency of the embryos, which allows for real-time imaging of the interaction between pathogens and host immune cells [4–7]. *Mycobacterium marinum* (*Mm*), one of the closest relatives of *Mtb*, is used to study mycobacterial pathogenesis in zebrafish. It causes a systemic tuberculosis-like infection

in zebrafish, with the formation of structured granulomas that closely resemble those in human TB. The use of this model has recently contributed important insights into the function of the granuloma in expansion and dissemination of mycobacteria during the early stages of infection [8].

Mathematical and computational modeling provides an important additional avenue for the further exploration of disease dynamics and offers powerful and complementary tools for the study of the host-pathogen interaction. Gathering and analyzing the information from the animal model in a computational modeling process makes it possible to describe, simulate, analyze and predict the mechanism and interactions behind the infection process in intuitive and easily analyzable terms. The agent-based model (ABM) is a computational formalism based on rules that govern autonomous agents [9]; it can be used to model discrete as well as stochastic events in biology. Pappalardo et al. have implemented and simulated models using ABM and cellular automata to study the vaccine administration and immune response to cancer in mice [10–12]. Kirschner et al. have utilized ABM to model and simulate the *Mtb* disease and the host-pathogen interaction [13–15]. They suggest the ABM as an appropriate method for exploring complex spatiotemporal systems such as granuloma formation [16]. The Petri net (PN) formalism is another method providing a natural and promising modeling technique useful for modeling metabolic pathways and biological behavior [17]. The PN formalism is, typically, very suitable for systems with a concurrent nature, that is, systems in which processes occur in parallel. In essence, the PN is a mathematical modeling language based on a directed bipartite graph. The PN formalism has already been successfully applied on case studies in biology to create, verify, and validate models. The stochastic activity network (SAN) is an extended Petri net model that uses probabilistic time and is in particular useful for performance evaluation. Tsavachidou and Liebman [18] have used SAN in modeling and quantitative evaluation of the biological pathways involved in menopause. They use biological pathways and experimental data in an accurate quantitative model to simulate and compare to *in vivo/in vitro* experiments. Peleg et al. [19] have used colored hierarchical PNs to study the effects of mutations in tRNA on the protein translation. They define qualitative models of molecular function at different levels of granularity. The application domain of tRNA was chosen due the abundant literature on tRNA molecular structure as well as the diseases that relate to abnormal structure. Regarding the process of mycobacterial infection, the interaction with host-pathogen is complex and much remains unknown and significance of specific immune factors present on the mycobacterial infection process still poorly understood. To date, mathematical and computational models applied to mycobacterial infection have been used to explore specific aspects at various biological scales (e.g., intracellular, cell-cell interactions, and cell population dynamics) [14–16]. The mycobacterial infection process thus is composed of numerous subprocesses, some of which are mutually dependant, giving rise to a very complex set of interactions. A model describing the process at a higher level is missing, and therefore we take the construction of

a model of the infection mechanism at a higher level of granularity as a starting point for our modeling efforts and explorations. The availability of such a model enables to connect and visualize the whole infection process. This top-down approach allows identifying, modeling, and testing of the lower-level processes in both qualitative and quantitative manner. The input for these lower-level processes is obtained from both empirical research and literature data.

The *zebrafish* model of *Mycobacterium* infection, based on *Mm* infection, has been identified as very useful in the understanding of host-mycobacteria interactions during early stages of infection. This model system is used to generate experimental data that elucidate the pathogenesis as well as to transfer the findings to the human case. The perspective of analysis from *in vivo/in vitro* studies requires an integration layer so that experimental data can be understood in the range of complex interactions that are underlying the infection process. Therefore, we intend to construct such integration layer from an *in silico* perspective using the Petri net formalism as a modeling method to simulate bacteria-host interactions in early stages of tuberculous granuloma formation. As indicated, our starting point is to construct such a model from a higher level of abstraction. We, therefore, designed a PN by first identifying the processes in the infection process, that is, phagocytosis of mycobacteria by macrophages, the migration of infected macrophages to deeper tissue, the growth of mycobacteria within individual macrophages, and the granuloma formation and maturation. These processes were represented in a qualitative colored Petri net (CPN) using the Snoopy software, a tool for modeling and animating/simulating hierarchical graph-based formalisms. The information analysis on the processes was obtained from recent literature about the phases involved in the early response to mycobacterial infection [8] and from interviews with researchers.

From the processes as the major design elements, we constructed a qualitative colored Petri net on a level of abstraction that helps understanding and describing the causal relations in a dynamic process. In addition to the processes, we acknowledged entities such as the zebrafish, the macrophage, the granuloma, and the bacteria. As such, the phases of the infection process are addressed whilst, for the moment, time and probability are not considered. In this manner, our model explores the disease on a high level of abstraction, modeling the factors that are crucial to visualize the mycobacterial infection process and the early immune response. Complex processes involving cell-cell or cell-bacteria communication can be modeled in a small-scale process and incorporated into the model as a hierarchical layer. As intended, the model shows the cause-effect relations that trigger the infection process. The graphical representation of the CPN communicates that in a manner a biologist can grasp immediately. Now, as the model incorporates the process of infection, the toolbox of the biologist is extended with an approach that allows to perform “what-if” as part of the experimentation whereas at the same time new experimental findings can be added to the model in a close collaboration between empirical and modeling scientists.



FIGURE 1: Microscope image of a zebrafish larva infected with *Mycobacterium marinum* by injection used for the study on infection progression and immune system response. Image is obtained with a Leica stereo fluorescence microscope commonly used in zebrafish research. Here the microscope image is depicted with an overlay of a fluorescent channel (red) in which the bacteria are visualized. The arrows indicate granulomas that have been developed after an induced infection with *Mycobacterium marinum*.

Starting from the abstract model of the global infection process, future extensions, such as submodels representing processes on tissue, cellular, and molecular scale, will hierarchically connect as a single model. In close collaboration with the empirical scientist and using the model, we intend to perform *in silico* experiments that are otherwise impractical or not feasible *in vivo* or *in vitro*, thereby predicting results of new experiments and generate further hypotheses about the immune system response to mycobacterial infection. The CPN model presented in this paper is the cornerstone of that process.

The remainder of this paper is structured as follows. In Section 2, we discuss the pathogenesis of the *Mycobacterium* infection in Zebrafish in more detail and next we introduce the building blocks of the CPN and the software that we have used to build the model. In Section 3, we provide a series of design considerations to come to an implementation of the model. Finally in Section 4, we end with the conclusion and discussion.

2. Materials and Methods

2.1. The Zebrafish Model of Mycobacterial Pathogenesis. The zebrafish is naturally susceptible to infections caused by *M. marinum* (*Mm*), genetically closely related to *M. tuberculosis* (*Mtb*). The *Mm* infection shares pathological hallmarks with *Mtb* infection. Like other pathogenic mycobacteria, *Mm* causes chronic infection of macrophages resulting in tuberculous granulomas, making it a useful model to study mycobacterial pathogenesis [20]. Zebrafish embryos have functional innate immune cells (macrophages and neutrophils), while their adaptive immune system is not yet functional. The experimental infection of zebrafish embryos is initiated by injected bacteria into the blood circulation or into tissue. Macrophages that are attracted to the site of infection take up the mycobacteria by a process called phagocytosis. Real-time imaging of infected zebrafish embryos has allowed the direct observation of the arrival of phagocytes at the infection site and their uptake of bacteria. The macrophages are the primary cell type infected with *Mm*; however, also infected neutrophils have been observed [6, 8] and were recently shown to play an important role in *Mm* infection control [21]. In Figure 1, an *Mm* infection in a zebrafish is depicted.

Inside the macrophage, bacteria can be exposed to bactericidal mechanisms and degraded in lysosomes. However, intracellular mycobacteria are predominantly distributed between the early and late phagosomal compartments, with some also escaping into the cytoplasm [22, 23]. Similar to *Mtb*, *Mm* escapes from lysosomal degradation and its survival inside macrophages is facilitated through the dynamic modulation of a range of cellular processes. These include inhibition of pathways involved in the fusion of the phagosome with lysosomes, antigen presentation, apoptosis, and the activation of bactericidal responses [23–25]. Mycobacterial interference with the host signaling machinery severely compromises the immune defences, and the multiplication of mycobacteria inside the macrophage over time causes its death, thereby enabling further spreading of the infection.

Once it has become infected with mycobacteria, the macrophage starts to induce recruitment of uninfected macrophages. Studies have established an important role for a mycobacterial virulence factor, the ESX-1 secretion system, in the recruitment of new macrophages to granulomas and the expansion of infected macrophages [5, 25, 26]. These macrophages efficiently find and phagocytose infected macrophages and bacteria that are released from dead cells, but in this process these macrophages are getting infected too. The aggregated macrophages become activated, a transformation reflected by an increase in their size and subcellular organelles, ruffled cell membranes, and enhanced phagocytic and microbicidal capabilities. A common feature of all *Mycobacterium* granulomas is the further differentiation of the macrophages into epithelioid cells that have tightly interdigitated cell membranes in zipper-like arrays linking adjacent cells. Those aggregates grow into organized structures that are referred to as granulomas, lumps of immune cells that surround the infection [23].

Primary granulomas are capable of disseminating infection throughout the body by egression of infected macrophages which suggests that granuloma macrophages constitute the major mechanism for dissemination of the infection [5]. These granulomas are the hallmark of the tuberculosis disease in both human and animal models. In Figure 2, a schematic representation is depicted of the early stages of the mycobacterial of the pathogenesis infection process.

2.2. Computational Modeling. Experimental research has generated a tremendous amount of insights into host-pathogen interactions that occur during mycobacterial infections. Mathematical and computational models can offer powerful and complementary methods in support for better understanding the mechanisms behind the infection process in intuitive and easily analyzable terms. Amongst these methods, we can refer to modeling approaches such as Brane calculi [28], π -calculus [29], agent-based modeling (ABM) [16], and petri nets (PNs) [30]. These modeling methods can be used to describe, simulate, analyze, and predict the behavior of biological system by turning what is known about the biology into equations and/or rules to describe and ultimately understand the system. Previously,

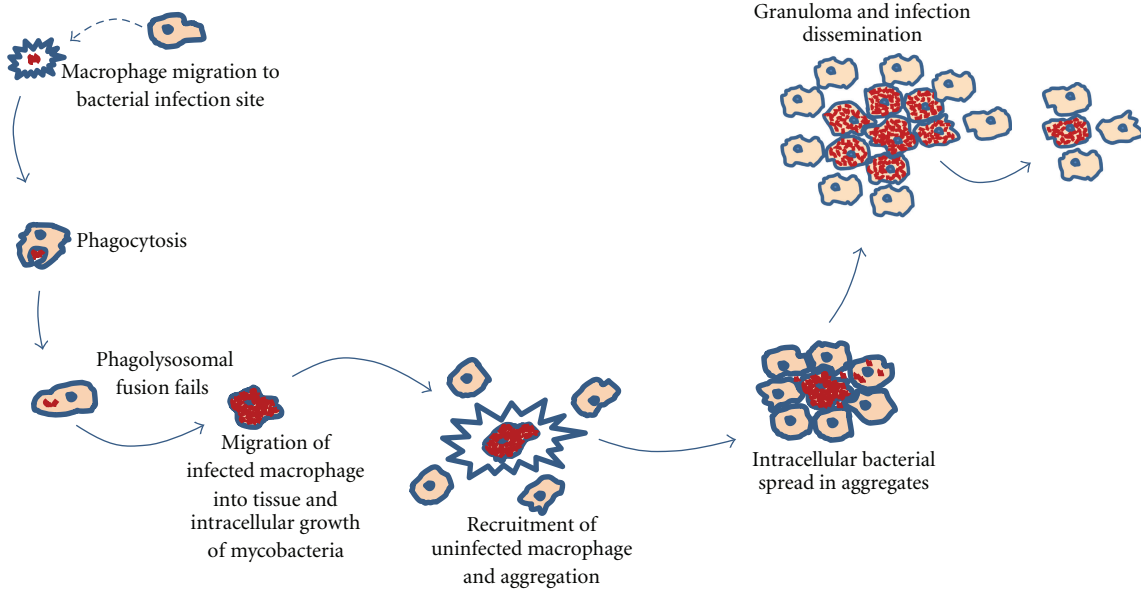


FIGURE 2: Schematic representation of the early stages of the immune response to the early stages of the mycobacterial infection process. This figure is an authors' rendition adapted from [27].

we proposed a system for modeling, simulating, and visualizing the *Mycobacterium* infection and granuloma formation, addressing the basic layout and the modeling challenges for this approach and evaluating between computational methods the Petri net as an appropriate method for the modeling of the infection process [31].

The Petri nets provide a formal and clear representation of systems based on their firm mathematical foundation for the analysis of system properties. The graphical notation of Petri nets allows an easy and intuitive construction of models of biological systems. To characterize the structure, behavioral properties, and dynamics of a model, there are several techniques to add time-dependent and space aspects as well as data and probabilistic aspects [32]. Petri nets have as their underlying structure a directed, finite, bipartite graph, typically without isolated nodes. The four main components of a general Petri net are as follows [33]:

- (i) *places*: passive nodes that refer to conditions or local states;
- (ii) *tokens*: variable elements that represent current information on a condition or local state;
- (iii) *transitions*: active nodes that describe local state shifts, events, and activities in the system;
- (iv) *directed arcs*: connections that specify relationships between transitions and places.

Standard PN models are discrete and have no notion of time and as such are very useful for modeling processes without time or probability. To model more complex processes, extensions to the standard PN are used; in colored Petri nets (CPNs), data values are assigned features using different colors as data structure [34]; in stochastic Petri nets (SPNs) probabilities are added to the transitions [35];

other extensions such as hybrid Petri nets (HPNs) and hybrid functional Petri nets (HFPNs) allow for coexistence of both continuous and discrete processes [36].

In order to create a flexible, compact, and parameterizable model, we decided to use a CPN to model the early stages of the infection process and granuloma formation. Although standard Petri nets can be used to model parts of our problem, such as reaction processes and biochemical components, it becomes impractical to represent different levels of abstraction, when in addition, other aspects have to be taken into account such as the physical and spatial organization of the organism, from the intracellular to the intercellular level and beyond (molecular, cellular, and tissues). Colored Petri nets allow the description of several similar network structures in a concise and well-defined way, providing a flexible template mechanism for network designers. In colored Petri nets, tokens can be distinguished by their colors. This allows one to discriminate levels (molecules, metabolites, proteins, secondary substances, genes, etc.). In addition, the token colors can be used to distinguish between subpopulations of a species in different locations (cytosol, nucleus, and so on).

For these reasons, we have chosen to model the early stages of the *Mycobacterium* infection process and granuloma formation and dissemination in terms of colored Petri nets. The process consists of phagocytosis of the mycobacteria by macrophages, migration of infected macrophages, and bacterial replication in an individual macrophage as well as the aggregation, granuloma formation, and dissemination of the infection. In the following section, we give a definition of CPN based on [34, 37]. We use B to denote the Boolean type, containing the elements $\{\text{false}, \text{true}\}$ with the standard operations from propositional and we use $\text{Type}(\text{Vars})$ to denote a set of types $\{\text{Type}(v) \mid v \in \text{Vars}\}$ of a typed set Vars.

Definition 1. A *multiset* m over a nonempty set S is a function $m : S \rightarrow \mathbb{N}$. An element $s \in S$ is said to belong to the multiset m if $m(s) \neq 0$, and then we write $s \in m$. The nonnegative integers $\{m(s) \mid s \in S\}$ are called the coefficients of the multiset m , and $m(s)$ is called the coefficient of s . The nonnegative integer $m(s) \in \mathbb{N}$ is the number of appearances of the element s in the multiset m .

We may represent a multiset m by the formal sum:

$$\sum_{s \in S} m(s)'s. \quad (1)$$

By S_{MS} we denote the set of all multisets over S .

Definition 2. A colored Petri net is a tuple $CPN = (\Sigma, P, T, A, C, G, E, I)$, where

- (i) Σ is a finite nonempty set of types, called color sets;
- (ii) P is a finite nonempty set of places;
- (iii) T is a finite nonempty set of transitions such that

$$P \cap T = \emptyset; \quad (2)$$

- (iv) A is a finite set of arcs such that

$$A \subseteq P \times T \cup T \times P; \quad (3)$$

- (v) C is a color function; it is defined from P to Σ ;
- (vi) G is a guard function; it is defined from T to expressions such that

$$\forall t \in T : [\text{Type}(G(t)) = B \wedge \text{Type}(\text{Var}(G(t))) \subseteq \Sigma]; \quad (4)$$

- (vii) E is an arc expression function; it is defined from A into expressions such that

$$\begin{aligned} \forall a \in A : [\text{Type}(E(a)) = C(p(a))_{MS} \\ \wedge \text{Type}(\text{Var}(E(a))) \subseteq \Sigma], \end{aligned} \quad (5)$$

where $p(a)$ is the place component of a ;

- (viii) I is an initialization function (initial marking); it is defined from P into closed expressions such that

$$\forall p \in P : [\text{Type}(I(p)) = C(p)_{MS}]. \quad (6)$$

In general, a marking m is a function associating with each place p a multiset $m(p)$ of colors (tokens) from $C(p)$. Markings are the global states of the colored Petri net.

The Petri net semantics describes the behavior of the net, based on a firing rule consisting of a precondition and the effect of the occurrence (firing) of a single transition. Whether or not a transition can fire depends on the marking of its preceding-places and the arc expression on the input arcs. A transition is enabled and is allowed to fire, if all preceding-places, are sufficiently marked and if the binding of the variables that appear in the arc expressions evaluates

to a multiset of token colors that is present on the corresponding input place. The guards of the transition should evaluate to true for the giving binding. If a transition has no preceding-places, it is always enabled. When a transition occurs with a given binding, a multiset of colored tokens are taken from each preceding-place and added to later-places in accordance with the arc expression on the arc leading to those places. Repeatedly firing transitions lead to firing sequences and determine the state space of the Petri net [33].

2.3. Software and Hardware Platform. Several tools are available to model biological systems using Petri nets, simulate their dynamic behavior, and analyze their structure. The Snoopy software provides an extensible, adaptive, and multiplatform framework to design, animate, and simulate Petri nets [38]. Its design facilitates the modular implementation of our CPN model allowing future extensions to be added through hierarchical organization of Petri nets. We have used the Snoopy software to implement and animate our net with two different operating systems (OS): Windows 7 (HP Intel core i7, 4 Gb RAM) and Mac OS 10.6 (MacBook Pro Intel core i7, 4 Gb RAM). The main difference between the two platforms is the additional features in the user interface for the Windows implementation. The CPN model runs with the same accuracy on both OS versions. This illustrates the platform independency of the Snoopy software framework.

3. Results

We have modeled the role of the innate immune system in the early stages of a *mycobacterial* infection. Our approach is to provide a large-scale model that drives the infection behavior. We have used the Snoopy tool, a framework for modeling and animating/simulating hierarchical graph-based formalisms [38], in order to create a qualitative colored Petri net representing the relevant phases in the infection process as depicted on Figure 2. In the following sections, we present the color sets Σ , places P , transitions T , and the initial marking I present in our $CPN = (\Sigma, P, T, A, C, G, E, I)$.

3.1. Set of Color Sets Σ . We have defined five simple color sets: position, individual, status, and count and four compound color sets: macrophage, bacteria, proliferation, Granuloma composed of the basic color sets. They represent empirical information from the infection process:

- (i) position is an integer value representing the location of a macrophage, bacteria, and/or granuloma;
- (ii) individual is a string value (mm, mac) used to identify bacteria and macrophages;
- (iii) status is a Boolean value; it can represent the infection status (healthy/infected) of a macrophage or the saturation of a proliferation;
- (iv) count is an integer value representing a threshold for the simulation;
- (v) macrophage is composed of position, individual, and status colors and represents host macrophage immune cells;

- (vi) bacteria is composed of position and individual colors and represents *M. marinum* bacteria that will be injected;
- (vii) proliferation is composed of count, individual, and status colors and represents the amount of infected aggregated macrophages;
- (viii) granuloma is composed of position, individual, and count colors and represents granulomas with the amount of macrophages.

3.2. *Set of Places P.* The set of places of our CPN is defined as

$$P = \{\text{Infection, ImmuneSystem, Phagocytosis, Migration, BactGrowth, Checkpoint, Condition, DeadMacrophage, RecruitmentCount, AgregationAmount, StopSignaling, Maturation, Dissemination}\}. \quad (7)$$

They represent population of cells and multicellular complexes that are part of our model:

- (i) $C(\text{Infection}) = \{\text{Bacteria}\}$: a place with the mycobacteria that intrude the host;
- (ii) $C(\text{ImmuneSystem}) = \{\text{Macrophage}\}$: a place containing the immune cells (healthy macrophages) that will react to an infection signaling;
- (iii) $C(\text{Phagocytosis}) = \{\text{Macrophage}\}$: a place containing the infected macrophages;
- (iv) $C(\text{Migration}) = \{\text{Macrophage}\}$ and $C(\text{BactGrowth}) = \{\text{Proliferation}\}$: places containing information about the bacterial replication within one macrophage and its movement;
- (v) $C(\text{DeadMacrophage}) = \{\text{Macrophage}\}$ and $C(\text{AgregationAmount}) = \{\text{Granuloma}\}$: places containing dead macrophages and the aggregation of recruited healthy macrophages (granuloma);
- (vi) $C(\text{Maturation}) = \{\text{Macrophage}\}$ and $C(\text{Dissemination}) = \{\text{count}\}$: places containing information about the infected aggregated macrophages (intracellular bacterial spread) and the control of the infection dissemination;
- (vii) $C(\text{Checkpoint}) = \{\text{status}\}$, $C(\text{Condition}) = \{\text{status}\}$, $C(\text{RecruitmentCount}) = \{\text{count}\}$ and $C(\text{StopSignaling}) = \{\text{count}\}$: places controlling the flow of the simulation.

3.3. *Set of Transitions T.* The set of transitions of our model is defined as

$$T = \{\text{BacSignaling, MacSignaling, IntracelullarSpread, Spread, } t1, t2, t3, t4\}. \quad (8)$$

They describe important events that govern the infection process and refer to the molecular interaction, signaling

reaction and intracellular changes; they also regulate some thresholds that control the simulation:

- (i) BacSignaling represents the signaling process when bacteria reach the host;
- (ii) MacSignaling represents the signaling process of an infected macrophage after its death (recruitment of healthy macrophages);
- (iii) IntracelullarSpread represents the bacterial replication among the aggregated macrophage in the granuloma;
- (iv) Spread represents the dissemination of granuloma infection;
- (v) $t1, t2, t3$, and $t4$ represent the control thresholds of the simulation.

3.4. *Initial Marking I.* The initial marking in our model determines for each place the number and type of colored tokens initially present in the places. We have the condition markings that are fixed and used to control the process and the example markings which are used in our example and can be modified without changing the workflow. They are defined as follows.

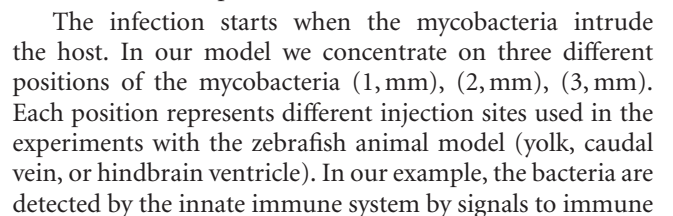
Condition markings:

- (i) $I(\text{Checkpoint}) = 1'(\text{true})$: initialized for checking if the bacterial replication inside the macrophage reaches its limits;
- (ii) $I(\text{RecruitmentCount}) = 1'(0)$: initialized for counting the number of macrophages recruited to aggregate into the dead macrophage;
- (iii) $I(\text{BactGrowth}) = 1'(1, \text{mm}, \text{true})$: initialized to trigger replicating the bacteria inside the macrophage;
- (iv) $I(\text{Dissemination}) = 1'(0)$: initialized to keep count of the dissemination of the granuloma;
- (v) $I(\text{Condition}) = 1'(\text{true})$: initialized to enable one infected macrophage become dead and start the signaling process.

Example markings:

- (i) $I(\text{Infection}) = 1'(1, \text{mm}) + 1'(2, \text{mm}) + 1'(3, \text{mm})$ defines the initial concentration of the mycobacteria that will intrude the host. We have defined three different positions to represent different injection sites;
- (ii) $I(\text{ImmuneSystem}) = 1'(1, \text{mac}, \text{false}) + 1'(2, \text{mac}, \text{false}) + 1'(3, \text{mac}, \text{false}) + \dots + 1'(10, \text{mac}, \text{false})$ defines the initial concentration of healthy macrophages in the host. The positions and amount of healthy macrophages are empirical and used just to represent their presence in the host.

All other places are initially empty, that is, there are no tokens at the onset.



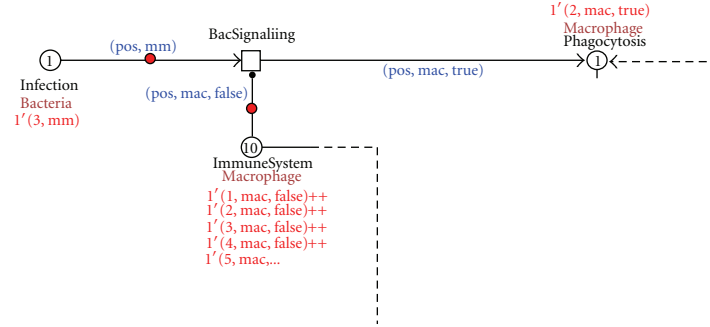


FIGURE 4: Screenshot of the infection detection and phagocytosis process.

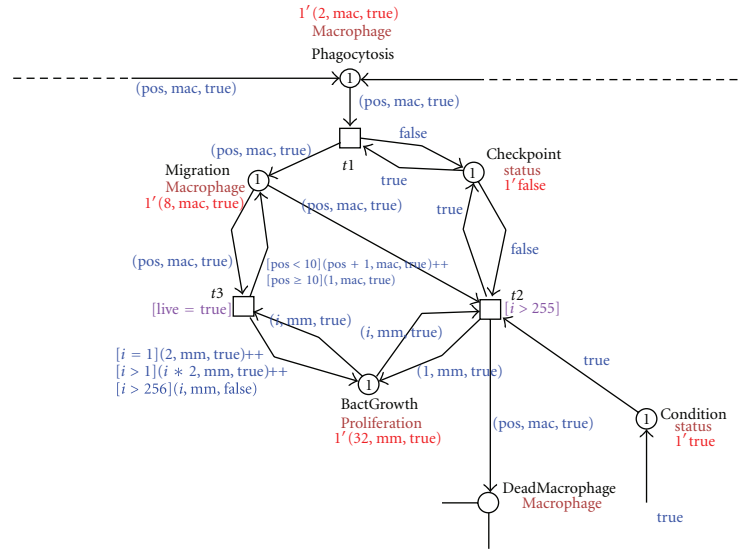


FIGURE 5: Screenshot of the migration and bacterial replication within macrophage causing its death.

cells, in our model healthy macrophage (1, mac, false), (2, mac, false), (3, mac, false) ... (10, mac, false), to take up the bacteria (phagocytosis). Figure 4 shows this process.

After phagocytosis, the bacteria start to proliferate and move within the macrophage; the macrophage changes its position, moving to deep tissue while the bacteria replicate inside the macrophage. The intracellular growth of mycobacteria is modeled as bacterial multiplication until a concentration of 255, causing the death of the macrophage. Figure 5 depicts this process.

A dead macrophage starts to signal, recruiting new healthy macrophages to take up the infected macrophage and the bacteria. In this way aggregates of immune cells are formed. The aggregates contain the bacteria but are unable to get rid of them. This process is visualized in Figure 6 where a dead macrophage $1'(10, \text{mac}, \text{true})$ is recruiting new macrophages to aggregate. The recruitment of macrophages is controlled by the MacSignaling transition that stops when four healthy macrophages are recruited. The numbers of macrophages that are recruited are set such that a minimal number will give rise to the formation of a granuloma. The latter is important in the development of the infection and

the disease in general. The number can be increased if a particular scenario for an *in silico* experiment so requires. It will not alter the general layout of the net rather creating different balances. The place RecruitmentCount controls that.

As these aggregates grow, structures develop that are referred to as tuberculous granulomas, lumps of immune cells that surround the infection. Figure 7 shows the representation of this process in our model, where one granuloma is formed at the position 10 with a concentration of five macrophages $1'(10, \text{mac}, 5)$.

The intracellular mycobacterial spread in the granuloma is visualized in our model by the process depicted in Figure 8. There, all five immune cells that form the granuloma on the position 10 $\{5'(10, \text{mac}, \text{true})\}$ get infected and start the process of dissemination.

In the dissemination process, an infected macrophage leaves the granuloma structure $\{3'(10, \text{mac}, \text{true})\}$ and starts another infection, moving, hosting an intracellular mycobacterial replication, dying, and repeating the granuloma formation process on another position. This process is visualized in Figure 9.

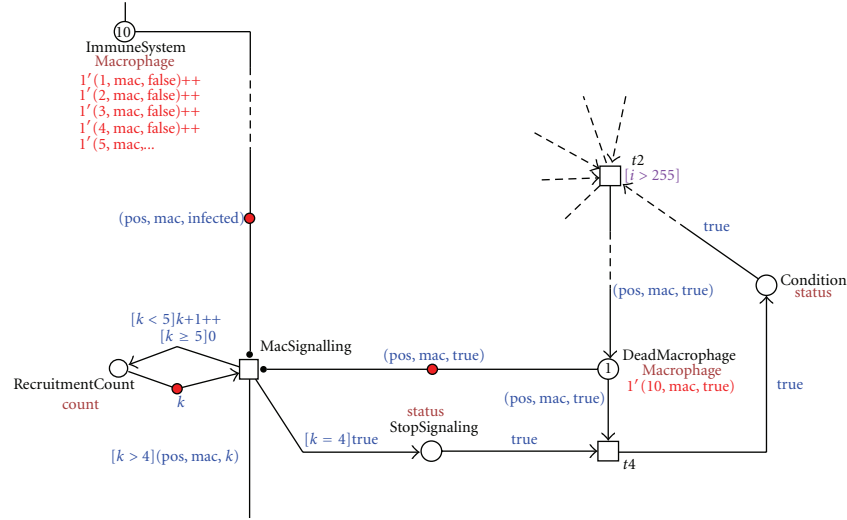


FIGURE 6: Screenshot of the dead macrophage signaling and aggregation process.

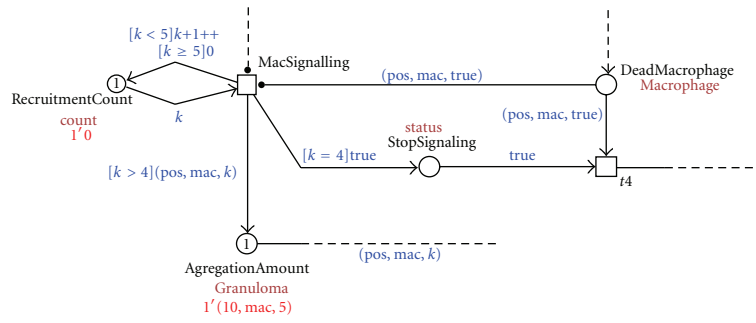


FIGURE 7: Screenshot of the granuloma formation process.

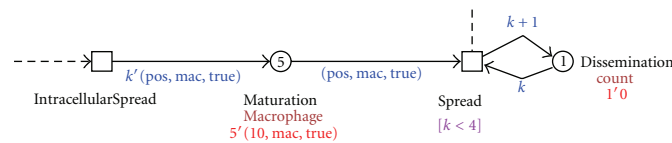


FIGURE 8: Screenshot of the intracellular mycobacterial spread and the infection dissemination process.

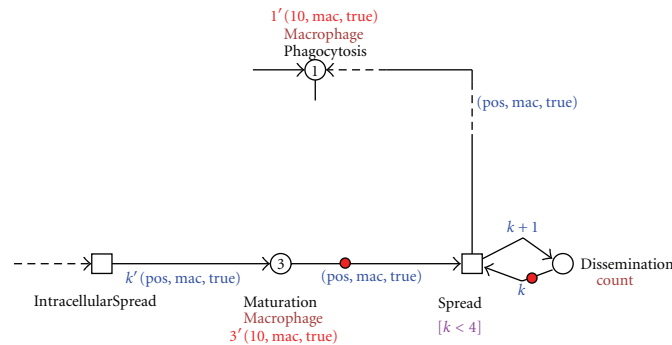


FIGURE 9: Screenshot of the granuloma formation process on the dissident infected macrophages on different positions.

The outcome of our model reproduces the early stages of the mycobacterial process and the innate immune response. We used the animation mode available in the Snoopy software to verify the dynamic behavior of our model. This property allows to animate the token flow of the net as well as to observe the causality of the model and its behavior. For inspection and perusal, the animation sequence can be found at <http://bio-imaging.liacs.nl/galleries/cpn-mmarminum>.

4. Conclusion and Discussion

A systems' biology approach, integrating both modeling and experimental aspects, has much to contribute to the study of host-pathogen interactions. Biological processes that are relevant to the immune response occur at different scales or levels of resolution, that is, molecular, cellular, and tissue levels [39, 40]. Development of multiscale, multi-compartment models based on *in vivo/in vitro* experimental data is essential to create a computational system that reflects this biological behavior [40]. In our previous work [31], we provide a basic layout addressing the modeling challenges from the integration of imaging analysis data and the Petri net formalism in different levels of abstraction, from epidemiological to genetic levels in a multiple-scale model.

The aim of this work is to introduce a modeling approach new to the modeling of the innate immune response in a model; this modeling represents the dynamic behavior of the mycobacterial infection process. We consider our model to represent a high level of abstraction in which the infection process can be visualized in a large-scale model. Complex processes involving cell-cell or cell-bacteria communication can be modeled as small-scale processes and incorporated in our model. We use the Petri net formalism as a formal modeling method because of its extensible, modular, easy, and intuitive construction properties different from other and more broadly used modeling frameworks [32]. We have developed a high-level abstraction of the infection process by designing a PN by acknowledging the major processes of the *Mycobacterium* infection together with the basic actors that are involved in these processes.

As a result, we have delivered a CPN model that expresses, at a high level of abstraction, the details that are involved in the early disease of mycobacterial infection. Information about the early mycobacterial infection process, the innate immune response, and the infection dissemination can be observed in our model. Through a parameterizable net that assembles information about the host-pathogenesis interaction phases, we can visualize the dynamics of the infection process. The scalability of our model allows extension on different levels of abstraction providing the aggregation of independent and related model hierarchically, that is, gene expression pathways, molecular process, cell-to-cell interaction events, and so forth. In this manner allowing experiments that simultaneously track molecular, cellular, tissue, organism, and population scale events, biologists have greatly appreciated the visualization of the processes through the animation of the PN.

Several reliable tools have been developed to create and investigate qualitative and quantitative properties of Petri nets by structural analysis, simulation of time-dependent dynamic behavior, and model checking. In the research presented here, we have chosen the Snoopy software [38] to implement and animate our model. This software is extensible and adaptive through support of simultaneous use of several models. Moreover, it is platform independent. Further extensions are to investigate the quantitative properties of the process. Such can be accomplished using the Charlie tool [41] so as to verify and validate the net and further analyze our model.

In summary, we have developed a straightforward model to explore the early mycobacterial infection and the immune response. Modeling the steps that regulate the infection process requires further testing on both theoretical and experimental levels. The results of these *in silico* experiments/findings can become the input for further analysis. It will support, for example, identification of key parameters or mechanisms, interpretation of data, or comparison of the capability of different mechanisms to (re)generate the observed data. Finally, a model that successfully describes existing experimental data may be used in the prediction of results from new experiments and generation of further hypotheses about the immune system response to mycobacterial infection helping to unravel the mechanisms of TB infection [42]. In this manner it can contribute to treatment. As indicated from the design of our CPN, the next steps in the development of the net are to add lower-level processes representing the tissue, cellular, and molecular interactions relevant to the infection process. The CPN accommodates this as hierarchical layers. Along with these layers, numerical data will become available that will allow to elaborate on the quantitative aspects of this process. The interplay of hierarchical levels and quantitative information has the potential to develop to a powerful tool for the research in tuberculosis disease, and hopefully it will further mature in a paradigm for integrated research to infection diseases.

References

- [1] J. L. Flynn and J. Chan, "Immunology of tuberculosis," *Annual Review of Immunology*, vol. 19, pp. 93–129, 2001.
- [2] A. H. Meijer and H. P. Spaink, "Host-Pathogen interactions made transparent with the zebrafish model," *Current Drug Targets*, vol. 12, no. 7, pp. 1000–1017, 2011.
- [3] C. L. Cosma, D. R. Sherman, and L. Ramakrishnan, "The secret lives of the pathogenic mycobacteria," *Annual Review of Microbiology*, vol. 57, pp. 641–676, 2003.
- [4] N. D. Meeker and N. S. Trede, "Immunology and zebrafish: spawning new models of human disease," *Developmental and Comparative Immunology*, vol. 32, no. 7, pp. 745–757, 2008.
- [5] J. M. Davis and L. Ramakrishnan, "The role of the granuloma in expansion and dissemination of early tuberculous infection," *Cell*, vol. 136, no. 1, pp. 37–49, 2009.
- [6] J. M. Davis, H. Clay, J. L. Lewis, N. Ghori, P. Herbomel, and L. Ramakrishnan, "Real-time visualization of Mycobacterium-macrophage interactions leading to initiation of granuloma formation in zebrafish embryos," *Immunity*, vol. 17, no. 6, pp. 693–702, 2002.

- [7] D. Traver, P. Herbomel, E. E. Patton et al., "The Zebrafish as a model organism to study development of the immune system," *Advances in Immunology*, vol. 81, pp. 253–330, 2003.
- [8] A. H. Meijer, A. M. van der Sar, C. Cunha et al., "Identification and real-time imaging of a myc-expressing neutrophil population involved in inflammation and mycobacterial granuloma formation in zebrafish," *Developmental and Comparative Immunology*, vol. 32, no. 1, pp. 36–49, 2008.
- [9] D. J. Barnes and D. Chu, *Introduction to Modeling for Biosciences*, Springer, London, UK, 2010.
- [10] F. Pappalardo, M. D. Halling-Brown, N. Rapin et al., "ImmunoGrid, an integrative environment for large-scale simulation of the immune system for vaccine discovery, design and optimization," *Briefings in Bioinformatics*, vol. 10, no. 3, pp. 330–340, 2009.
- [11] F. Pappalardo, I. M. Forero, M. Pennisi, A. Palazon, I. Melero, and S. Motta, "SimB16: modeling induced immune system response against B16-melanoma," *PLoS ONE*, vol. 6, no. 10, Article ID e26523, 2011.
- [12] D. Alemani, F. Pappalardo, M. Pennisi, S. Motta, and V. Brusici, "Combining cellular automata and Lattice Boltzmann method to model multiscale avascular tumor growth coupled with nutrient diffusion and immune competition," *Journal of Immunological Methods*, vol. 376, no. 1–2, pp. 55–68, 2012.
- [13] D. E. Kirschner, D. Young, and J. L. Flynn, "Tuberculosis: global approaches to a global disease," *Current Opinion in Biotechnology*, vol. 21, no. 4, pp. 524–531, 2010.
- [14] D. Kirschner and S. Marino, "Mycobacterium tuberculosis as viewed through a computer," *Trends in Microbiology*, vol. 13, no. 5, pp. 206–211, 2005.
- [15] P. L. Lin, D. Kirschner, and J. L. Flynn, "Modeling pathogen and host: *in vitro*, *in vivo* and *in silico* models of latent *Mycobacterium tuberculosis* infection," *Drug Discovery Today: Disease Models*, vol. 2, no. 2, pp. 149–154, 2005.
- [16] J. L. Segovia-Juarez, S. Ganguli, and D. Kirschner, "Identifying control mechanisms of granuloma formation during *M. tuberculosis* infection using an agent-based model," *Journal of Theoretical Biology*, vol. 231, no. 3, pp. 357–376, 2004.
- [17] S. Hardy and P. N. Robillard, "Modeling and simulation of molecular biology systems using petri nets: modeling goals of various approaches," *Journal of Bioinformatics and Computational Biology*, vol. 2, no. 4, pp. 595–613, 2004.
- [18] D. Tsavachidou and M. N. Liebman, "Modeling and simulation of pathways in menopause," *Journal of the American Medical Informatics Association*, vol. 9, no. 5, pp. 461–471, 2002.
- [19] M. Peleg, I. S. Gabashvili, and R. B. Altman, "Qualitative models of molecular function: linking genetic polymorphisms of tRNA to their functional sequelae," *Proceedings of the IEEE*, vol. 90, no. 12, pp. 1875–1886, 2002.
- [20] E. L. Benard, A. M. Van Der Sar, F. Ellett, G. J. Lieschke, H. P. Spaink, and A. H. Meijer, "Infection of zebrafish embryos with intracellular bacterial pathogens," *Journal of Visualized Experiments*, no. 61, pp. 1–8, 2012.
- [21] C. T. Yang, C. J. Cambier, J. M. Davis, C. J. Hall, P. S. Crosier, and L. Ramakrishnan, "Neutrophils exert protection in the early tuberculous granuloma by oxidative killing of mycobacteria phagocytosed from infected macrophages," *Cell Host & Microbe*, vol. 12, no. 3, pp. 301–312, 2012.
- [22] N. van der Wel, D. Hava, D. Houben et al., "*M. tuberculosis* and *M. leprae* translocate from the phagolysosome to the cytosol in myeloid cells," *Cell*, vol. 129, no. 7, pp. 1287–1298, 2007.
- [23] V. Sundaramurthy and J. Pieters, "Interactions of pathogenic mycobacteria with host macrophages," *Microbes and Infection*, vol. 9, no. 14–15, pp. 1671–1679, 2007.
- [24] C. M. Rosenberger and B. B. Finlay, "Phagocyte sabotage: disruption of macrophage signalling by bacterial pathogens," *Nature Reviews Molecular Cell Biology*, vol. 4, no. 5, pp. 385–396, 2003.
- [25] E. J. M. Stoop, T. Schipper, S. K. Rosendahl Huber et al., "Zebrafish embryo screen for mycobacterial genes involved in the initiation of granuloma formation reveals a newly identified ESX-1 component," *Disease Models and Mechanisms*, vol. 4, no. 4, pp. 526–536, 2011.
- [26] J. M. Davis, D. A. Haake, and L. Ramakrishnan, "Leptospira interrogans stably infects zebrafish embryos, altering phagocyte behavior and homing to specific tissues," *PLoS Neglected Tropical Diseases*, vol. 3, no. 6, article e463, 2009.
- [27] R. Lesley and L. Ramakrishnan, "Insights into early mycobacterial pathogenesis from the zebrafish," *Current Opinion in Microbiology*, vol. 11, no. 3, pp. 277–283, 2008.
- [28] L. Cardelli, "Brane calculi interactions of biological membranes," in *Proceedings of the International Conference on Computational Methods in Systems Biology (CMSB '04)*, vol. 3082, pp. 257–278, May 2004.
- [29] A. Regev, W. Silverman, and E. Shapiro, "Representation and simulation of biochemical processes using the pi-calculus process algebra," *Proceedings of the Pacific Symposium on Biocomputing*, pp. 459–470, 2001.
- [30] V. N. Reddy, M. L. Mavrovouniotis, and M. N. Liebman, "Petri net representations in metabolic pathways," in *Proceedings of the International Conference on Intelligent Systems for Molecular Biology (ISMB '93)*, vol. 1, pp. 328–336, January 1993.
- [31] R. V. Carvalho, W. Davids, A. H. Meijer, and F. J. Verbeek, "Spatio-temporal modeling and simulation of mycobacterium pathogenesis using petri nets," in *Bio-Inspired Models of Networks, Information, and Computing Systems*, vol. 103 of *Lecture Notes of the Institute for Computer Sciences, Social Informatics and Telecommunications Engineering*, pp. 236–241, 2012.
- [32] M. Heiner, D. Gilbert, and R. Donaldson, "Petri nets for systems and synthetic biology," *Formal Methods for Computational Systems Biology*, vol. 5016, pp. 215–264, 2008.
- [33] J. Desel and G. Juhás, "What Is a Petri Net?" Informal answers for the informed reader," *Unifying Petri Nets*, vol. 2128, pp. 1–25, 2001.
- [34] K. Jensen and L. M. Kristensen, *Coloured Petri Nets*, vol. 254, Springer, Berlin, Germany, 2009.
- [35] I. Mura and A. Csikász-Nagy, "Stochastic Petri Net extension of a yeast cell cycle model," *Journal of Theoretical Biology*, vol. 254, no. 4, pp. 850–860, 2008.
- [36] H. Alla and R. David, "Continuous and hybrid Petri nets," *Journal of Circuits, Systems and Computers*, vol. 8, no. 1, pp. 159–188, 1998.
- [37] F. Liu and M. Heiner, "Colored Petri nets to model and simulate biological systems," in *Proceedings of the Workshops of the 31st International Conference on Application and Theory of Petri Nets and Other Models of Concurrency (PETRI NETS '10)*, vol. 827 of *CEUR Workshop*, pp. 71–85, 2010.
- [38] M. Heiner, R. Richter, M. Schwarick, and C. Rohr, "Snoopy-a tool to design and execute graph-based formalisms," *Petri Net Newsletter*, vol. 74, pp. 8–22, 2008.
- [39] D. Gammack, S. Ganguli, S. Marino, J. Segovia-Juarez, and D. E. Kirschner, "Understanding the immune response in tuberculosis using different mathematical models and biological

- scales,” *Multiscale Modeling and Simulation*, vol. 3, no. 2, pp. 312–345, 2005.
- [40] S. Marino, J. J. Linderman, and D. E. Kirschner, “A multifaceted approach to modeling the immune response in tuberculosis,” *Wiley Interdisciplinary Reviews: Systems Biology and Medicine*, vol. 3, no. 4, pp. 479–489, 2011.
- [41] A. Franzke, *Charlie 2.0—A Multi-Threaded Petri Net Analyzer*, Brandenburg University of Technology at Cottbus, 2009.
- [42] A. E. Nezhinsky, E. Stoop, A. A. Vasylevska, A. van der Sar, and F. J. Vebeek, “Spatial analysis of bacterial infection patterns in Zebrafish,” in *Proceedings of the 21th Annual Belgian-Dutch Conference on Machine Learning*, pp. 27–32, 2012.

Research Article

Computational Modeling of Microabscess Formation

Alexandre Bittencourt Pigozzo,¹ Gilson Costa Macedo,² Rodrigo Weber dos Santos,¹ and Marcelo Lobosco¹

¹ Graduate Program in Computational Modeling, UFJF, Rua José Lourenço Kelmer s/n, Campus Universitário, Bairro São Pedro, 36036-900 Juiz de Fora, MG, Brazil

² Graduate Program in Biological Sciences, UFJF, Rua José Lourenço Kelmer s/n, Campus Universitário, Bairro São Pedro, 36036-900 Juiz de Fora, MG, Brazil

Correspondence should be addressed to Alexandre Bittencourt Pigozzo, alexbpr@gmail.com

Received 29 June 2012; Revised 28 August 2012; Accepted 5 September 2012

Academic Editor: Vladimir Brusic

Copyright © 2012 Alexandre Bittencourt Pigozzo et al. This is an open access article distributed under the Creative Commons Attribution License, which permits unrestricted use, distribution, and reproduction in any medium, provided the original work is properly cited.

Bacterial infections can be of two types: acute or chronic. The chronic bacterial infections are characterized by being a large bacterial infection and/or an infection where the bacteria grows rapidly. In these cases, the immune response is not capable of completely eliminating the infection which may lead to the formation of a pattern known as microabscess (or abscess). The microabscess is characterized by an area comprising fluids, bacteria, immune cells (mainly neutrophils), and many types of dead cells. This distinct pattern of formation can only be numerically reproduced and studied by models that capture the spatiotemporal dynamics of the human immune system (HIS). In this context, our work aims to develop and implement an initial computational model to study the process of microabscess formation during a bacterial infection.

1. Introduction

The immune system is one of the most important and complex system of our organism. Despite great advances in recent years that shed light on its understanding and unravel the underlying key mechanisms behind its functions, there are still many functions of the human immune system (HIS) that are not well understood. Computational models of HIS dynamics can contribute to a better understanding of the relationship between cells and molecules of the HIS.

In this study, we developed a mathematical model of some cells and molecules of the HIS to reproduce the spatiotemporal dynamics of the initial formation of microabscesses during an immune response to a bacteria.

To reproduce these dynamics, we introduce a mathematical model composed of a system of partial differential equations (PDEs) that extends our previous models [1, 2] and defines the dynamics of representative cells and molecules of the HIS during the immune response to a bacteria. The model presented is descriptive, mechanistic, and deterministic; therefore, it enables the understanding of how different complex phenomena, structures, and elements

interact during an immune response. In addition, the model's parameters reflect the physiological features of the system, making the model appropriate for general use.

The remainder of this paper is organized as follows. First, the necessary biological background is presented. Next, related works are briefly discussed. This exposition is followed by a description of the mathematical model proposed in this work and the numerical scheme used to implement it. Then simulation results obtained from the proposed model are discussed, and, finally, our conclusions and plans for future work are presented.

2. Biological Background

The initial response of the host to a diverse array of biological stressors including bacterial infection, burns, trauma, and invasive surgery is an inflammatory response. Despite the growing understanding of the cellular and molecular mechanisms of inflammation, the complexity of the inflammatory response has challenged therapeutic development [3, 4]. A key reason for this conundrum has been speculated to

be the difficulty of predicting the impact of manipulating individual components of the highly complex, nonlinear, and redundant inflammatory response [5]. Thus, progress would require a greater understanding of how components are organized. This makes systems biology based approaches appealing [6].

Most inflammatory reactions begin as a suppurative or purulent exudation process when the first line of cellular defense, the neutrophils, accumulate in the area. A suppurative process is characterized by the presence of pus (neutrophils mixed with cellular debris). Classically, there are three requisites of suppuration:

- (i) presence of neutrophils that release proteolytic enzymes,
- (ii) necrosis of some types,
- (iii) liquefaction.

This suppurative process may lead to the formation of microabscesses. A microabscess is a localized collection of dead cells, body fluids, microbes, and other cells of the HIS. The process of formation of a microabscess begins when a cell of the HIS encounters bacteria and warn other cells that there is a stranger in the host. Its “warn” is in the form of a class of biochemicals called cytokines, which beckon other HIS cells to come to the point of infection and surround the enemy.

Most often all this goes unnoticed because the first few immune system cells phagocytize (engulf and digest) the invaders and the battle is finished. But every so often, an invader has a trick to escape the immune response and cannot be killed by the phagocytes. Those bacteria continue to grow and to spew out whatever they do. More and more immune system cells, mainly neutrophils, congregate at the infection site trapping the pathogens in the center. If this microabscess is close enough to the body surface, it can be seen as a blob of pus under the skin. When a microabscess is well developed, it has a wall or capsule of fibrous connective tissue separating it from the surrounding tissue, helping to prevent any microbes present in the microabscess from spreading to other areas of the body. Thus, microabscesses can be considered as a natural strategy used to fight against infection.

Microabscesses are found in many different diseases, for instance, the authors in [7–10] present animal studies detailing the formation of liver microabscess and microabscess by different types of infections. Epidermal microabscess formation by neutrophils was also evaluated in [11–14]. Infection of the heart by bacteria (bacterial myocarditis [15]) or by viruses (viral myocarditis [16]) is also correlated with microabscess formation by neutrophils. The interaction between tumor cells and inflammatory cells plays an important role in cancer initiation and progression and was investigated in [17] for the case of tumor-infiltrating neutrophils in pancreatic neoplasia, where the pattern of microabscess formation by neutrophils was reported once again.

3. Related Work

This section presents and discusses other mathematical and computational models of the immune response. Essentially, two distinct approaches are used: agent-based models and ordinary differential equations (ODEs). These models have some features in common with our model. All models include representative cells and molecules of the innate immune system. For example, neutrophils, macrophages, and proinflammatory cytokines are modeled in the majority of models. Some models as our model consider the important interactions between endothelial cells, tissue cells, and cytokines. Despite some similarities with our model, none of the works focus on modeling microabscesses.

4. Models Based on Agents

In [18, 19], it was developed an agent-based model of the dynamics of some cells, such as polymorphonuclear leukocytes (PMNs) and mononuclear cells and molecules, such as $\text{TNF-}\alpha$ and IL-1, during the initial inflammatory response in the interface endothelium/blood at the capillary level. Some characteristics of the model are as follows:

- (i) all the cells are represented as agents whose behavior is close to the real;
- (ii) it considers the interactions between endothelial cells and circulating inflammatory cells at the blood/blood vessel-lining interface;
- (iii) the initial injury number (IIN) defines the number of tissue cells that are dead initially;
- (iv) the oxygen concentration is one important variable in the model;
- (v) the total tissue damage is represented as a deficit in the oxygen variable;
- (vi) the injury state of an endothelial cell depends on the available oxygen concentration;
- (vii) proinflammatory mediators and endothelial cells surface adhesion molecules are modeled by state variables;
- (viii) it considers a generic pathogen that causes the infection.

The work aims to reproduce the time course of the early inflammatory response associated with the Systemic Inflammatory Syndrome Response (SIRS)/Multiple Organ Failure (MOF) from massive trauma or large exposure to endotoxin. The objective of the simulations were to compare the results with the soluble TNF-receptor experiment [20] where the soluble TNF-receptor is tested as a therapeutic treatment for the sepsis. The author claims that his results generally replicate the results of several large-scale clinical trials of cytokine-directed antimediator agents.

In [6], an agent-based modeling (ABM) framework is proposed to study the nonlinear dynamics of acute inflammatory responses to LPS. Their work uses an agent-based approach to elucidate molecular interactions involved

TABLE 1: Initial conditions.

Parameter	Value	Unit
B_0	$\begin{cases} 70 : x = 2.5 \text{ mm}, y = 2.5 \text{ mm} \\ 0 : \text{otherwise} \end{cases}$	10^4 cells/mm^3
BD_0	$0 : 0 \leq x \leq 4, 0 \leq y \leq 4$	10^4 cells/mm^3
RM_0	$\begin{cases} 10 : x = 1 \text{ mm}, y = 1 \text{ mm} \\ 10 : x = 1 \text{ mm}, y = 4 \text{ mm} \\ 10 : x = 4 \text{ mm}, y = 2.5 \text{ mm} \\ 0 : \text{otherwise} \end{cases}$	10^4 cells/mm^3
AM_0	$0 : 0 \leq x \leq 4, 0 \leq y \leq 4$	10^4 cells/mm^3
N_0	$0 : 0 \leq x \leq 4, 0 \leq y \leq 4$	10^4 cells/mm^3
ND_0	$0 : 0 \leq x \leq 4, 0 \leq y \leq 4$	10^4 cells/mm^3
CH_0	$0 : 0 \leq x \leq 4, 0 \leq y \leq 4$	10^4 cells/mm^3
HT_0	$10 : 0 \leq x \leq 4, 0 \leq y \leq 4$	cells/mm^3
TD_0	$0 : 0 \leq x \leq 4, 0 \leq y \leq 4$	10^4 cells/mm^3

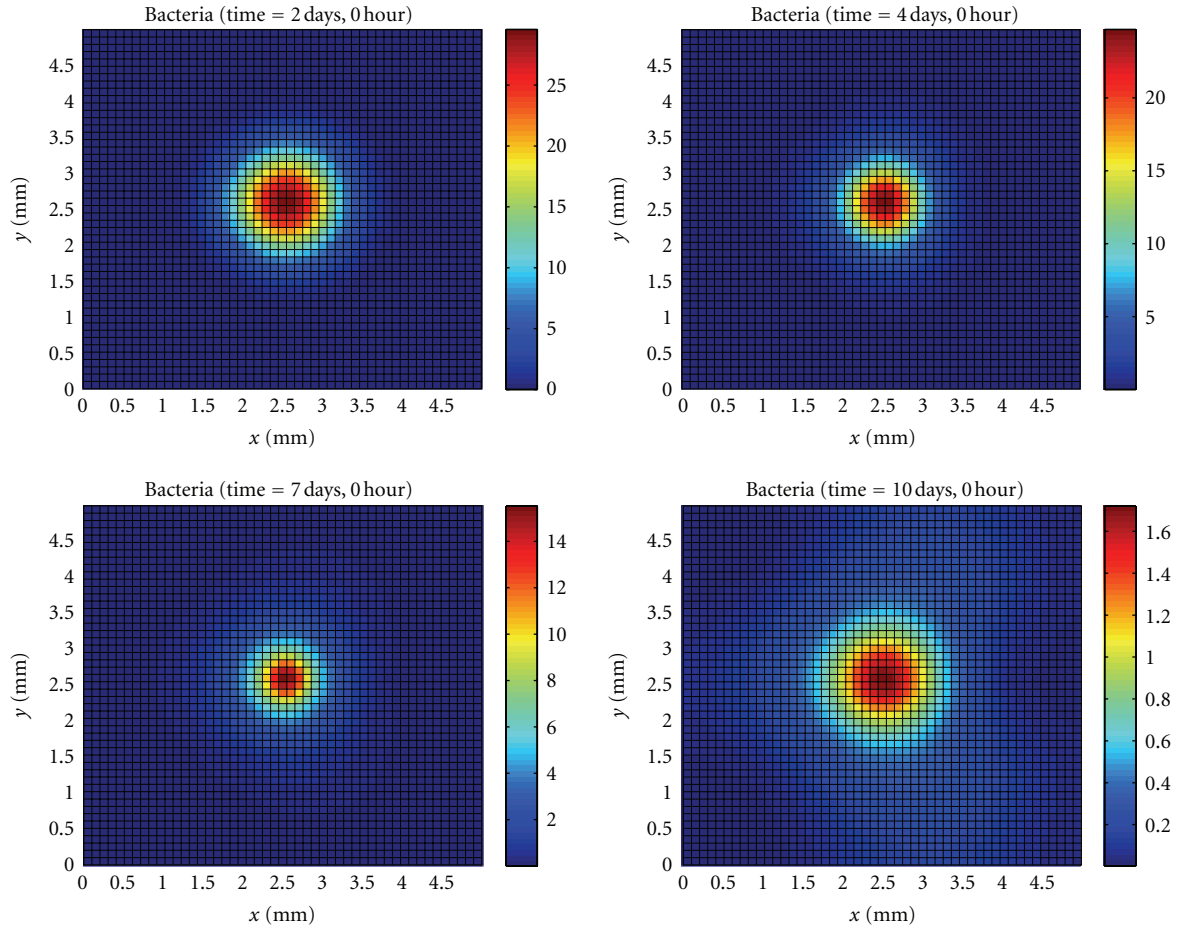


FIGURE 1: Temporal evolution and spatial distribution of bacteria.

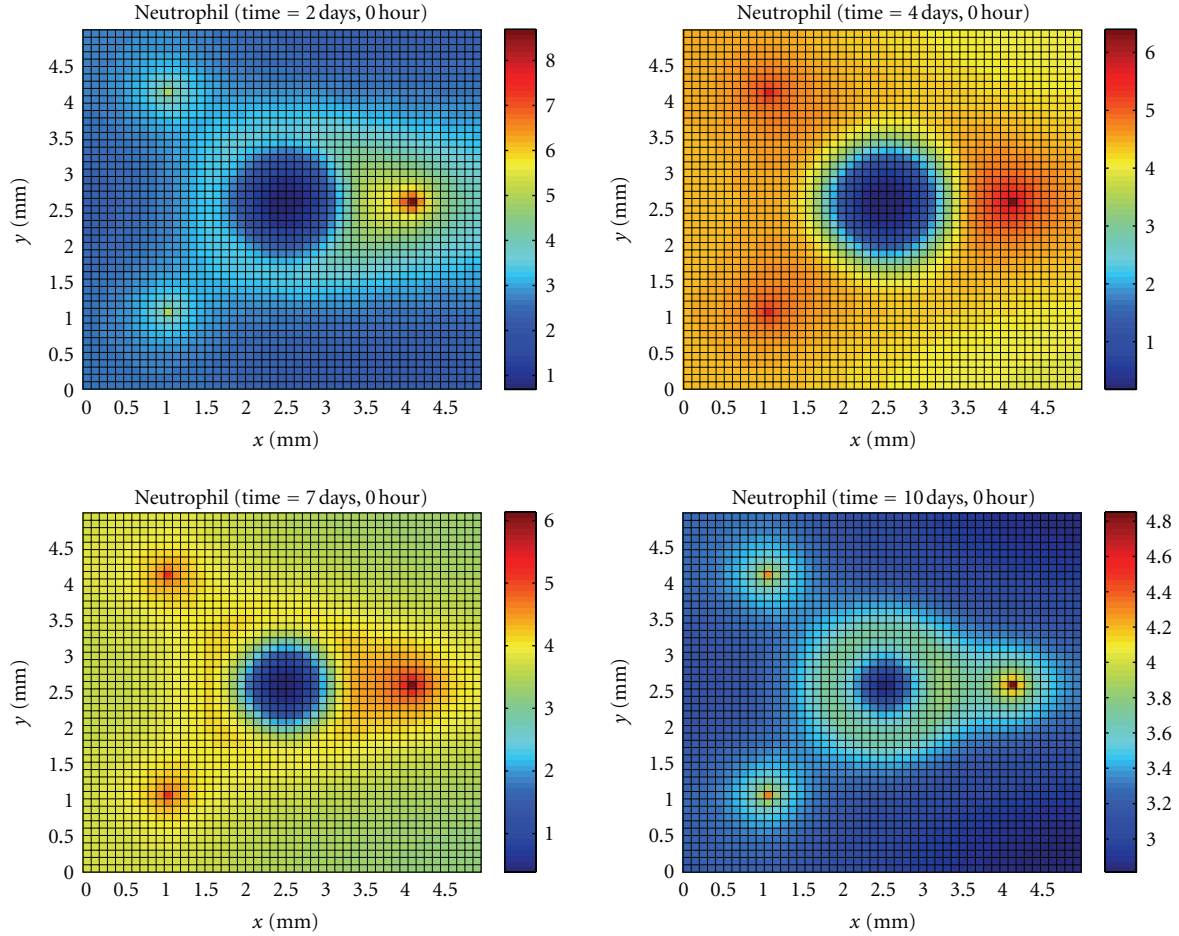


FIGURE 2: Temporal evolution and spatial distribution of neutrophil.

in the $\text{NF-}\kappa\beta$ signaling pathway, coupled with the spatial orientation of various inflammation specific molecules and cell populations such as macrophages and T-helper cells. In their model, the propagation of LPS signaling across the system is studied by considering the coupling between extracellular signals and transcriptional response. Some relevant characteristics considered in the model are as follows:

- (i) molecular interactions,
- (ii) cellular heterogeneity,
- (iii) LPS/TLR4 signal transduction pathway,
- (iv) transcriptional response.

The proposed *in silico* model is evaluated through its ability to successfully reproduce a self-limited inflammatory response as well as a series of scenarios: a persistent (non)infectious response or innate immune tolerance and potentiation effects followed by perturbations in intracellular signaling molecules and cascades.

5. Models Based on ODEs

The model of [21] studies immunomodulatory strategies for treating cases of severe sepsis. They introduced and

evaluated the concept of conducting a randomized clinical trial *in silico* based on simulated patients generated from a mechanistic mathematical model of bacterial infection, acute inflammatory response, global tissue dysfunction, and a therapeutic intervention. Trial populations are constructed to reflect heterogeneity in bacterial load and virulence as well as propensity to mount and modulate an inflammatory response. They constructed a cohort of 1000 trial patients submitted to therapy with one of three different doses of a neutralizing antibody directed against tumor necrosis factor (anti-TNF) for 6, 24, or 48 hrs. Their focus was to assess the feasibility of using differential equation models to improve the design of clinical trials. This paper replicates *in silico* the general findings from actual clinical trials—that it is very difficult to design a treatment strategy that is effective over a broad range of sepsis patients.

6. Hybrid Models

In [22], a hybrid model that coupled an agent-based model [18, 19] and a system dynamics/differential equation model [21] was created using the System Dynamics tool within Netlogo [23]. They developed an interface between the agent-based and system dynamics models. The area of

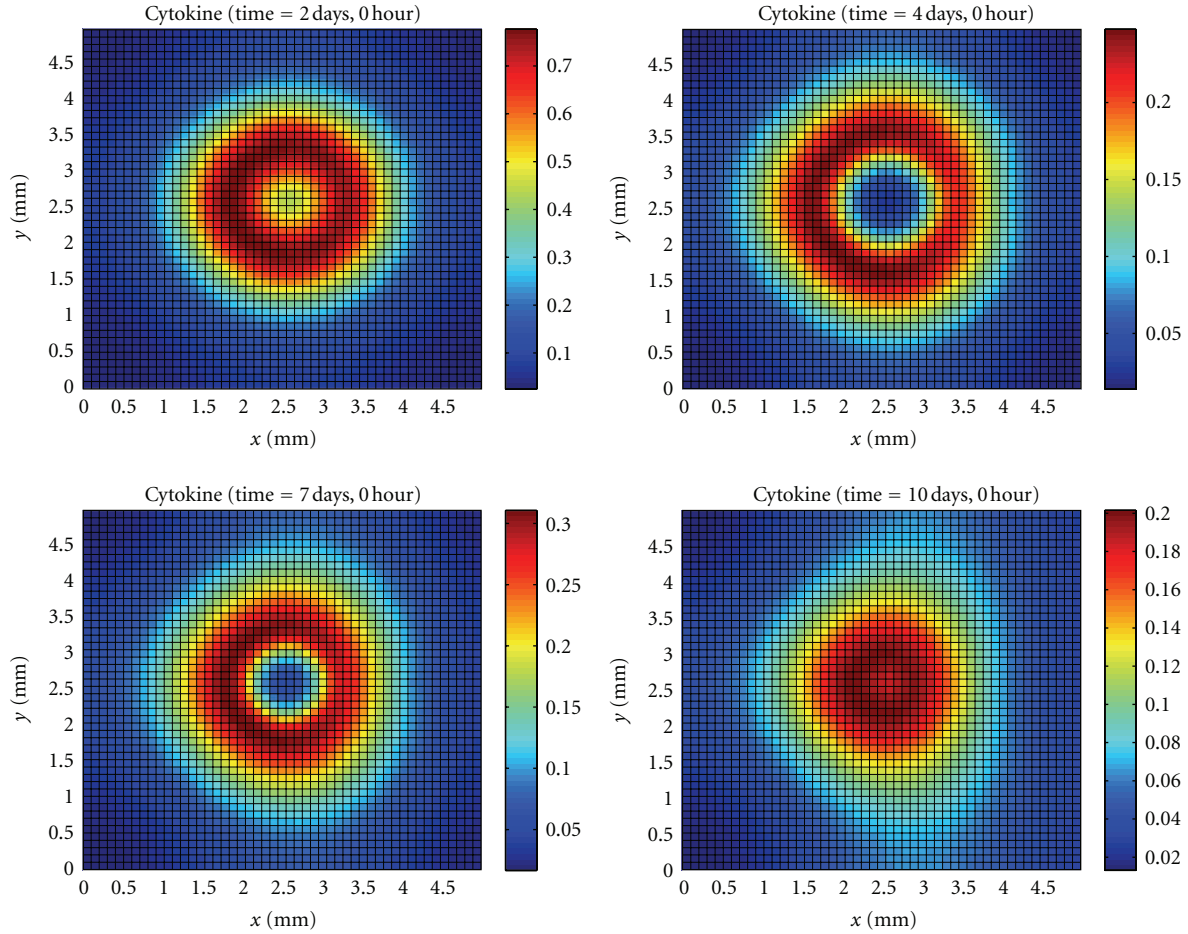


FIGURE 3: Temporal evolution and spatial distribution of cytokine.

initial infection and subsequent interactions at this point were simulated with the agent-based model and certain aspects primarily related to the production and life cycle of circulating inflammatory cells was modeled with the system dynamics model. They implemented a simple system dynamics model that focused on systemic polymorphonuclear neutrophils (PMN) production, maturation, sequestration, and release. Some of the flows inside the system dynamics model were influenced by the conditions within the agent-based model. The primary role of the system dynamics model was to manifest a delay between the elevation of the cytokines in the tissue and the increase in PMNs in the circulating blood. The objective of the work was to reproduce some of the results of the agent-based model [18, 19] using the hybrid model.

7. Mathematical Model

Our main objective is to develop a parameterized mathematical model of the human innate immune system that simulates the immune response occurring in a generic tissue. To achieve this goal, we first build a model of the immune response to LPS [1, 2]. In this work, we extend this model to reproduce the spatiotemporal dynamics of a bacterial infection and the process of microabscess formation.

The mathematical model simulates the temporal and spatial behavior of bacteria (B), dead bacteria (BD), macrophages, neutrophils (N), apoptotic neutrophils (ND), proinflammatory cytokines (CH), healthy tissue cells (HT), and dead tissue cells (TD). Macrophages are present in two states of readiness: resting (RM) and *hyperactivated* (AM). We must stress that the equations modeling proinflammatory cytokines are generic in the sense that they model the role of distinct cytokines taking part in the inflammatory process. Equation parameters can be adjusted to model the role of a specific proinflammatory cytokine.

The relationships among all of the model's components are described next. Neutrophils, resting macrophages, and active macrophages phagocytose the bacteria. The neutrophils then undergo apoptosis, which may or may not be induced by the phagocytosis process. In this different state, apoptotic neutrophils cannot perform phagocytosis or produce proinflammatory cytokines; as a result, apoptotic neutrophils are eliminated from the body after being phagocytosed by active macrophages. Apoptotic neutrophils will die after a period of time, releasing cytotoxic granules and degradation enzymes in the medium that cause tissue damage destroying healthy tissue cells. Active neutrophils and bacteria also cause tissue damage by producing toxic

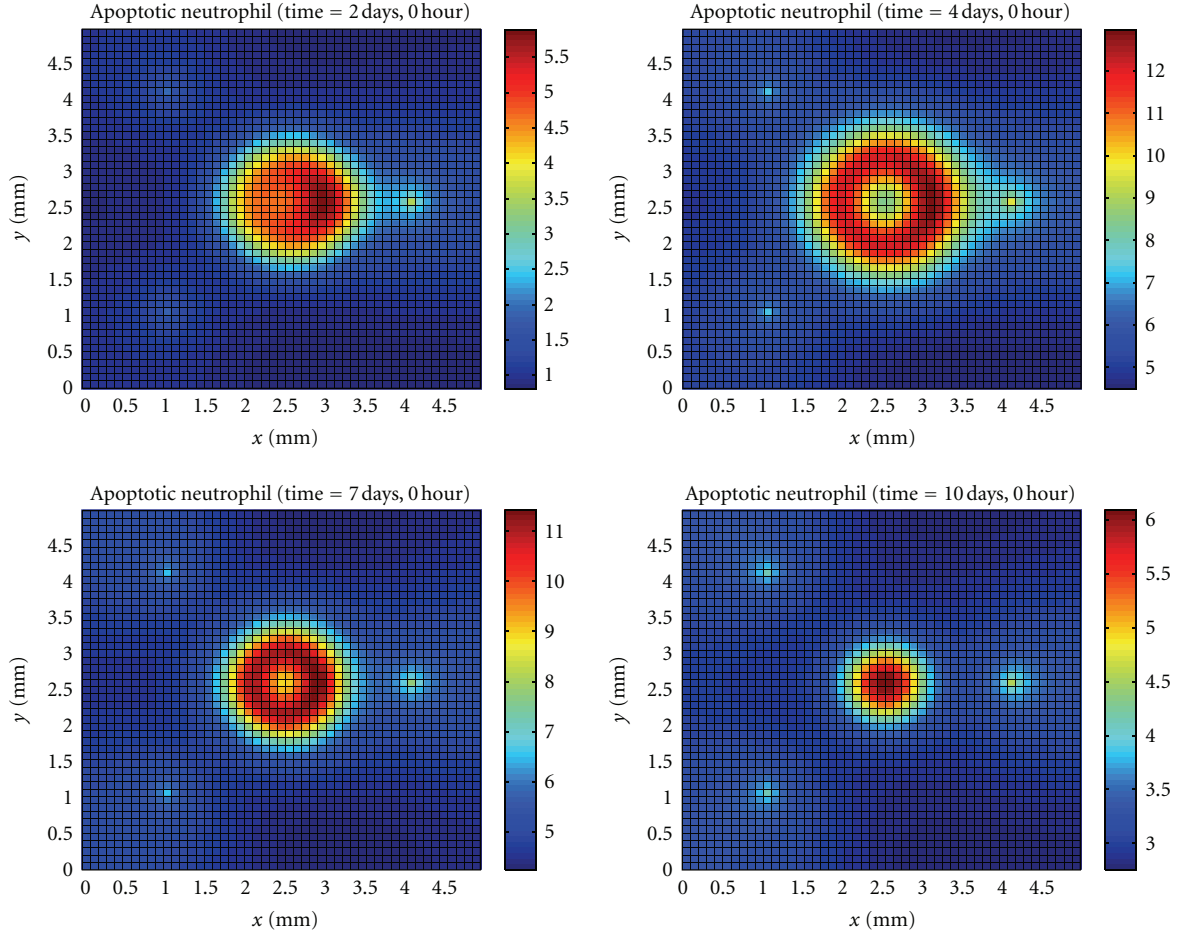


FIGURE 4: Temporal evolution and spatial distribution of apoptotic neutrophil.

products that are not modeled here. The infection site is “cleaned” by resting and active macrophages that do the phagocytosis of dead tissue cells. Healthy tissue cells in contact with bacteria, neutrophils, and active macrophages produce proinflammatory cytokines. The proinflammatory cytokines increase the permeability of the blood vessels; consequently, more neutrophils and monocytes are recruited to the infected tissue. In addition, the proinflammatory cytokines act as a chemoattractant substance to the resting macrophages, active macrophages, and neutrophils.

Below, we provide the equations derived from the model. Equation (1) provides the bacteria differential equation:

$$\begin{aligned}
 \frac{\partial B}{\partial t} = & r_B \cdot B \cdot g(w) - \mu_B \cdot B - \lambda_{N|B} \cdot N \cdot B \\
 & - \lambda_{RM|B} \cdot RM \cdot B - \lambda_{AM|B} \cdot AM \cdot B \\
 & + D_B \cdot \text{dif}(B, w),
 \end{aligned} \quad (1)$$

$$B(x, y, 0) = B_0, \quad \left. \frac{\partial B(\cdot, t)}{\partial n} \right|_{\partial \Omega} = 0.$$

In this equation, $r_B \cdot B \cdot g(w)$ denotes the reproduction term of the bacteria, where r_B is the rate of reproduction and $g(w)$ is a function of the total density of cells w in a

discretized area of the two-dimensional space at a specific time step. The w variable is defined as

$$\begin{aligned}
 w(x, y, t) = & B(x, y, t) + BD(x, y, t) + N(x, y, t) \\
 & + ND(x, y, t) + RM(x, y, t) + AM(x, y, t) \\
 & + CH(x, y, t) + HT(x, y, t) + TD(x, y, t);
 \end{aligned} \quad (2)$$

$\mu_B \cdot B$ denotes the decay of bacteria, where μ_B is the rate of decay. $\lambda_{N|B} \cdot N \cdot B$ denotes the phagocytosis of bacteria by neutrophils, where $\lambda_{N|B}$ is the rate of this phagocytosis. $\lambda_{RM|B} \cdot RM \cdot B$ denotes the phagocytosis of bacteria by resting macrophages, where $\lambda_{RM|B}$ is the rate of this phagocytosis. $\lambda_{AM|B} \cdot AM \cdot B$ denotes the phagocytosis of bacteria by active macrophages, where $\lambda_{AM|B}$ is the rate of this phagocytosis. $D_B \cdot \text{dif}(B, w)$ denotes bacteria diffusion, where D_B represents the diffusion coefficient and $\text{dif}(B, w)$ is calculated in the following way:

$$\text{dif}(B, w) = \nabla \cdot (g(w) \nabla (f(w)B) - f(w)B \nabla g(w)). \quad (3)$$

The f function models the probability of a cell being pushed from a site due to the pressure exerted by neighboring cells [24, 25]. This population pressure is modelled by a Hill equation [26]. It increases with the total density of cells w

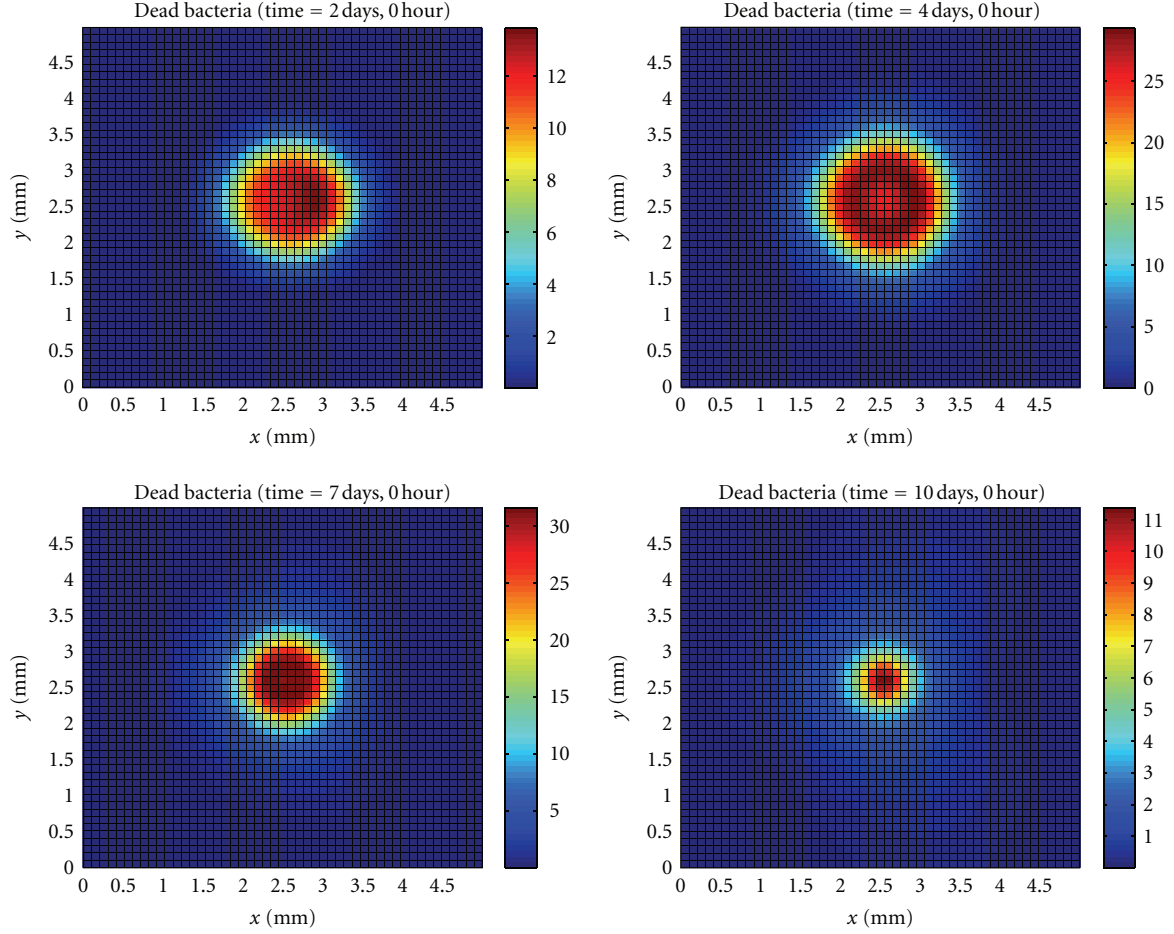


FIGURE 5: Temporal evolution and spatial distribution of dead bacteria.

occupying the same position in space and has a saturation in a high density of cells.

The f function is defined as

$$f(w) = 1 + \alpha \frac{w}{\beta + w}. \quad (4)$$

α and β are constant values.

The g function returns the percentage of free space in a discretized area of the two-dimensional space and its use is motivated by some important biological concepts such as quorum sensing/volume sensing [24, 25, 27–29]. The idea is that cells have a set of cell density sensing mechanisms and changes its behavior in crowded regions. In the context of our model it is used to limit the density of cells that occupy a discretized area of our two-dimensional domain. The g function is defined as

$$g(w) = 1 - \frac{w}{\text{total}}. \quad (5)$$

The variable total represents the maximum density of cells that fits in a discretized area of the tissue.

The differential equation corresponding to dead bacteria (BD) is given as follows:

$$\begin{aligned} \frac{\partial \text{BD}}{\partial t} = & \mu_B \cdot B + \lambda_{N|B} \cdot N \cdot B + \lambda_{\text{RM}|B} \cdot \text{RM} \cdot B \\ & + \lambda_{\text{AM}|B} \cdot \text{AM} \cdot B - \lambda_{\text{AM}|BD} \cdot \text{AM} \cdot \text{BD} \\ & - \lambda_{\text{RM}|BD} \cdot \text{RM} \cdot \text{BD} + D_{\text{BD}} \cdot \text{dif}(\text{BD}, w), \end{aligned} \quad (6)$$

$$\text{BD}(x, y, 0) = B_0, \quad \left. \frac{\partial \text{BD}(\cdot, t)}{\partial n} \right|_{\partial \Omega} = 0.$$

Here, note that $\mu_B \cdot B$, $\lambda_{N|B} \cdot N \cdot B$, $\lambda_{\text{RM}|B} \cdot \text{RM} \cdot B$ and $\lambda_{\text{AM}|B} \cdot \text{AM} \cdot B$ were defined previously. $\lambda_{\text{AM}|BD} \cdot \text{AM} \cdot \text{BD}$ denotes the phagocytosis of dead bacteria by active macrophages, where $\lambda_{\text{AM}|BD}$ is the rate of phagocytosis. $\lambda_{\text{RM}|BD} \cdot \text{RM} \cdot \text{BD}$ denotes the phagocytosis of dead bacteria by resting macrophages, where $\lambda_{\text{RM}|BD}$ is the rate of phagocytosis. $D_{\text{BD}} \cdot \text{dif}(\text{BD}, w)$ denotes dead bacteria diffusion, where D_{BD} represents the diffusion coefficient and the function dif was defined previously.

The differential equation corresponding to the resting macrophage (RM) is given as follows:

$$\begin{aligned}
 P_{RM} &= (P_{RM}^{\max} - P_{RM}^{\min}) \cdot \frac{CH}{(CH + \text{keq}_{CH})} + P_{RM}^{\min}, \\
 \text{source}_{RM} &= P_{RM} \cdot (M^{\max} - (RM + AM)), \\
 \frac{\partial RM}{\partial t} &= -\mu_{RM} \cdot RM - \lambda_{B|RM} \cdot B \cdot RM + \text{source}_{RM} \cdot g(w) \\
 &\quad + D_{RM} \cdot \text{dif}(RM, w) \\
 &\quad - \chi_{RM} \cdot \text{chemotaxis}(RM, CH, w), \\
 RM(x, y, 0) &= RM_0, \quad \left. \frac{\partial RM(\cdot, t)}{\partial n} \right|_{\partial\Omega} = 0.
 \end{aligned} \tag{7}$$

P_{RM} denote the increase in endothelium permeability and its effects on monocyte extravasation. The permeability of blood vessel endothelium is modeled by a Hill equation [26], which also has been used to model drug dose-response relationships [30]. The idea is to model the increase in the permeability of the endothelium in accordance with the number of proinflammatory cytokines deposited on the endothelium.

The calculation of P_{RM} involves the following parameters: (a) P_{RM}^{\max} , the maximum endothelium permeability induced by the proinflammatory cytokine; (b) P_{RM}^{\min} , the minimum endothelium permeability induced by the proinflammatory cytokine; (c) keq_{CH} , the number of proinflammatory cytokines that exert 50% of the maximum effect on permeability. $\text{source}_{RM} \cdot g(w)$ denotes the source term of macrophages, which is related to the number of monocytes that will enter into the tissue from the blood vessels. This number depends on the endothelium permeability P_{RM} and on the number of monocytes appearing in the blood (M^{\max}).

$\mu_{RM}RM$ denotes resting macrophage apoptosis, where μ_{RM} is the apoptosis rate. $\lambda_{B|RM} \cdot B \cdot RM$ denotes the activation of resting macrophages, where $\lambda_{B|RM}$ is the rate of activation. $D_{RM} \cdot \text{dif}(RM, w)$ denotes resting macrophage diffusion, where D_{RM} represents the diffusion coefficient and the function dif was defined previously. $\chi_{RM} \cdot \text{chemotaxis}(RM, CH, w)$ denotes resting macrophage chemotaxis, where χ_{RM} is the chemotaxis rate and $\text{chemotaxis}(RM, CH, w)$ is calculated in the following way:

$$\text{chemotaxis}(RM, CH, w) = \nabla \cdot (RMg(w)f(w)\nabla CH). \tag{8}$$

The differential equation corresponding to the active macrophage (AM) is given as follows:

$$\begin{aligned}
 \frac{\partial AM}{\partial t} &= -\mu_{AM} \cdot AM + \lambda_{B|RM} \cdot B \cdot RM + D_{AM} \\
 &\quad \cdot \text{dif}(AM, w) - \chi_{AM} \cdot \text{chemotaxis}(AM, CH, w), \\
 AM(x, y, 0) &= AM_0, \quad \left. \frac{\partial AM(\cdot, t)}{\partial n} \right|_{\partial\Omega} = 0.
 \end{aligned} \tag{9}$$

TABLE 2: Parameters.

Parameter	Value	Unit	Reference
α	0.05	Adimensional	Estimated*
β	35	Cells/mm ³	Estimated*
Total	70	Cells/mm ³	Estimated*
M^{\max}	15000	Cells/mm ³	[44]**
N^{\max}	250000	Cells/mm ³	[44]**
P_N^{\max}	1	1/day	[45]**
P_{RM}^{\max}	1	1/day	Estimated*
P_N^{\min}	0.001	1/day	Estimated*
P_{RM}^{\min}	0.01	1/day	Estimated*
keq_{CH}	5	Cells/mm ³	Estimated*
r_B	4	1/day	[46]
$\lambda_{B HT}$	0.05	1/(cells/mm ³)·day	[47]
$\lambda_{AM BD}$	0.6	1/(cells/mm ³)·day	[47]**
$\lambda_{AM ND}$	0.8	1/(cells/mm ³)·day	[44]
$\lambda_{AM TD}$	0.6	1/(cells/mm ³)·day	[47]**
$\lambda_{RM BD}$	0.6	1/(cells/mm ³)·day	[47]**
$\lambda_{RM TD}$	0.6	1/(cells/mm ³)·day	[47]**
$\lambda_{N B}$	0.55	1/(cells/mm ³)·day	[44]
$\lambda_{B N}$	0.24	1/(cells/mm ³)·day	[47]
$\lambda_{RM B}$	0.25	1/(cells/mm ³)·day	[44]
$\lambda_{AM B}$	0.8	1/(cells/mm ³)·day	[44]
μ_B	0.01	1/day	[44]
μ_N	0.67	1/day	[44]
μ_{ND}	0.05	1/day	[44]
μ_{RM}	0.0033	1/day	[44]
μ_{AM}	0.07	1/day	[44]
μ_{CH}	12	1/day	[44]
D_B	0.05	mm ² /day	[44]
D_{RM}	5	mm ² /day	[44]
D_{AM}	5	mm ² /day	[44]
D_N	10	mm ² /day	[44]
D_{ND}	0.001	mm ² /day	[44]
D_{CH}	6	mm ² /day	[44]
χ_N	10	mm ² /day	[44]
χ_{RM}	5	mm ² /day	[44]
χ_{AM}	7	mm ² /day	[44]
$\beta_{CH N}$	1	1/(cells/mm ³)·day	[48]*
$\beta_{CH AM}$	1	1/(cells/mm ³)·day	[48]*
$\beta_{CH HT}$	0.2	1/(cells/mm ³)·day	[48]*
RM_{act}	0.4	1/(cells/mm ³)·day	[44]

Here, note that $\lambda_{B|RM} \cdot B \cdot RM$ was defined previously. Above, $\mu_{AM} \cdot AM$, $D_{AM} \cdot \text{dif}(AM, w)$, and $\chi_{AM} \cdot \text{chemotaxis}(AM, CH, w)$ denote the active macrophage apoptosis, diffusion, and chemotaxis, respectively, whereas μ_{AM} , D_{AM} , and χ_{AM} are the apoptosis rate, diffusion coefficient, and chemotaxis rate, respectively.

The neutrophil differential equation (N) is given as follows:

$$\begin{aligned}
 P_N &= (P_N^{\max} - P_N^{\min}) \cdot \frac{CH}{CH + \text{keq}_{CH}} + P_N^{\min}, \\
 \text{source}_N &= P_N \cdot (N^{\max} - N),
 \end{aligned}$$

$$\begin{aligned} \frac{\partial N}{\partial t} = & -\mu_N \cdot N - \lambda_{B|N} \cdot B \cdot N + \text{source}_N \cdot g(w) \\ & + D_N \cdot \text{dif}(N, w) - \chi_N \cdot \text{chemotaxis}(N, \text{CH}, w), \\ N(x, y, 0) = N_0, \quad \frac{\partial N(\cdot, t)}{\partial n} \Big|_{\partial\Omega} = 0. \end{aligned} \quad (10)$$

In this equation, P_N denotes the increase in endothelium permeability and its effects on neutrophil extravasation. In the top equation, P_N^{\max} is the maximum endothelium permeability induced by proinflammatory cytokines, P_N^{\min} is the minimum endothelium permeability induced by proinflammatory cytokines, and keq_{CH} is the number of proinflammatory cytokines that exert 50% of the maximum effect on endothelium permeability.

Here, $\mu_N \cdot N$ denotes neutrophil apoptosis, where μ_N is the rate of apoptosis. $\lambda_{B|N} \cdot B \cdot N$ denotes the neutrophil apoptosis induced by phagocytosis, where $\lambda_{B|N}$ represents the rate of this induced apoptosis. $\text{source}_N \cdot g(w)$ represents the source term of neutrophil, that is, the number of neutrophils entering the tissue from the blood vessels. This number depends on the endothelium permeability (P_N) and on the number of neutrophils in the blood (N^{\max}).

$D_N \cdot \text{dif}(N, w)$ denotes neutrophil diffusion, where D_N represents the diffusion coefficient and the function dif was defined previously. $\chi_N \cdot \text{chemotaxis}(N, \text{CH}, w)$ denotes neutrophil chemotaxis, where χ_N is the chemotaxis rate and $\text{chemotaxis}(N, \text{CH}, w)$ was defined previously.

The differential equation corresponding to the apoptotic neutrophil (ND) is given as follows:

$$\begin{aligned} \frac{\partial \text{ND}}{\partial t} = & \mu_N \cdot N + \lambda_{B|N} \cdot B \cdot N - \lambda_{\text{ND}|AM} \cdot \text{ND} \cdot \text{AM} \\ & - \mu_{\text{ND}} \text{ND} + D_{\text{ND}} \cdot \text{dif}(\text{ND}, w), \\ \text{ND}(x, y, 0) = \text{ND}_0, \quad \frac{\partial \text{ND}(\cdot, t)}{\partial n} \Big|_{\partial\Omega} = 0. \end{aligned} \quad (11)$$

Here, note that $\mu_N \cdot N$ and $\lambda_{B|N} \cdot B \cdot N$ were defined previously, whereas $\lambda_{\text{ND}|AM} \cdot \text{ND} \cdot \text{AM}$ denotes the phagocytosis of the apoptotic neutrophil carried out by active macrophages, and $\lambda_{\text{ND}|AM}$ is the rate of this phagocytosis. $\mu_{\text{ND}} \text{ND}$ denotes the neutrophil necrosis, where μ_{ND} is the rate of necrosis. $D_{\text{ND}} \cdot \text{dif}(\text{ND}, w)$ denotes apoptotic neutrophil diffusion, where D_{ND} represents the diffusion coefficient and the function dif was defined previously.

The differential equation for the proinflammatory cytokine (CH) is given in as follows:

$$\begin{aligned} \frac{\partial \text{CH}}{\partial t} = & -\mu_{\text{CH}} \cdot \text{CH} + (\beta_{\text{CH}|N} \cdot N \cdot B + \beta_{\text{CH}|AM} \cdot \text{AM} \cdot B \\ & + \beta_{\text{CH}|HT} \cdot \text{HT} \cdot B) \cdot g(w) \\ & + D_{\text{CH}} \cdot \text{dif}(\text{CH}, w) \\ \text{CH}(x, y, 0) = \text{CH}_0, \quad \frac{\partial \text{CH}(\cdot, t)}{\partial n} \Big|_{\partial\Omega} = 0. \end{aligned} \quad (12)$$

In this equation, $\mu_{\text{CH}} \text{CH}$ denotes the proinflammatory cytokine decay, where μ_{CH} is the decay rate. $\beta_{\text{CH}|N} \cdot N \cdot B$ denotes the proinflammatory cytokine production by the neutrophils, where $\beta_{\text{CH}|N}$ is the production rate. $\beta_{\text{CH}|AM} \cdot \text{AM} \cdot B$ denotes the proinflammatory cytokine production by active macrophages, where $\beta_{\text{CH}|AM}$ is the production rate. $\beta_{\text{CH}|HT} \cdot \text{HT} \cdot B$ denotes the proinflammatory cytokine production by healthy tissue cells in contact with bacteria, where $\beta_{\text{CH}|HT}$ is the production rate. $D_{\text{CH}} \cdot \text{dif}(\text{CH}, w)$ denotes the proinflammatory cytokine diffusion, where D_{CH} represents the diffusion coefficient and the function dif was defined previously.

The differential equation corresponding to the healthy tissue (HT) is given as follows:

$$\begin{aligned} \frac{\partial \text{HT}}{\partial t} = & -\mu_{\text{ND}} \text{ND} - \lambda_{B|\text{HT}} \cdot B \cdot \text{HT}, \\ \text{HT}(x, y, 0) = \text{HT}_0, \quad \frac{\partial \text{HT}(\cdot, t)}{\partial n} \Big|_{\partial\Omega} = 0. \end{aligned} \quad (13)$$

$\mu_{\text{ND}} \text{ND}$ denotes the tissue damage caused by the release of toxic products from necrotic neutrophils. $\lambda_{B|\text{HT}} \cdot B \cdot \text{HT}$ denotes the tissue damage caused by bacteria, where $\lambda_{B|\text{HT}}$ is the rate of damage.

The differential equation corresponding to the dead tissue (TD) is given as follows:

$$\begin{aligned} \frac{\partial \text{TD}}{\partial t} = & \mu_{\text{ND}} \text{ND} + \lambda_{B|\text{HT}} \cdot B \cdot \text{HT} - \lambda_{\text{RM}|TD} \cdot \text{RM} \cdot \text{TD} \\ & - \lambda_{\text{AM}|TD} \cdot \text{AM} \cdot \text{TD}, \\ \text{TD}(x, y, 0) = \text{TD}_0, \quad \frac{\partial \text{TD}(\cdot, t)}{\partial n} \Big|_{\partial\Omega} = 0. \end{aligned} \quad (14)$$

$\mu_{\text{ND}} \text{ND}$ and $\lambda_{B|\text{HT}} \cdot B \cdot \text{HT}$ were defined previously. $\lambda_{\text{RM}|TD} \cdot \text{RM} \cdot \text{TD}$ denotes the phagocytosis of dead tissue cells by resting macrophages, where $\lambda_{\text{RM}|TD}$ is the rate of phagocytosis. $\lambda_{\text{AM}|TD} \cdot \text{AM} \cdot \text{TD}$ denotes the phagocytosis of dead tissue cells by active macrophages, where $\lambda_{\text{AM}|TD}$ is the rate of phagocytosis.

The mathematical model presented here introduced some modifications to our previous model [2] with the aim to reproduce the microabscess formation. We included equations for the dynamics of the tissue to take into account some effects of infection such as tissue damage and production of cytokines by tissue cells. We also replaced the LPS equation in our previous model [2] by the bacteria equation with a term for reproduction of bacteria. Besides we modified the calculus of the diffusion and chemotaxis terms [24] (a) to limit the number of cells that are allowed to stay at the same time in the same area of the domain and (b) to reduce the efficiency of the diffusion and chemotaxis processes in overcrowded regions. More specifically, the method we implemented incorporates the following general mechanisms which may lead to dispersal of the population [24].

- (i) Population pressure: we assume that a high cell density results in increased probability of a cell being

pushed from a site, for example, due to the pressure exerted by neighboring cells. This is achieved phenomenologically with the f function of our mathematical model and the changes in diffusion and chemotaxis calculus.

- (ii) Limited space: here we assume that no more cells can enter a site above a total cell density. In our model, this is achieved with the incorporation of the g function in the diffusion and chemotaxis calculations.
- (iii) Gradient detection: cells may detect and respond to a local gradient in the cell density and as a consequence cells can move to higher concentrations of the attractant substance.

8. Implementation

The numerical method used to solve the mathematical model was the Finite Difference Method [31], a method commonly used in the numeric discretization of PDEs.

A complex part of the resolution of the PDEs is the resolution of the convective term, the chemotaxis term. The development of numerical methods to approximate convective terms (in most cases not linear) have been subject of intense researches [32–35].

Different numerical approaches have been proposed for the discretization of the chemotaxis term [36, 37]. Our implementation is based on the finite difference method for the spatial discretization and the explicit Euler method for the time evolution. The discretization of the chemotaxis term ($\nabla \cdot (\chi_N N \nabla CH)$) uses the First-Order Upwind scheme [38]. Therefore, the precision of our numerical implementation is first-order in time (explicit Euler) and first-order in space (upwind scheme). The upwind scheme discretizes the hyperbolic PDEs through the use of differences with bias in the direction given by the signal of the characteristics' speeds. The upwind scheme uses an adaptive or solution-sensitive stencil to numerically simulate more precisely the direction of information propagation.

In two-dimension, the upwind scheme approximates the chemotaxis term as the sum of the flux in the x direction ($resX$) with the flux in the y direction ($resY$). $resX$ is the sum of the flux_left at the point $x - \Delta x/2$ with the flux_right at the point $x + \Delta x/2$ and $resY$ is the sum of the flux_up at the point $y - \Delta y/2$ with the flux_down at the point $y + \Delta y/2$ in Algorithm 1.

In this code, ch represents the discretization of the proinflammatory cytokine, n represents the discretization of neutrophils, w is the total density of cells in a position of the space, x and y are the positions in space, and Δx and Δy are the spatial discretizations in x and y directions, respectively. The test made is to define what is the signal of the characteristic speed, where the speed of the movement of $N(y, x)$ is given by the term ∇CH . This value is then used to choose between two schemes of finite differences: forward or backward.

We decided to implement our own numerical method to solve the systems of PDEs because (a) we have the possibility to parallelize the code and (b) most of the numerical libraries

offer few functions that are suitable to our problem. The sequential code was implemented in C.

9. Numerical Experiments

We performed several simulations in order to verify that the model's results are in agreement with what is described in the literature. Our objective was to reproduce some characteristics of the microabscess such as an accumulation of dead cells and bacteria in the infection site.

The model's initial conditions and parameters are given in Tables 1 and 2, respectively.

In Table 2, parameters marked with * were adjusted to qualitatively reproduce the results obtained in several studies of the immune response to LPS. In the case of the bacteria (results not shown here), we adjust the equation parameters in order to obtain an exponential decrease in time as shown in [39]. The results of the concentration of proinflammatory cytokines in time (results not shown here) are qualitatively similar to those obtained in some experimental works [40–42]. The parameters marked with ** were based on the values given in the references but were adjusted due to the use of distinct units (e.g., from liter to mm^3) or to fit in a 25 mm^2 tissue. In this paper, we obtained parameter values for humans whenever they were available. The variables β and total in (5) and (4) were defined based on the concentrations of neutrophils and macrophages per liter given in [43] and were adjusted (a) due to the use of distinct units (e.g., from liter to mm^3) and (b) to fit in a 25 mm^2 tissue. The variable total represents the maximum density of cells that fits in a discretized area of the tissue.

In the next sections, we will show the results of the simulation performed with the parameters given in Table 2. In this simulation, we considered a $5 \text{ mm} \times 5 \text{ mm}$ two-dimensional domain representing a tissue with 25 mm^2 of area and a simulation time of 5 days. In our model, the exchange between the vascular system (arterioles and vessels) and tissue was assumed to occur only at the points (1, 1), (1, 4), and (4, 2.5). In this point, immune cells (neutrophils and macrophages) that are in the blood stream can enter into the tissue. The communication between blood vessels and tissue is modeled by permeabilities that vary in time and may depend on the concentration of different cells and molecules (in our model, the endothelium permeability of neutrophils and macrophages depends on the concentration of the proinflammatory cytokine).

10. Bacteria

In the case of bacteria (Figure 1), we observe that initially the bacteria diffuses through the tissue causing tissue damage without its presence to be noticed.

As soon as resting macrophages residents in the tissue recognize the bacteria they start to produce proinflammatory cytokines that will diffuse through the tissue reaching the blood vessel. Once proinflammatory cytokines interact with the endothelial cells an increase in the endothelium permeability occurs allowing neutrophils and monocytes to migrate to the tissue.

```

float chemotaxis (float* * n, float **ch, int x, int y, float * * w)
{
    flux_left = 0;
    flux_right = 0;
    if (x > 0)
    {
        if ((ch[y][x] - ch[y][x - 1]) > 0)
        {
            flux_left = - (ch[y][x] - ch[y][x - 1]) * n[y][x - 1] * g(w[y][x - 1]) * f(w[y][x - 1]) / deltaX;
        }
        else
        {
            flux_left = - (ch[y][x] - ch[y][x - 1]) * n[y][x] * g(w[y][x]) * f(w[y][x]) / deltaX;
        }
    }
    if (x < (size - 1))
    {
        if ((ch[y][x + 1] - ch[y][x]) > 0)
        {
            flux_right = (ch[y][x + 1] - ch[y][x]) * n[y][x] * g(w[y][x]) * f(w[y][x]) / deltaX;
        }
        else
        {
            flux_right = (ch[y][x + 1] - ch[y][x]) * n[y][x + 1] * g(w[y][x + 1]) * f(w[y][x + 1]) / deltaX;
        }
    }
    resX = (flux_left + flux_right) / deltaX;
    flux_up = 0;
    flux_down = 0;
    if (y > 0)
    {
        if ((ch[y][x] - ch[y - 1][x]) > 0)
        {
            flux_up = - (ch[y][x] - ch[y - 1][x]) * n[y - 1][x] * g(w[y - 1][x]) * f(w[y - 1][x]) / deltaY;
        }
        else
        {
            flux_up = - (ch[y][x] - ch[y - 1][x]) * n[y][x] * g(w[y][x]) * f(w[y][x]) / deltaY;
        }
    }
    if (y < (size - 1))
    {
        if ((ch[y + 1][x] - ch[y][x]) > 0)
        {
            flux_down = (ch[y + 1][x] - ch[y][x]) * n[y][x] * g(w[y][x]) * f(w[y][x]) / deltaY;
        }
        else
        {
            flux_down = (ch[y + 1][x] - ch[y][x]) * n[y + 1][x] * g(w[y + 1][x]) * f(w[y + 1][x]) / deltaY;
        }
    }
    resY = (flux_up + flux_down) / deltaY;
    return (resX + resY);
}

```

ALGORITHM 1

The bacteria starts to die a lot due to the presence of huge numbers of neutrophils. However, the immune response can not completely eliminate bacteria due to the formation of the microabscess pattern. In the microabscess, there are bacteria and a huge concentration of dead cells around it (Figures

4, 5, and 6). In this context, the cleaning process realized by macrophages is very important to allow neutrophils to reach bacteria and eliminate them. Macrophages are responsible for phagocyte dead cells that accumulated in the microabscess. The pattern of microabscess could have lasted

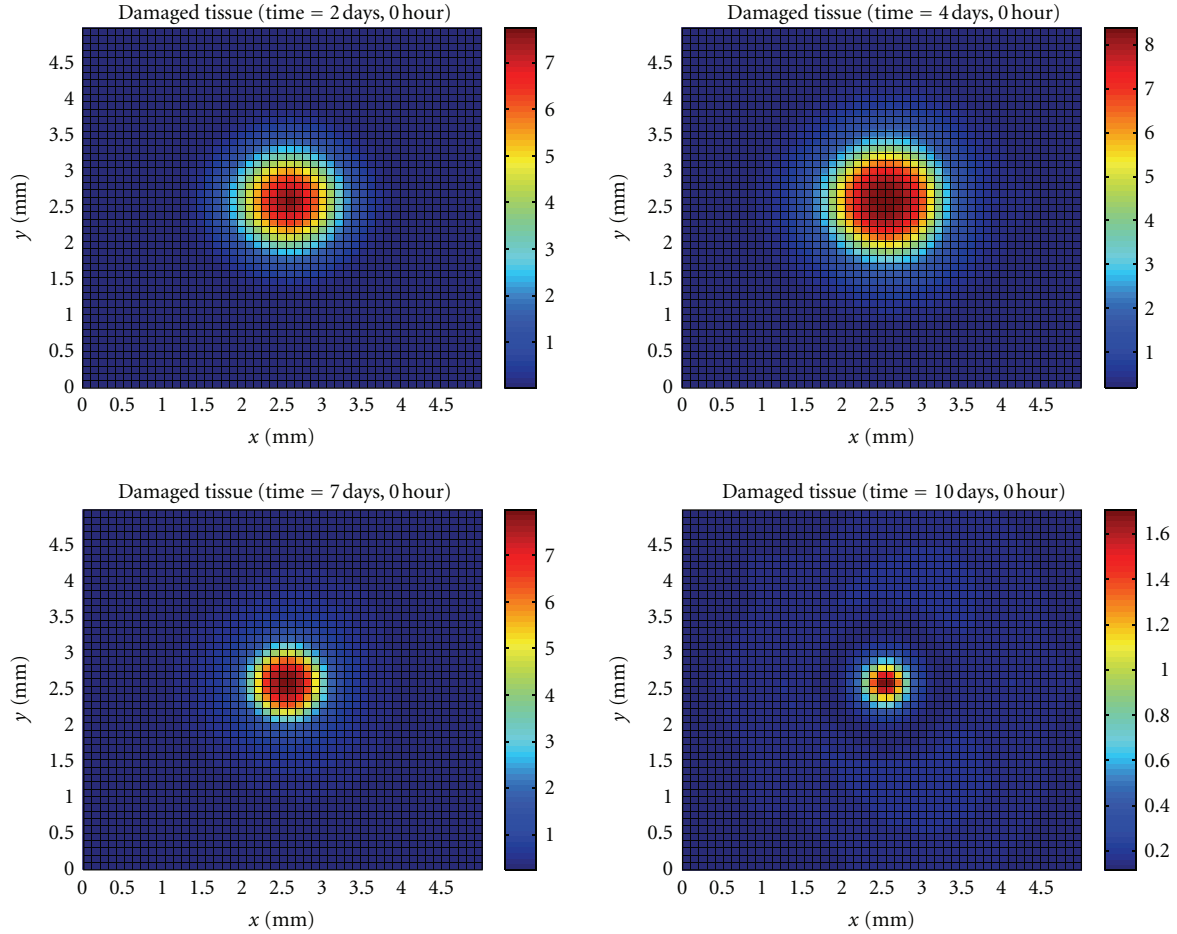


FIGURE 6: Temporal evolution and spatial distribution of damaged tissue cells.

longer if we had considered the formation of fibrous tissue around the microabscess.

11. Neutrophil

Neutrophils are initially attracted to the tissue by proinflammatory cytokines produced by activated resident macrophages (Figure 2). Once a neutrophil encounters bacteria, it phagocytizes bacteria and starts to produce proinflammatory cytokines that will attract more neutrophils and macrophages. The cytokine gradient will guide the movement of neutrophils and macrophages in the direction of the highest bacteria concentration.

After the microabscess formation, the immune system cells lose contact with a high number of bacteria. As these cells tend to move following the cytokine gradient, we can observe an accumulation of them around the microabscess.

After a significant number of macrophages phagocyte dead cells, the neutrophils can encounter the bacteria and phagocyte them from the border to the center of the microabscess area. As a consequence, a reduction in the microabscess area is observed (Figure 1), which indicates that the immune response is succeeding in controlling the infection.

12. Cytokine

The cytokines in Figure 3 are produced primarily by resident macrophages that are the first to recognize the bacteria presence. The cytokines will increase the endothelium permeability allowing neutrophils to migrate to the tissue. The arrived neutrophils will produce even more cytokines that will guide the movement of neutrophils and macrophage cells in the direction of high concentrations of bacteria.

During the formation of the microabscess and after it, the production of cytokines is higher in the regions where neutrophils and macrophages have contact with the bacteria that is surrounding the microabscess.

13. Apoptotic Neutrophils

In Figure 4, it can be observed that initially the neutrophils that came from the blood vessel closer to the site of infection died in large number than the neutrophils that came from other sites. Then, after microabscess formation, a lot of neutrophils start to die around the entire microabscess. This phenomenon continues until the microabscess disappears.

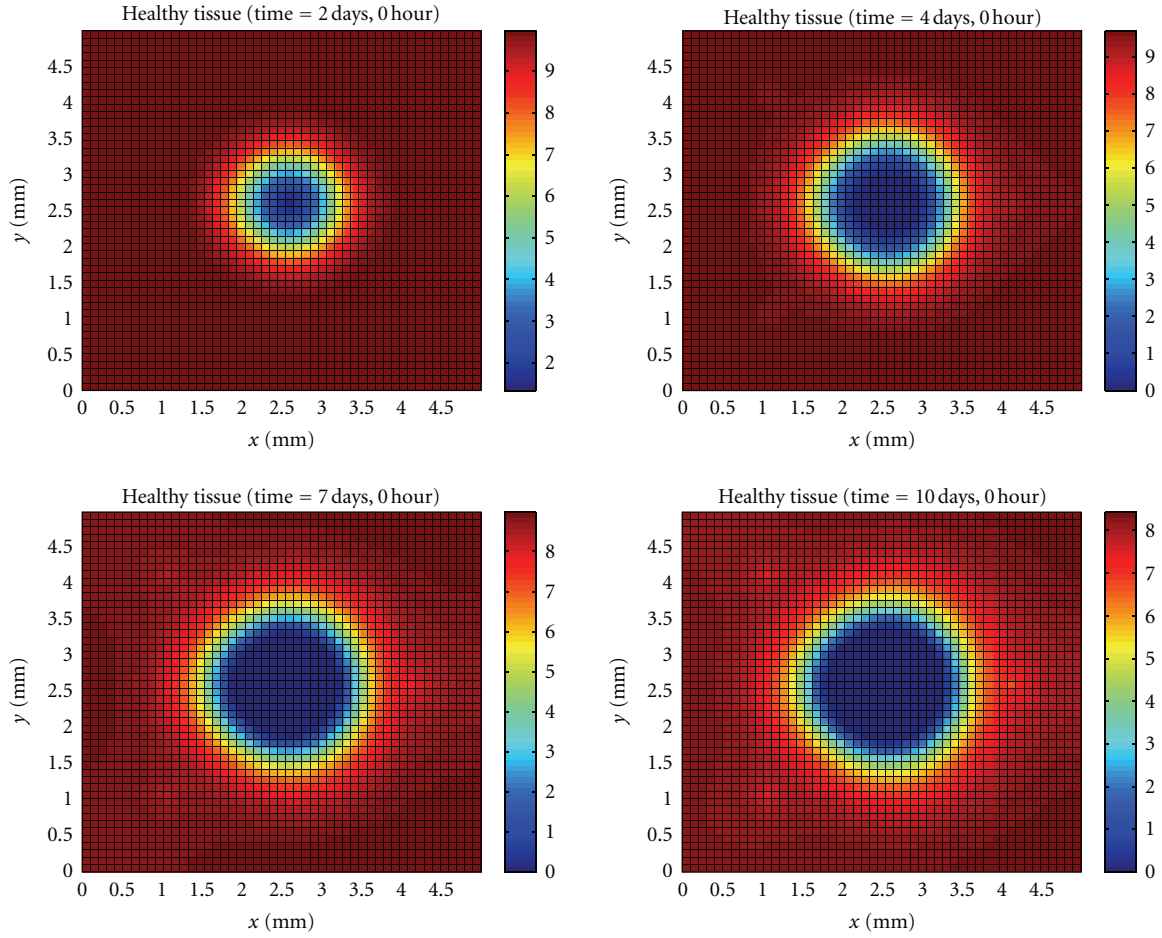


FIGURE 7: Temporal evolution and spatial distribution of healthy tissue cells.

14. Dead Bacteria

Figure 5 shows that initially more bacteria died near blood vessels. After the formation of the microabscess, the bacteria starts to die around the entire microabscess since this is the area where the immune response is acting.

15. Tissue Cells

In Figure 6, it can be observed that a lot of tissue damage by bacteria during the period the immune system took to mount an effective immune response. The number of dead tissue cells then reduces, because of the phagocytosis realized by macrophages.

Figure 7 shows the evolution of the healthy tissue area destroyed by the bacteria.

16. Microabscess Area

Figure 8 shows the microabscess area using a set of level curves. We defined the microabscess as an area where the concentration of bacteria plus concentration of dead bacteria plus the concentrations of damaged tissue and apoptotic neutrophil is higher. These results show that our model was

capable to reproduce the formation of the microabscess in agreement with the observed characteristics of a microabscess [7, 14, 49–54].

17. Conclusions and Future Works

In this work, we presented a computational model for the dynamics of representative types of cells and molecules of the HIS during an immune response to a bacteria. Despite the simplifications and limitations of the model, our results showed that we were able to reproduce an initial microabscess formation. The spatial results show a collection of dead tissue cells, dead bacteria, and apoptotic neutrophil in the microabscess region. This distinct pattern of formation can only be reproduced by spatiotemporal models, such as PDEs models.

As future work, we plan to perform a detailed sensitivity analysis of our microabscess formation model. A previous work [55] has given us some hints about the most sensitivity parameter of the model. We also plan to validate our model against experimental data.

We also plan to modify many aspects of the model to make it more real. For example, we plan to consider a more adequate model to represent the structure of the tissue

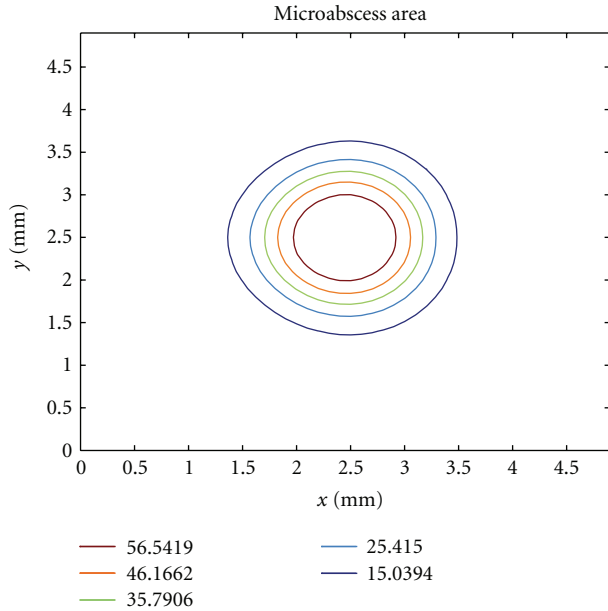


FIGURE 8: Level curves highlighting the microabscess area at day 5 of the immune response.

and its constituents. The tissue can be better characterized as a multiphasic porous medium subjected to stress and deformation variations mainly during the inflammatory process. This porous medium would comprise fluids, extracellular matrix, cells, and molecules. We also plan to model the mechanical behaviour of each of these phases and the mechanical interactions between them.

We have interest in developing models for processes such as vasodilation, coagulation, and others and analyse its effects on the mechanical behaviour of immune system cells and the consequences for the immune response.

With the aim to investigate better the formation of the microabscess, we plan to add another features that contribute to this formation such as the effects of extracellular pH on immune response [56]. Acidic pH predominates at inflammatory *loci* and other sites of immune activity. Investigations on neutrophils demonstrate mainly inhibition of chemotaxis, respiratory activity, and bactericidal capacity at reduced pH. Besides diminished extracellular pH may play a role in suppressing cytokine production and cytotoxic activities by pulmonary macrophages [56].

Besides we plan to add to the model the process of fibrous tissue formation around the microabscess. We plan to investigate what factors determine if the fibrous tissue will be produced or not. The production of fibrous tissue as well as the coagulation process are ways of the immune system to prevent the bacteria to spread throughout the body doing damage with possible serious consequences, for example, SIRS/MOF. In particular, we are interested in modeling the participation of macrophages, fibroblasts, tissue cells, endothelial cells, and many mediators in the process of fibrous tissue formation. An important step in this process is the production of collagen by fibroblasts induced by the cytokine TGF- β produced by macrophages

[57, 58]. The macrophages has many roles in the processes of wound healing and tissue repair. For example, during the coagulation process, macrophages and endothelial cells are responsible for the production of diverse growth factors and chemotactic substances that attracts and stimulates the proliferation of tissue cells initiating tissue repair [59].

Acknowledgments

The authors would like to thank FAPEMIG, CNPq, CAPES, and UFJF for supporting this study.

References

- [1] A. B. Pigozzo, G. C. Macedo, R. W. Dos Santos, and M. Lobosco, "Implementation of a computational model of the innate immune system," in *10th International Conference on Artificial Immune Systems (ICARIS '11)*, vol. 6825, pp. 95–107, July 2011.
- [2] A. B. Pigozzo, G. C. Macedo, R. W. dos Santos, and M. Lobosco, "On the computational modelling of the innate immune system," *BMC Bioinformatics*. In press.
- [3] E. J. Kerschen, J. A. Fernandez, B. C. Cooley et al., "Endotoxemia and sepsis mortality reduction by non-anticoagulant-activated protein C," *Journal of Experimental Medicine*, vol. 204, no. 10, pp. 2439–2448, 2007.
- [4] V. K. Klaitman and Y. Almog, "Corticosteroids in sepsis: a new concept for an old drug," *Israel Medical Association Journal*, vol. 5, no. 1, pp. 51–55, 2003.
- [5] Y. Vodovotz, G. Constantine, J. Rubin, M. Csete, E. O. Voit, and G. An, "Mechanistic simulations of inflammation: current state and future prospects," *Mathematical Biosciences*, vol. 217, no. 1, pp. 1–10, 2009.
- [6] X. Dong, P. T. Foteinou, S. E. Calvano, S. F. Lowry, and I. P. Androulakis, "Agent-based modeling of endotoxin-induced acute inflammatory response in human blood leukocytes," *PLoS ONE*, vol. 5, no. 2, Article ID e9249, 2010.
- [7] K. B. Seydel, T. Zhang, and S. L. Stanley, "Neutrophils play a critical role in early resistance to amebic liver abscesses in severe combined immunodeficient mice," *Infection and Immunity*, vol. 65, no. 9, pp. 3951–3953, 1997.
- [8] M. C. Rigother, H. Khun, P. Tavares, A. Cardona, M. Huerre, and N. Guillén, "Fate of *Entamoeba histolytica* during establishment of amoebic liver abscess analyzed by quantitative radioimaging and histology," *Infection and Immunity*, vol. 70, no. 6, pp. 3208–3215, 2002.
- [9] J. C. Lin, F. Y. Chang, C. P. Fung et al., "Do neutrophils play a role in establishing liver abscesses and distant metastases caused by *Klebsiella pneumoniae*?" *PLoS ONE*, vol. 5, no. 11, Article ID e15005, 2010.
- [10] Y. Ebe, G. Hasegawa, H. Takatsuka et al., "The role of Kupffer cells and regulation of neutrophil migration into the liver by macrophage inflammatory protein-2 in primary listeriosis in mice," *Pathology International*, vol. 49, no. 6, pp. 519–532, 1999.
- [11] M. Schön, D. Denzer, R. C. Kubitz, T. Ruzicka, and M. P. Schön, "Critical role of neutrophils for the generation of psoriasisiform skin lesions in flaky skin mice," *Journal of Investigative Dermatology*, vol. 114, no. 5, pp. 976–983, 2000.
- [12] A. Wetzel, T. Wetzig, U. F. Haustein et al., "Increased neutrophil adherence in psoriasis: role of the human endothelial

- cell receptor Thy-1 (CD90)," *Journal of Investigative Dermatology*, vol. 126, no. 2, pp. 441–452, 2006.
- [13] W. Grayson, "The HIV-positive skin biopsy," *Journal of Clinical Pathology*, vol. 61, no. 7, pp. 802–817, 2008.
 - [14] M. I. Cybulsky, I. J. Cybulsky, and H. Z. Movat, "Neutropenic responses to intradermal injections of *Escherichia coli*. effects on the kinetics of polymorphonuclear leukocyte emigration," *American Journal of Pathology*, vol. 124, no. 1, pp. 1–9, 1986.
 - [15] J. Bhavsar, D. Gordon, and M. Shea, "Listeria myocarditis with an atypical intracavitary vegetation/thrombus," *Heart*, vol. 96, no. 20, p. 1637, 2010.
 - [16] K. Oka, K. Oohira, Y. Yatabe et al., "Fulminant myocarditis demonstrating uncommon morphology—a report of two autopsy cases," *Virchows Archiv*, vol. 446, no. 3, pp. 259–264, 2005.
 - [17] M. D. Reid, O. Basturk, D. Thirabanjasak et al., "Tumor-infiltrating neutrophils in pancreatic neoplasia," *Modern Pathology*, vol. 24, no. 12, pp. 1612–1619, 2011.
 - [18] G. An, "Agent-based computer simulation and sirs: building a bridge between basic science and clinical trials," *Shock*, vol. 16, no. 4, pp. 266–273, 2001.
 - [19] G. An, "In silico experiments of existing and hypothetical cytokine-directed clinical trials using agent-based modeling," *Critical Care Medicine*, vol. 32, no. 10, pp. 2050–2060, 2004.
 - [20] C. J. Fisher, J. M. Agosti, S. M. Opal et al., "Treatment of septic shock with the tumor necrosis factor receptor:Fc fusion protein," *The New England Journal of Medicine*, vol. 334, no. 26, pp. 1697–1702, 1996.
 - [21] G. Clermont, J. Bartels, R. Kumar, G. Constantine, Y. Vodovotz, and C. Chow, "In silico design of clinical trials: a method coming of age," *Critical Care Medicine*, vol. 32, no. 10, pp. 2061–2070, 2004.
 - [22] W. Wakeland, L. Macovsky, and G. An, "A hybrid simulation model for studying acute inflammatory response," in *Proceedings of the Spring Simulation Multiconference (SpringSim '07)*, vol. 2, pp. 39–46, Society for Computer Simulation International, San Diego, Calif, USA, 2007.
 - [23] NetLogo, <http://ccl.northwestern.edu/netlogo/>.
 - [24] K. J. Painter and J. A. Sherratt, "Modelling the movement of interacting cell populations," *Journal of Theoretical Biology*, vol. 225, no. 3, pp. 327–339, 2003.
 - [25] K. J. Painter, "Continuous models for cell migration in tissues and applications to cell sorting via differential chemotaxis," *Bulletin of Mathematical Biology*, vol. 71, no. 5, pp. 1117–1147, 2009.
 - [26] S. Goutelle, M. Maurin, F. Rougier et al., "The Hill equation: a review of its capabilities in pharmacological modelling," *Fundamental and Clinical Pharmacology*, vol. 22, no. 6, pp. 633–648, 2008.
 - [27] K. J. Painter and T. Hillen, "Volume-filling and quorum-sensing in models for chemosensitive movement," *Canadian Applied Mathematics Quarterly*, vol. 10, no. 4, pp. 501–543, 2002.
 - [28] H. M. Byrne and M. R. Owen, "A new interpretation of the Keller-Segel model based on multiphase modelling," *Journal of Mathematical Biology*, vol. 49, no. 6, pp. 604–626, 2004.
 - [29] Z. A. Wang, "On chemotaxis models with cell population interactions," *Mathematical Modelling of Natural Phenomena*, vol. 5, no. 3, pp. 173–190, 2010.
 - [30] J. G. Wagner, "Kinetics of pharmacologic response I. Proposed relationships between response and drug concentration in the intact animal and man," *Journal of Theoretical Biology*, vol. 20, no. 2, pp. 173–201, 1968.
 - [31] R. J. LeVeque, "Finite Difference Methods for Ordinary and Partial Differential Equations Steady State and Time Dependent Problems," *Society for Industrial and Applied Mathematics*. In press.
 - [32] A. Harten, "High resolution schemes for hyperbolic conservation laws," *Journal of Computational Physics*, vol. 135, no. 2, pp. 260–278, 1997.
 - [33] B. P. Leonard, "Simple high-accuracy resolution program for convective modelling of discontinuities," *International Journal for Numerical Methods in Fluids*, vol. 8, no. 10, pp. 1291–1318, 1988.
 - [34] C. W. Shu and S. Osher, "Efficient implementation of essentially non-oscillatory shock-capturing schemes, II," *Journal of Computational Physics*, vol. 83, no. 1, pp. 32–78, 1989.
 - [35] G. A. Sod, "A survey of several finite difference methods for systems of nonlinear hyperbolic conservation laws," *Journal of Computational Physics*, vol. 27, no. 1, pp. 1–31, 1978.
 - [36] A. Marrocco, "Numerical simulation of chemotactic bacteria aggregation via mixed finite elements," *Mathematical Modelling and Numerical Analysis*, vol. 37, no. 4, pp. 617–630, 2003.
 - [37] F. Filbet, "A finite volume scheme for the Patlak-Keller-Segel chemotaxis model," *Numerische Mathematik*, vol. 104, no. 4, pp. 457–488, 2006.
 - [38] M. M. Hafez and J. J. Chattot, *Innovative Methods For Numerical Solution of Partial Differential Equations*, World Scientific Publishing Company, 2002.
 - [39] Y. Li, A. Karlin, J. D. Loike, and S. C. Silverstein, "A critical concentration of neutrophils is required for effective bacterial killing in suspension," *Proceedings of the National Academy of Sciences of the United States of America*, vol. 99, no. 12, pp. 8289–8294, 2002.
 - [40] R. De Waal Malefyt, J. Abrams, B. Bennett, C. G. Figdor, and J. E. De Vries, "Interleukin 10(IL-10) inhibits cytokine synthesis by human monocytes: an autoregulatory role of IL-10 produced by monocytes," *Journal of Experimental Medicine*, vol. 174, no. 5, pp. 1209–1220, 1991.
 - [41] I. P. Oswald, T. A. Wynn, A. Sher, and S. L. James, "Interleukin 10 inhibits macrophage microbicidal activity by blocking the endogenous production of tumor necrosis factor α required as a costimulatory factor for interferon γ -induced activation," *Proceedings of the National Academy of Sciences of the United States of America*, vol. 89, no. 18, pp. 8676–8680, 1992.
 - [42] G. D. Martich, R. L. Danner, M. Ceska, and A. F. Suffredini, "Detection of interleukin 8 and tumor necrosis factor in normal humans after intravenous endotoxin: the effect of antiinflammatory agents," *Journal of Experimental Medicine*, vol. 173, no. 4, pp. 1021–1024, 1991.
 - [43] M. H. Beers, R. S. Porter, and T. V. Jones, *The Merck Manual*, Merck & Co., 18th edition, 2006.
 - [44] B. Su, W. Zhou, K. S. Dorman, and D. E. Jones, "Mathematical modelling of immune response in tissues," *Computational and Mathematical Methods in Medicine*, vol. 10, pp. 1748–6718, 2009.
 - [45] T. H. Price, H. D. Ochs, R. Gershoni-Baruch, J. M. Harlan, and A. Etzioni, "In vivo neutrophil and lymphocyte function studies in a patient with leukocyte adhesion deficiency type II," *Blood*, vol. 84, no. 5, pp. 1635–1639, 1994.
 - [46] R. Kumar, G. Clermont, Y. Vodovotz, and C. C. Chow, "The dynamics of acute inflammation," *Journal of Theoretical Biology*, vol. 230, no. 2, pp. 145–155, 2004.
 - [47] A. Reynolds, J. Rubin, G. Clermont, J. Day, Y. Vodovotz, and G. Bard Ermentrout, "A reduced mathematical model of the acute inflammatory response: I. Derivation of model and

- analysis of anti-inflammation,” *Journal of Theoretical Biology*, vol. 242, no. 1, pp. 220–236, 2006.
- [48] A. Andoh, H. Takaya, T. Saotome et al., “Cytokine regulation of chemokine (IL-8, MCP-1, and RANTES) gene expression in human pancreatic periacinar myofibroblasts,” *Gastroenterology*, vol. 119, no. 1, pp. 211–219, 2000.
 - [49] C. W. Hanke, H. R. Higley, D. M. Jolivet, N. A. Swanson, and S. J. Stegman, “Abscess formation and local necrosis after treatment with Zyderm or Zyplast Collagen Implant,” *Journal of the American Academy of Dermatology*, vol. 25, no. 2, part 1, pp. 319–326, 1991.
 - [50] G. A. MacDonald, J. K. Greenson, E. A. DelBuono et al., “Mini-microabscess syndrome in liver transplant recipients,” *Hepatology*, vol. 26, no. 1, pp. 192–197, 1997.
 - [51] L. W. Lamps, C. W. Pinson, D. S. Raiford, Y. Shyr, M. A. Scott, and M. K. Washington, “The significance of microabscesses in liver transplant biopsies: a clinicopathological study,” *Hepatology*, vol. 28, no. 6, pp. 1532–1537, 1998.
 - [52] A. D. Gable, D. K. Marsee, D. A. Milner, and S. R. Granter, “Suppurative inflammation with microabscess and pseudocyst formation is a characteristic histologic manifestation of cutaneous infections with rapid-growing *Mycobacterium* species,” *American Journal of Clinical Pathology*, vol. 130, no. 4, pp. 514–517, 2008.
 - [53] J. C. Lin, F. Y. Chang, C. P. Fung et al., “Do neutrophils play a role in establishing liver abscesses and distant metastases caused by *Klebsiella pneumoniae*?” *PLoS ONE*, vol. 5, no. 11, Article ID e15005, 2010.
 - [54] H. S. Alsaif, S. K. Venkatesh, D. S. G. Chan, and S. Archuleta, “CT appearance of pyogenic liver abscesses caused by *Klebsiella pneumoniae*,” *Radiology*, vol. 260, no. 1, pp. 129–138, 2011.
 - [55] P. Rocha, A. Pigozzo, B. Quintela, G. Macedo, R. Santos, and M. Lobosco, “Modelling the innate immune system,” in *Bio-Inspired Computational Algorithms and their Applications*, InTech, 2012.
 - [56] A. Lardner, “The effects of extracellular pH on immune function,” *Journal of Leukocyte Biology*, vol. 69, no. 4, pp. 522–530, 2001.
 - [57] E. P. Amento, N. Ehsani, H. Palmer, and P. Libby, “Cytokines and growth factors positively and negatively regulate interstitial collagen gene expression in human vascular smooth muscle cells,” *Arteriosclerosis and Thrombosis*, vol. 11, no. 5, pp. 1223–1230, 1991.
 - [58] M. R. Duncan, K. S. Frazier, S. Abramson et al., “Connective tissue growth factor mediates transforming growth factor β -induced collagen synthesis: downregulation by cAMP,” *The FASEB Journal*, vol. 13, no. 13, pp. 1774–1786, 1999.
 - [59] A. C. Newby and A. B. Zaltsman, “Fibrous cap formation or destruction—the critical importance of vascular smooth muscle cell proliferation, migration and matrix formation,” *Cardiovascular Research*, vol. 41, no. 2, pp. 345–360, 1999.

Research Article

Time-Course Analysis of Main Markers of Primary Infection in Cats with the Feline Immunodeficiency Virus

**B. Ribba,¹ H. El Garch,² S. Brunet,² E. Grenier,¹
F. Castiglione,³ H. Poulet,² and P. Vanhems^{4,5,6,7}**

¹INRIA, Project-team NUMED, Ecole Normale Supérieure de Lyon, 46 allée d'Italie, 69007 Lyon Cedex 07, France

²Discovery Research, Meril SAS, 69007 Lyon, France

³Institute for Computing Applications "M. Picone", National Research Council of Italy (CNR), Rome, Italy

⁴Service d'Hygiène, Epidémiologie et Prévention, Hospices Civils de Lyon, 69008 Lyon, France

⁵Université de Lyon, 69000 Lyon, Lyon, Université Lyon I, Villeurbanne, F-69100, France

⁶Université de Lyon I, 69000 Villeurbanne, France

⁷Equipe Epidémiologie et Santé Publique, Laboratoire de Biométrie et Biologie Evolutive, UMR 5558, CNRS,

8 Avenue Rockefeller, 69310 Lyon cedex, France

Correspondence should be addressed to B. Ribba, benjamin.ribba@inria.fr

Received 14 June 2012; Accepted 29 July 2012

Academic Editor: Francesco Pappalardo

Copyright © 2012 B. Ribba et al. This is an open access article distributed under the Creative Commons Attribution License, which permits unrestricted use, distribution, and reproduction in any medium, provided the original work is properly cited.

Studies of the response of the immune system to feline immunodeficiency virus (FIV) during primary infection have shown that a subpopulation of CD8⁺ T-cells with an activated phenotype and reduced expression of the CD8 β chain (denoted CD8 β^{low} T cells) expands to reach up to 80% of the total CD8⁺ T cell count. The expansion of this subpopulation is considered to be a signature of FIV and an indicator of immune system alteration. We use a simple mathematical formalism to study the relationships over time between the dose of infection, the size of the CD8 β^{low} population, and the circulating viral load in cats infected with FIV. Viremia profiles are described using a combination of two exponential laws, whereas the CD8 β^{low} percentage (out of the total CD8⁺ population) is represented by a Gompertz law including an expansion phase and a saturation phase. Model parameters are estimated with a population approach using data from 102 experimentally infected cats. We examine the dose of infection as a potential covariate of parameters. We find that the rates of increase of viral load and of CD8 β^{low} percentage are both correlated with the dose of infection. Cats that develop strong acute viremia also show the largest degree of CD8 β^{low} expansion. The two simple models are robust tools for analysing the time course of CD8 β^{low} percentage and circulating viral load in FIV-infected cats and may be useful for generating new insights on the disease and on the design of therapeutic strategies, potentially applicable to HIV infection.

1. Introduction

Cats infected with the feline immunodeficiency virus (FIV) develop an acquired immunodeficiency syndrome (AIDS) much like humans infected with HIV [1]. The infection causes an acute viremia, which decreases after several weeks, and the development of a partial immunity [2]. The acute stage is followed by a chronic asymptomatic phase, often persisting for years, during which the immune system is progressively impaired. As in the case of HIV infection, the more common signs of the asymptomatic phase are the

depletion of CD4⁺ peripheral T cells and the reduction of the CD4/CD8 ratio [3]. At the end of the asymptomatic stage of the disease, infected cats develop chronic opportunistic infections and eventually die [4].

The immune response to FIV during acute infection is well documented in the literature (see in particular [5–7]). In addition to anti-FIV neutralizing antibodies and cytotoxic and noncytotoxic CD8⁺ T cells, the primary (acute) stage of infection is known to be characterized by the appearance and expansion of a CD8⁺ T-cell subpopulation with an activated phenotype showing reduced expression of the

CD8 β chain and the complete disappearance of the L-selectin CD62L surface molecule [8]. These CD8 β^{low} CD62L $^-$ T cells, hereafter referred to as CD8 β^{low} cells, persist throughout the course of infection. The persistence of this activated T-cell population, which has been shown to possess anti-FIV activity, suggests a profound homeostatic disorder, as in healthy animals activated CD8 cells are generally present only during peak immune responses.

The observed expansion of the CD8 β^{low} cell subpopulation—which can reach, during the acute stage, up to 80% of the total population of CD8 $^+$ T cells—may be driven by CD8 β^{low} cells' sensitivity to apoptosis, a sensitivity that is enhanced by antigen recognition [2]. CD8 β^{low} cells might be chronically activated as a result of persistent virus replication and antigen recognition, die by apoptosis and get replenished quickly. Thus, it is believed that FIV can alter the immune homeostasis by inducing chronic activation of CD8 $^+$ T cells into CD8 β^{low} , driving their expansion, and, at the same time, inducing cytotoxicity against infected CD4 $^+$ T cells.

The expansion of the CD8 β^{low} subpopulation is considered to be an important marker of FIV infection and disease [2]. A characterization of the process of expansion, in addition to other markers of disease, is likely to increase researchers' understanding of FIV infection and AIDS pathogenesis, thus facilitating the design of new therapeutic strategies.

Mathematical models to describe longitudinal data from HIV-infected patients have been extensively developed [9]. To describe the dynamics of viremia and CD4 $^+$ T cells, numerous models have used systems of ordinary differential equations based on the prey-predator modelling framework [10–13]. In this type of model, viral particles infect healthy CD4 $^+$ T cells, which later die, liberating new replicated virus into the plasma. One of the most interesting aspects of this mechanistic approach is that each model parameter has a clear biological meaning, such as rate of infection of CD4 $^+$ T cells, the cell lifespan, or the virus replication rate. Such models have been shown to correctly predict circulating viral loads in HIV-infected patients undergoing antiviral therapies [11]. Some variations of this modelling approach have been discussed in the literature. For instance, the integration of cytotoxic CD8 $^+$ T cells has been shown to potentially describe with more accuracy the kinetics of viremia in HIV patients [14]. Models based on the prey-predator framework can provide interesting insights into the life cycle of the virus and its interaction with the host. However, these models tend to be complex, as they generally integrate a large number of parameters and variables such as viral load, CD4 $^+$ T cells of different status (e.g., uninfected, early-stage infected, late-stage infected), and different types of CD8 $^+$ T cells. Proper estimation of such parameters requires a large number of observations (ideally, observations for all variables should be available) for all individuals to be analyzed. Obviously, these are difficult conditions to meet in a clinical setting. Furthermore, it is known that the immune response can vary significantly across subjects, and it might therefore be too simplistic to assume parameters to be constant in a given population of patients. The need to integrate interindividual results adds an additional level

of complexity to the already complex mechanistic model. Finally, to our knowledge, such models have not yet been challenged with data from untreated primary infection (e.g., data from untreated HIV-infected patients or from FIV-infected cats), so the information they provide regarding the natural progression of disease may be limited.

In this study, we propose two phenomenological models that correctly reproduce the time-evolution of the percentage of CD8 β^{low} CD62L $^-$ T cells and of circulating viral load during the early primary infection phase in 102 cats infected with various doses of FIV.

2. Materials and Methods

2.1. Ethic Statement. All animal experiments were conducted in accordance with the European Community regulations, and all procedures were supervised and approved by the Merial Ethical Committee.

2.2. Animals. In this experiment, 102 cats (49 males and 53 females; mean age: 22.8 weeks, SD: 7.7, range: 13–36.5) were randomized into 23 groups of 4 to 7 cats each. Each group was assigned an FIV strain (Petaluma clade A, Glasgow-8 clade A, or EVA clade B) and inoculum size. Each cat was challenged with a single intramuscular injection of 1 mL of viral suspension of one of the three FIV strains examined. In preliminary *in vitro* experiments, the three strains were observed to be comparable in terms of viremia and impact on lymphocyte subpopulations. Virus dilutions ranged from 1/90,000 to 1/3, and the infection doses, expressed in log₁₀/mL of cell culture infectious dose 50% (CCID₅₀), ranged from 0.26 to 4.09 (median: 2.5, SD: 1.21).

2.3. Longitudinal Measurements. Viral load was measured using quantitative real-time polymerase chain reaction. For each cat, a measurement was taken at time 0, and, when possible, additional measurements were taken at the ends of weeks 1, 3, 4, 6, 9, 12, 15, 18, and 23. Values were expressed as log₁₀ of viral RNA copies per millilitre of plasma. For these measurements, the detection threshold, or the limit of quantification (LOQ), was 80 copies per mL, which corresponds to 1.9 on the log₁₀ scale. In total, 485 measurements were analyzed, but there was high variability in the number of measurements per cat (mean = 4.75 measurements/cat, min = 1, max = 7, SD = 1.2). The values themselves (all taken together) were also highly variable (median = 3.95 log₁₀ RNA copies/mL of plasma, min = 1.9 (LOQ), max = 6.91, SD = 1.37).

The number of CD8 β^{low} cells and the total number of CD8 $^+$ T cells were measured by flow cytometry as described in [2]. However, data on these lymphocytes were available for only 79 cats out of the total 102. The size of the CD8 β^{low} CD62L $^-$ subpopulation was expressed as the percentage of CD8 β^{low} CD62L $^-$ T cells in the entire CD8 $^+$ T-cell population. The analysis was carried out on 377 observations with an average of 4.8 observations per animal (min = 3, max = 6, SD = 0.8). The median observed value of

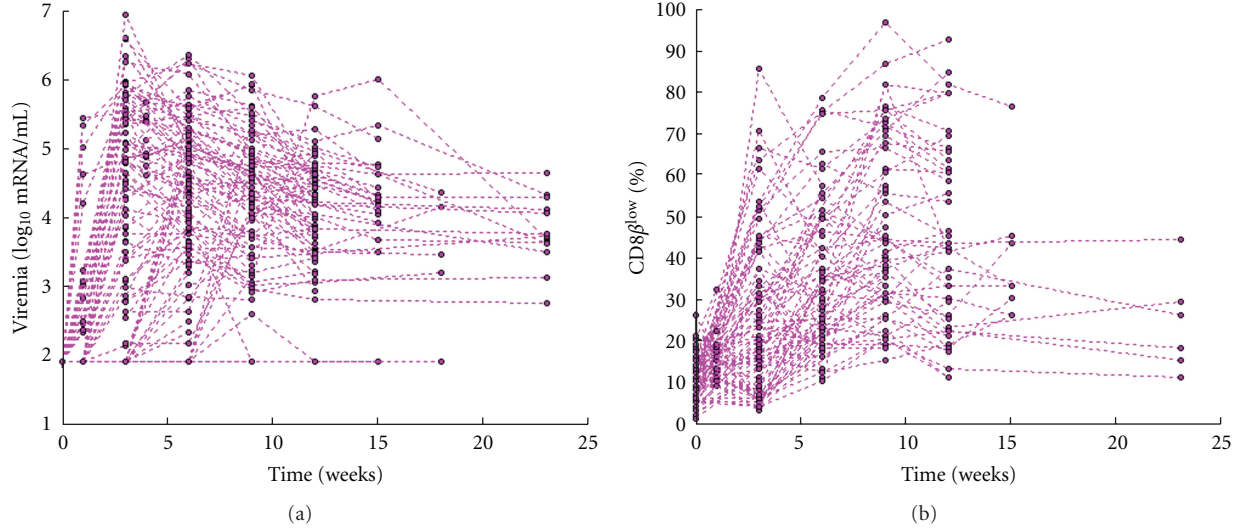


FIGURE 1: Time-evolution of circulating viral load, expressed as \log_{10} of viral RNA copies per mL plasma (a); $CD8\beta^{low}$ population size expressed as the percentage of the $CD8\beta^{low}CD62L^-$ T-cell subpopulation out of the total population of $CD8^+$ T cells (b). Time is expressed as weeks after infection. Viral load was measured in 102 cats, but $CD8\beta^{low}$ cell counts were measured in only 79 cats.

$CD8\beta^{low}$ percentage was 22% (min = 1%, max = 96%, SD = 20.5). Figure 1 shows the time-evolution of viral load in all 102 cats (Figure 1(a)) and $CD8\beta^{low}$ percentage in the 79 cats (Figure 1(b)) for which lymphocyte counts were available. The curves indicate high variability across cats in both viral load and $CD8\beta^{low}$ percentages.

2.4. Data Analysis. The high variability in the number of available data points per animal, as well as the variability across animals in the patterns of the data, required the use of mixed-effects regression techniques. Mixed-effects models take into account different forms of variability and, in particular, interindividual variability [15]. More precisely, they use the available information from all individuals of an analyzed population to retrieve both population-level and individual-level values for the dynamic parameters. As a consequence, they are particularly suited for the analysis of datasets with large numbers of individuals, even if data are sparse for some of the individuals.

In their general form, such models can be written as follows:

$$y_{ij} = f(x_{ij}, \phi_i) + g(x_{ij}, \phi_i)\varepsilon_{ij}, \quad 1 \leq i \leq N; \quad 1 \leq j \leq n_i, \quad (1)$$

where N is the number of animals, n_i the number of observations for individual i , x the regression variable (e.g., time), and y the observations. The term f represents deterministic equations; in our case, these are simple phenomenological laws. The residual error is $g(x_{ij}, \phi_i)\varepsilon_{ij}$, where $\varepsilon_{ij} \sim N(0, \sigma^2)$. In what follows we will consider constant error models, that is, $g(x_{ij}, \phi_i) = 1$.

Each individual parameter ϕ_i can be defined as follows:

$$\phi_i = h(\mu + \eta_i), \quad \eta_i \sim N(0, \Omega), \quad i = 1, \dots, N, \quad (2)$$

where η_i is a p -vector of random effects and h is some pre-defined transformation. Here, we assume that the individual parameters are log-normally distributed (i.e., $h(u) = e^u$). μ is a p -vector of fixed population parameters (i.e., $h(\mu)$ is the median value across individuals for each of the p parameters). Ω is the $p \times p$ variance-covariance matrix of the random effects. We assume potential correlations between the random effects, meaning that Ω is a full matrix.

The unknown set of parameters in the model is then

$$\theta = (\mu, \Omega, \sigma^2). \quad (3)$$

The likelihood function related to this problem can be written as follows:

$$L(\theta, y) = \prod_{i=1}^N L_i(\theta, y_i), \quad (4)$$

with

$$\begin{aligned} L_i(\theta, y_i) &= \int p(y_i, \eta_i, \theta) d\eta_i \\ &= C \int \sigma^{-n_i} |\Omega|^{-1/2} e^{-1/(2\sigma^2) \|y_i - f(x_i, \phi_i)\|^2 - (1/2) \eta_i' \Omega^{-1} \eta_i} d\eta_i. \end{aligned} \quad (5)$$

If f is nonlinear with respect to the random effects, the likelihood function cannot be easily computed and maximized. One intuitive means of addressing this problem is to analyze the data from each individual separately. This approach, however, requires a large number of observations per individual, and therefore it is clearly not feasible in our case. An alternative method is the SAEM algorithm (stochastic approximation of the EM algorithm [16]), which can be used to calculate the maximum likelihood, without any approximation of the likelihood function and to estimate

population (θ) and individual (ϕ_i) parameters. We used Monolix software (Lixoft) to estimate those parameters. The software analyzes all individual data simultaneously. In a first step, a likelihood function is minimized in order to estimate the mean values of the model parameters as well as their variability throughout the population. The resultant estimates are referred to as the population parameters. In a second step, information on the mean parameter values is used to estimate, on the basis of each individual dataset, the best model parameters for each individual. These are called individual parameters.

Mixed-effects models also have the advantage of being associated with a large panel of validation tools. The log-likelihood (LLH) value (actually $-2 \times \text{LLH}$) is generally used to select the best model from among multiple models. However, since a model with a greater number of parameters is more likely to produce a better fit because it has more degrees of freedom, a penalty term is generally added to the likelihood function to account for the number of parameters. Examples of criterion functions that include such penalty terms are the Akaike information criterion (AIC):

$$\text{AIC} = -2 \times \text{LLH} + 2 \times n, \quad (6)$$

where n is the number of free parameters to be estimated, and the Bayesian information criterion (BIC):

$$\text{BIC} = -2 \times \text{LLH} + \log(k) \times n, \quad (7)$$

where k is the sample size.

We tested different types of phenomenological models, and we selected the best ones on the basis of three criterion functions—namely, $-2 \times \text{LLH}$, AIC, and BIC values—goodness of fit, residual plots, and precision of parameter estimates as relative standard errors. We assessed simulation-based diagnostics through visual predictive check, that is, we graphically compared the observed data and the simulated data (using population parameters and both interindividual and residual variability). We calculated ε -shrinkage and η -shrinkage to evaluate the degree of shrinkage of individual predictions towards the observations [17]. High values of shrinkage ($>30\%$) are considered to impair diagnostics based on individual predictions and covariate analysis [17].

3. Results

3.1. Modelling Viremia. We first formulated a model to describe the observed pattern of acute increase in viral load followed by decay, as shown in Figure 1(a). The best model we identified was a sum of two exponentials, describing, respectively, the growth and decay parts of the curves:

$$V = \frac{A_0 k_{\text{in}}}{k_{\text{in}} - k_{\text{out}}} (e^{-k_{\text{out}} t} - e^{-k_{\text{in}} t}), \quad (8)$$

where V is the viral load, expressed as \log_{10} of the number of viral RNA copies per mL of plasma; k_{in} and k_{out} are the two parameters regulating, respectively, the increase and decay of viral load; A_0 is a scaling adimensional parameter. Figure 2(a) shows a schematic view and focuses on the effect

of changing the value of the parameter k_{in} . The higher the parameter value, the more rapid the increase in viral load. Interanimal variability in the model parameters (A_0 , k_{in} , k_{out}) was assumed to be log-normally distributed, and cat-specific estimates are given as follows, for example, for k_{in} :

$$k_{\text{in}_i} = k_{\text{in}} e^{\eta_i^{k_{\text{in}}}}, \quad (9)$$

where k_{in} is the typical value for the population (mean value) and $\eta_i^{k_{\text{in}}}$ is an inter-animal random effect that follows a normal distribution with mean 0 and variance $\omega_{k_{\text{in}}}^2$.

In a second step, the dose of infection and the virus strain were evaluated as continuous and, respectively, categorical covariates. We used a backward-stepwise method to test how inclusion of these covariates affected the three model parameters [18]. Virus strain had no significant effect on the values of any of the three parameters, whereas dose of infection, expressed in \log_{10}/mL of CCID50, affected the constant rate of increase of viral load. Dose of infection was successfully integrated into k_{in} , which can be written as follows:

$$k_{\text{in}} = k_{\text{in}} e^{\beta_{k_{\text{in}}} \times \text{DOSE}}. \quad (10)$$

With this covariate integration, the objective function ($-2 \times \text{LLH}$) was reduced by 58 points, the parameter $\beta_{k_{\text{in}}}$ was estimated with high precision ($P < 0.001$), and the variability on the k_{in} parameter decreased by 30%.

Consequently, the value of parameter k_{in} increases as the inoculum size increases, ranging from 0.074 weeks⁻¹ for the lowest dose to 3.55 weeks⁻¹ for the highest dose. This result indicates that the higher the dose of infection, the stronger the increase of viral load in the acute phase. The parameter k_{out} was estimated at 0.025 weeks⁻¹, and the scaling factor A_0 at 5.56. All parameters were estimated with low-standard errors. Table 1 presents the parameter estimates of the model as mean values, with standard deviation of random effects or inter-animal variability (IAV). Figure 3 shows model diagnostics with a visual predictive check, that is, the simulation of the population model with 95% of variability together with the data points (Figure 3(a)) and individual predictions plotted against the actual observations (Figure 3(b)). Correlation between predictions and observations is good ($r^2 = 0.81$, $P < 0.001$). In Figure 4, we show individual predictions with a 95% confidence interval around the predictions for six cats taken from the analyzed population and who were challenged with infection doses from 1.65 to 4.09 \log_{10}/mL . The model correctly predicts the time-evolution of viral load in the individual cats, and a relationship is demonstrated between the dose of infection and the rate of increase of viral load in plasma during the primary stage of infection. This correlation is shown in Figure 5(a), where the estimated values of parameter k_{in} for all 102 cats are plotted against the actual values of the infection dose ($r^2 = 0.73$, $P < 0.001$).

3.2. Modelling $\text{CD8}\beta^{\text{low}}\text{CD62L}^-$. In the study presented in [2], the percentage of $\text{CD8}\beta^{\text{low}}$ cells is shown to increase in the weeks following infection, eventually reaching a

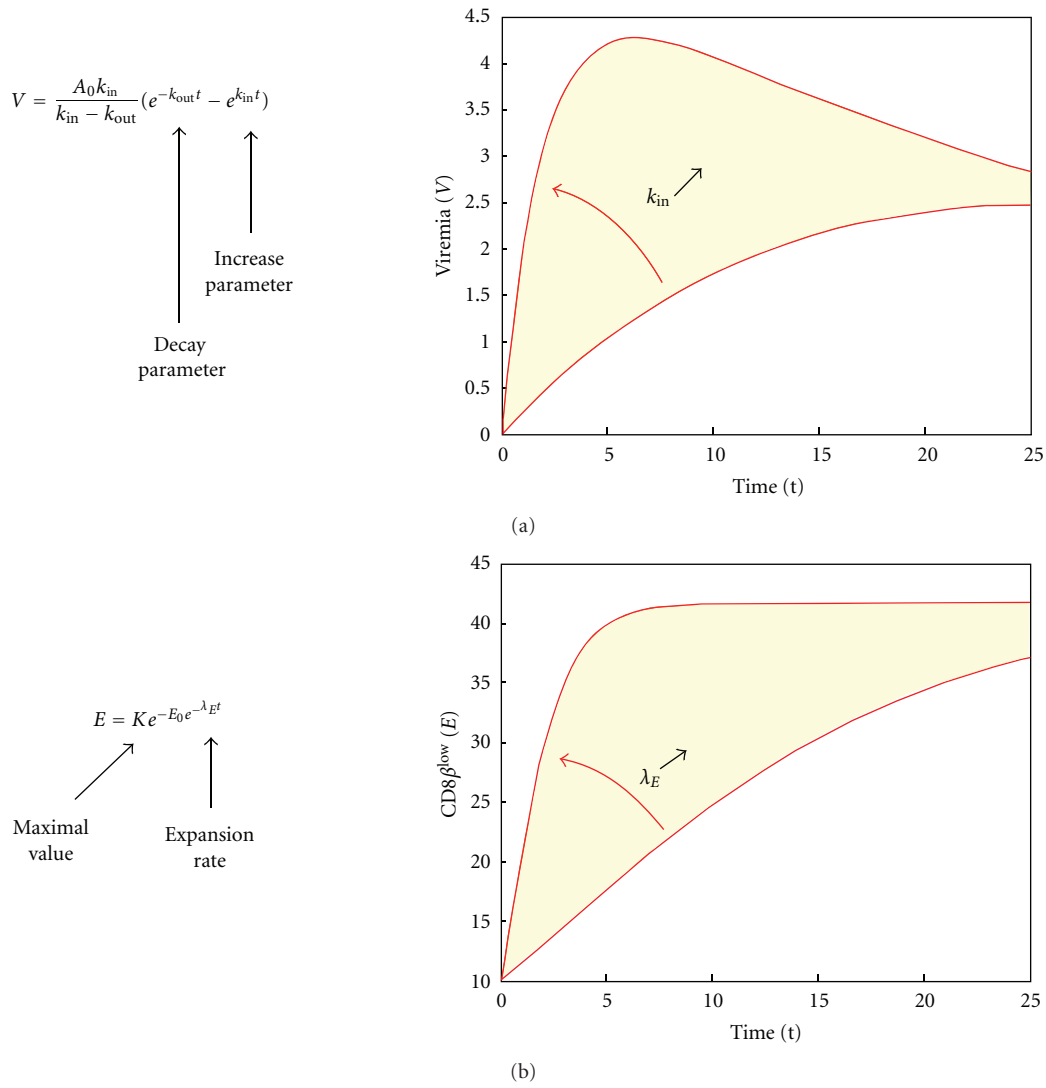


FIGURE 2: Schematic view and basic simulations of selected models for viremia (a) and $CD8\beta^{low}$ percentage (b). We highlight here the role of the parameters regulating the increase of viremia and $CD8\beta^{low}$, respectively.

TABLE 1

Parameters	Description	Mean value (SE)	IAV	η -shrinkage
Viral load				
k_{in}	Increase rate of viral load	0.06 week ⁻¹ (21%)	97%	21%
β_{kin}	Covariate (cell line) on parameter k_{in} (exponential formulation)	1.01 (12%)	—	—
k_{el}	Decay rate of viral load	0.02 week ⁻¹ (9%)	46%	66%
A_0	Scaling parameter	5.56 (2%)	35%	26%
a_V	Parameter of the error residual model (constant formulation)	0.56 (5%)	—	—
$CD8\beta^{low}$				
λ_E	Expansion rate of $CD8\beta^{low}$	0.07 week ⁻¹ (28%)	74%	35%
β_{λ_E}	Covariate (cell line) on parameter λ_E (exponential formulation)	0.77 (17%)	—	—
K	Maximal $CD8\beta^{low}$ percentage	39.4 (6%)	56%	23%
E_0	Scaling parameter	1.42 (6%)	54%	31%
a_E	Parameter of the error residual model (exponential formulation)	0.41 (5%)	—	—

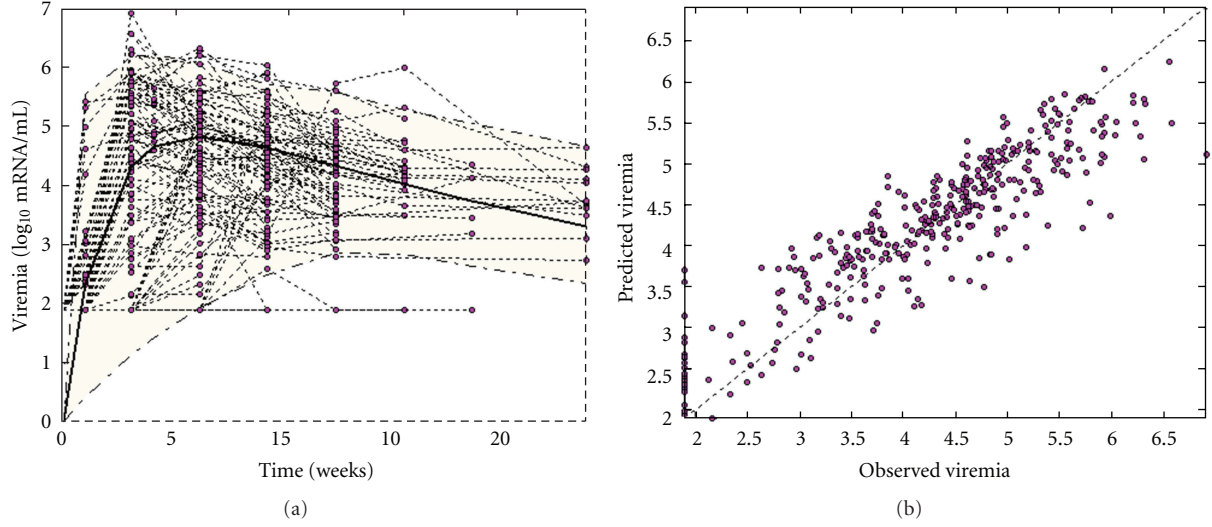


FIGURE 3: Viremia model diagnostics. (a): Simulation of the population model with 95% of variability together with the data points (visual predictive check). (b): Individual predictions versus the actual observations.

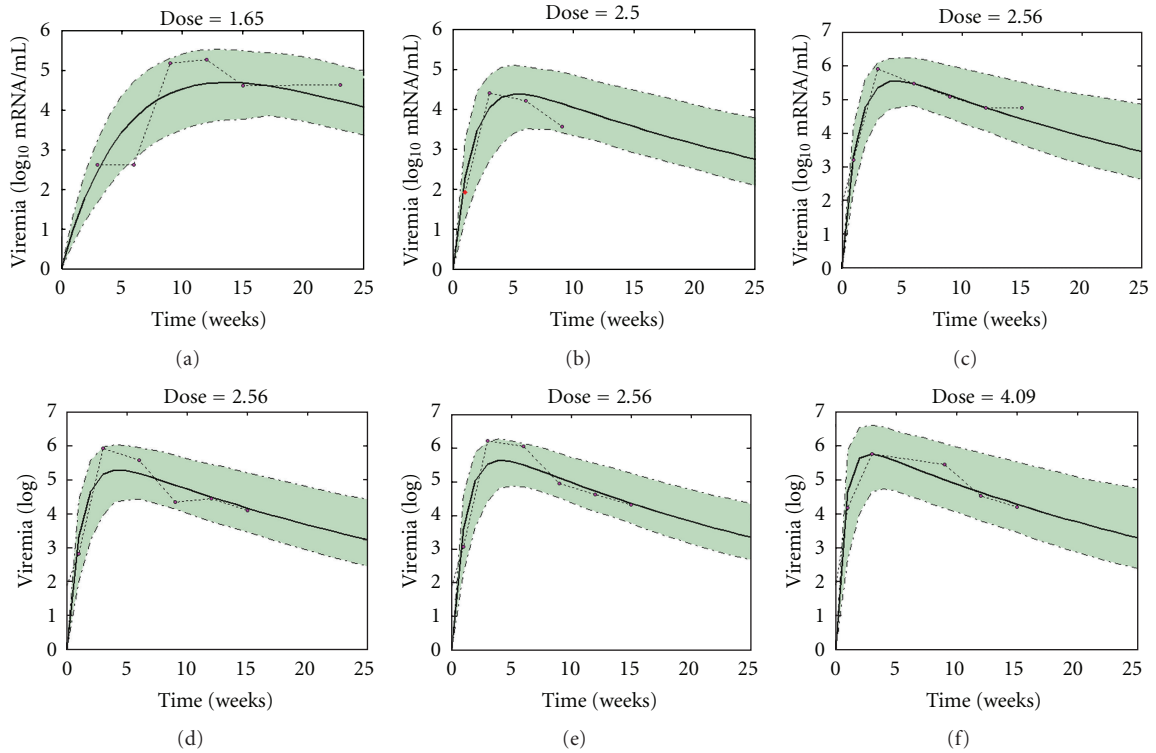


FIGURE 4: Goodness of individual predictions of viral load. A 95% confidence interval around the prediction for six cats taken from the analyzed population is shown. The corresponding infection doses, expressed as log₁₀/mL of cell culture infectious dose 50% (CCID50), are shown.

saturation level. We tested several laws, such as a sigmoid function, in an attempt to reproduce this pattern. The best model selected was the Gompertz equation. The model can be written as follows:

$$E = K e^{-E_0 e^{-\lambda_E t}}, \quad (11)$$

where E represents the percentage of $CD8^{\beta low}$ cells, and the parameter E_0 is involved in the expression of the percentage of $CD8^{\beta low}$ cells at time 0. More precisely, we set $E(t = 0) = K e^{-E_0}$. λ_E is a constant term determining the expansion rate and K is the maximal percentage of $CD8^{\beta low}$ cells. The larger the parameter λ_E , the sharper the expansion. Figure 2(b) shows a schematic view of the model and highlights the

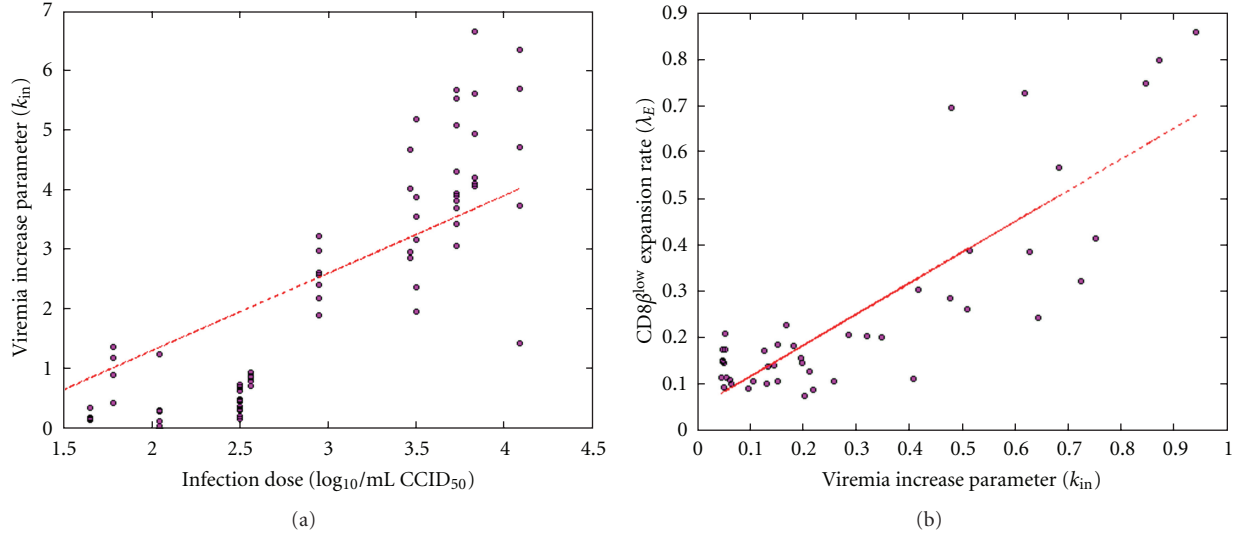


FIGURE 5: (a) Correlations found between the dose of infection, expressed in $\log_{10}/\text{mL CCID}_{50}$, and the increase rate of viral load. (b) Resulting correlation between the rate of increase of viral load and $\text{CD8}\beta^{\text{low}}$ expansion rate.

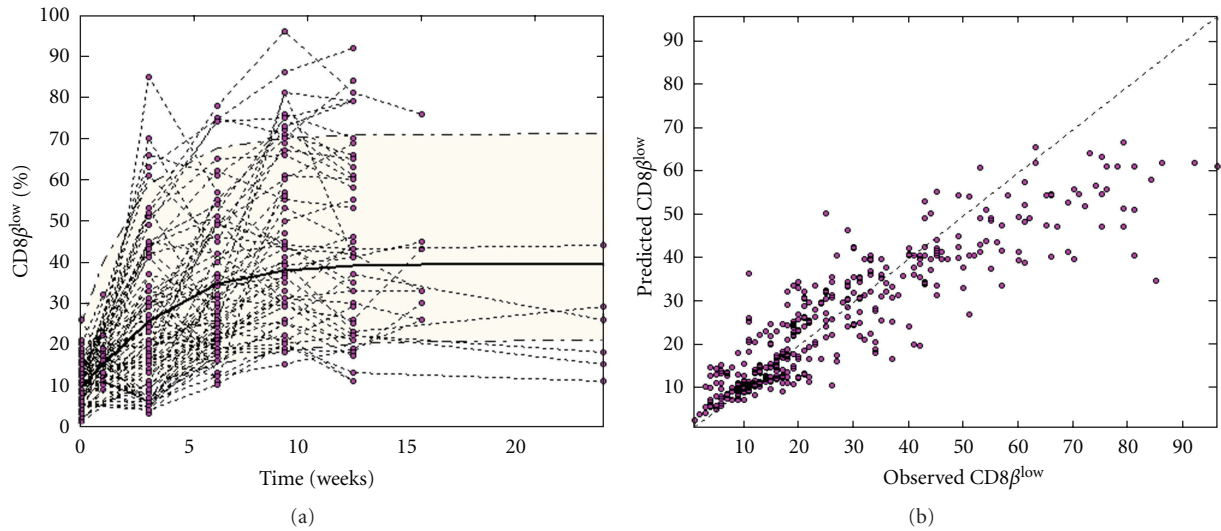


FIGURE 6: $\text{CD8}\beta^{\text{low}}$ model diagnostics. (a): Visual predictive check. (b): Individual predictions versus the actual observations.

impact of a change in the value of λ_E on the shape of the curve. Inter-animal variability in the model parameters (E_0 , λ_E , K) was assumed to be lognormal; the dose of infection and virus strain were evaluated as before as covariates. Only the dose of infection, expressed as \log_{10}/mL of CCID_{50} , was finally successfully integrated into the constant expansion rate of $\text{CD8}\beta^{\text{low}}$. With this covariate integration, the objective function was reduced by 33 points, and the variability on the λ_E parameter decreased by 44%.

The mean value of the maximal percentage (K) was estimated at 39.4%. The constant rate of $\text{CD8}\beta^{\text{low}}$ expansion increases as the dose increases, ranging from 0.08 weeks^{-1} for the lowest dose to 1.62 weeks^{-1} for the highest dose. This range is very similar to the range of the rate of increase of viral load. Consequently, we observe that the higher the

dose of infection, the stronger the expansion of $\text{CD8}\beta^{\text{low}}$. Notably, we observe a linear relationship between the rate of expansion of the $\text{CD8}\beta^{\text{low}}$ population and the rate of increase of viral load (Figure 5(a)). Figure 6, similarly to Figure 3, shows model diagnostics with a visual predictive check (Figure 6(a)) and individual predictions plotted against actual observations (Figure 6(b)). Correlations between predictions and observations are fairly good ($r^2 = 0.80$, $P < 0.001$), although the highest observations seem to be underestimated by the model. In fact, the proposed model is able to reproduce only the expansion of the $\text{CD8}\beta^{\text{low}}$ percentage, whereas in many cases the highest observed $\text{CD8}\beta^{\text{low}}$ percentages were followed by lower percentages at subsequent time points (see Figure 6(a)). The latter observation might be attributable to technical variability in

performing the laboratory measurements or to fluctuations around a saturation point.

4. Discussion

FIV is a major pathogen affecting cats and is recognized as a relevant model for the study of HIV infection. In particular, during the primary infection phase, the clinical signs and virus localization in FIV-infected cats have been shown to be similar to those observed in HIV infection [1]. The study of primary HIV infection is likely to shed new light on the development of the disease, as a relationship has been shown to exist between the characteristics of acute-stage HIV infection and progression to death due to AIDS [19, 20]. As primary infection in HIV might be difficult to document, the study of the early phase of FIV infection could be an alternative means of gaining insights into HIV that might contribute to the design of new efficient therapy.

In addition to being a valuable model for HIV, FIV on its own constitutes an important research interest. As a result of the growing prevalence and severity of FIV infection, an effective FIV vaccine is greatly needed in veterinary medicine [2]. The issues that researchers have faced in the process of FIV vaccine development are similar to those encountered for HIV, and it is believed that effective vaccines against HIV and against FIV will elicit cellular immune responses [21–24].

We performed a longitudinal analysis of important markers of FIV—that is, viral load and $CD8\beta^{low}$ percentage—in cats undergoing primary infection. The analysis was carried out retrospectively, using data from cats that were infected in an experimental protocol.

This analysis led us to propose two phenomenological models that correctly reproduced the time-evolution of $CD8\beta^{low}$ percentage and viremia during primary FIV infection in cats. These simple models allowed us to integrate, at the level of the parameters, the intersubject variability that often characterizes preclinical and clinical data.

Expansion of $CD8\beta^{low}$ percentage was modelled with a Gompertz law, and viremia was modelled using two exponential laws to reproduce the initial burst of viral load followed by decay. All model parameters were estimated with low-standard errors, and, as expected, variability was elevated for some of the parameters. Even if the models are phenomenological, some of the parameters, and in particular the rate of expansion of the $CD8\beta^{low}$ population and viral load, can be easily related to the shapes of the curves (see Figure 2 for illustration), and so can be easily interpreted. The dose of infection, expressed as \log_{10}/mL of CCID50, was found to be a relevant covariate of the rate of expansion of the $CD8\beta^{low}$ population and the rate of increase of viral load; this covariate explains a large part (up to 30%) of the inter-animal variability on the distribution of these two parameters. Finally, the rate of expansion of viral load and the rate of expansion of $CD8\beta^{low}$ percentage

were observed to be correlated ($r^2 = 0.73$, $P < 0.001$; see Figure 5(b)). Obviously, this correlation does not provide any clues regarding the mechanism of action of $CD8\beta^{low}$ or the relationship between the $CD8^+$ T-cell subpopulation and viremia, but it reinforces the prevalent hypothesis that $CD8\beta^{low}$ percentage is a relevant marker of FIV progression.

The results we obtained with the proposed models may provide insight into the time course of viremia or viral load and the size of the $CD8\beta^{low}$ population following infection. Our study points to phenomenological models as a potentially valuable complement to the numerous mechanistic models used to study HIV infection and AIDS progression. For example, researchers have identified a linear relationship between a patient's viral load, taken as the average of all the patient's viral load measurements (allegedly compatible with the concept of a viral set point), and his or her survival time [25, 26]. Our study provides evidence that disease progression in patients can be well described by a simple phenomenological model that does not rely on any biological assumptions. The dynamic approach we adopted here could provide insights into the link between viremia and patient survival [26]. Indeed, the analysis of the time course of viral load might be a better predictor of survival than the average viral load parameter used by Arnaout et al. [25].

5. Summary

Cats infected with the feline immunodeficiency virus (FIV) develop an acquired immunodeficiency syndrome (AIDS), similarly to humans infected with HIV. FIV infection causes an acute viremia, which decreases after several weeks, and the appearance of a subpopulation of activated $CD8^+$ T cells that we refer to as $CD8\beta^{low}$ cells. The expansion of this activated T-cell population is recognized as an important marker of FIV infection and disease. Characterization of the $CD8\beta^{low}$ population's complex pattern of expansion, including its correlation with other disease markers such as viral load, is likely to increase researchers' understanding of FIV infection and AIDS pathogenesis. We propose two simple and independent mathematical equations to analyze the time-evolution of $CD8\beta^{low}$ population size and of viral load during primary infection in cats with FIV. We develop the models using a population approach and mixed-effects regression techniques, based on repeated measurements in more than 100 cats infected with FIV.

Acknowledgement

The authors wish to thank Lyon Biopôle (project FIV-VAX) for financial support.

References

- [1] M. Bendinelli, M. Pistello, S. Lombardi et al., "Feline immunodeficiency virus: an interesting model for AIDS studies and an important cat pathogen," *Clinical Microbiology Reviews*, vol. 8, no. 1, pp. 87–112, 1995.
- [2] R. Paillot, S. Richard, F. Bloas et al., "Toward a detailed characterization of feline immunodeficiency virus-specific T

- cell immune responses and mediated immune disorders," *Veterinary Immunology and Immunopathology*, vol. 106, no. 1-2, pp. 1-14, 2005.
- [3] J. J. Callanan, H. Thompson, S. R. Toth et al., "Clinical and pathological findings in feline immunodeficiency virus experimental infection," *Veterinary Immunology and Immunopathology*, vol. 35, no. 1-2, pp. 3-13, 1992.
 - [4] A. M. Beebe, N. Dua, T. G. Faith, P. F. Moore, N. C. Pedersen, and S. Dandekar, "Primary stage of feline immunodeficiency virus infection: viral dissemination and cellular targets," *Journal of Virology*, vol. 68, no. 5, pp. 3080-3091, 1994.
 - [5] J. N. Flynn, S. Dunham, A. Mueller, C. Cannon, and O. Jarrett, "Involvement of cytolytic and non-cytolytic T cells in the control of feline immunodeficiency virus infection," *Veterinary Immunology and Immunopathology*, vol. 85, no. 3-4, pp. 159-170, 2002.
 - [6] W. Song, E. W. Collisson, P. M. Billingsley, and W. C. Brown, "Induction of feline immunodeficiency virus-specific cytolytic T-cell responses from experimentally infected cats," *Journal of Virology*, vol. 66, no. 9, pp. 5409-5417, 1992.
 - [7] Y. Inoshima, Y. Ikeda, M. Kohmoto et al., "Persistence of high virus neutralizing antibody titers in cats experimentally infected with feline immunodeficiency virus," *Journal of Veterinary Medical Science*, vol. 58, no. 9, pp. 925-927, 1996.
 - [8] D. H. Gebhard, J. L. Dow, T. A. Childers, J. I. Alvelo, M. B. Tompkins, and W. A. F. Tompkins, "Progressive expansion of an L-selectin-negative CD8 cell with anti-feline immunodeficiency virus (FIV) suppressor function in the circulation of FIV-infected cats," *Journal of Infectious Diseases*, vol. 180, no. 5, pp. 1503-1513, 1999.
 - [9] D. Wodarz and M. A. Nowak, "Mathematical models of HIV pathogenesis and treatment," *BioEssays*, vol. 24, no. 12, pp. 1178-1187, 2002.
 - [10] A. S. Perelson, A. U. Neumann, M. Markowitz, J. M. Leonard, and D. D. Ho, "HIV-1 dynamics in vivo: virion clearance rate, infected cell life-span, and viral generation time," *Science*, vol. 271, no. 5255, pp. 1582-1586, 1996.
 - [11] A. S. Perelson, P. Essunger, Y. Cao et al., "Decay characteristics of HIV-1-infected compartments during combination therapy," *Nature*, vol. 387, no. 6629, pp. 188-191, 1997.
 - [12] M. A. Nowak and C. R. M. Bangham, "Population dynamics of immune responses to persistent viruses," *Science*, vol. 272, no. 5258, pp. 74-79, 1996.
 - [13] M. A. Nowak and R. M. May, *Virus Dynamics: Mathematical Principles of Immunology and Virology*, vol. 12, Oxford University Press, Oxford, UK, 2000.
 - [14] M. A. Stafford, L. Corey, Y. Cao, E. S. Daar, D. D. Ho, and A. S. Perelson, "Modeling plasma virus concentration during primary HIV infection," *Journal of Theoretical Biology*, vol. 203, no. 3, pp. 285-301, 2000.
 - [15] M. J. Lindstrom and D. M. Bates, "Nonlinear mixed effects models for repeated measures data," *Biometrics*, vol. 46, no. 3, pp. 673-687, 1990.
 - [16] A. Samson, M. Lavielle, and F. Mentré, "The SAEM algorithm for group comparison tests in longitudinal data analysis based on non-linear mixed-effects model," *Statistics in Medicine*, vol. 26, no. 27, pp. 4860-4875, 2007.
 - [17] M. O. Karlsson and R. M. Savic, "Diagnosing model diagnostics," *Clinical Pharmacology and Therapeutics*, vol. 82, no. 1, pp. 17-20, 2007.
 - [18] U. Wahlby, E. N. Jonsson, and M. O. Karlsson, "Comparison of stepwise covariate model building strategies in population pharmacokinetic-pharmacodynamic analysis," *AAPS Pharm-Sci*, vol. 4, no. 4, 2002.
 - [19] P. Vanhems, B. Hirschel, A. N. Phillips et al., "Incubation time of acute human immunodeficiency virus (HIV) infection and duration of acute HIV infection are independent prognostic factors of progression to AIDS," *Journal of Infectious Diseases*, vol. 182, no. 1, pp. 334-337, 2000.
 - [20] P. Vanhems, N. Voirin, B. Hirschel et al., "Incubation and duration of specific symptoms at acute retroviral syndrome as independent predictors of progression to AIDS," *Journal of Acquired Immune Deficiency Syndromes*, vol. 32, no. 5, pp. 542-544, 2003.
 - [21] K. H. J. Siebelink, E. Tijhaar, R. C. Huisman et al., "Enhancement of feline immunodeficiency virus infection after immunization with envelope glycoprotein subunit vaccines," *Journal of Virology*, vol. 69, no. 6, pp. 3704-3711, 1995.
 - [22] J. A. Karlas, K. H. J. Siebelink, M. A. V. Peer et al., "Vaccination with experimental feline immunodeficiency virus vaccines, based on autologous infected cells, elicits enhancement of homologous challenge infection," *Journal of General Virology*, vol. 80, no. 3, pp. 761-765, 1999.
 - [23] S. Giannecchini, P. Isola, O. Sichi et al., "AIDS vaccination studies using an ex vivo feline immunodeficiency virus model: failure to protect and possible enhancement of challenge infection by four cell-based vaccines prepared with autologous lymphoblasts," *Journal of Virology*, vol. 76, no. 14, pp. 6882-6892, 2002.
 - [24] J. Richardson, S. Broche, S. Baud et al., "Lymphoid activation: a confounding factor in AIDS vaccine development?" *Journal of General Virology*, vol. 83, no. 10, pp. 2515-2521, 2002.
 - [25] R. A. Arnaot, A. L. Lloyd, T. R. O'Brien, J. J. Goedert, J. M. Leonard, and M. A. Nowak, "A simple relationship between viral load and survival time in HIV-1 infection," *Proceedings of the National Academy of Sciences of the United States of America*, vol. 96, no. 20, pp. 11549-11553, 1999.
 - [26] J. W. Mellors, A. Muñoz, J. V. Giorgi et al., "Plasma viral load and CD4+ lymphocytes as prognostic markers of HIV-1 infection," *Annals of Internal Medicine*, vol. 126, no. 12, pp. 946-954, 1997.

Research Article

Relaxation Estimation of RMSD in Molecular Dynamics Immunosimulations

Wolfgang Schreiner,¹ Rudolf Karch,¹ Bernhard Knapp,¹ and Nevena Ilieva²

¹ Section of Biosimulation and Bioinformatics, Center for Medical Statistics, Informatics, and Intelligent Systems (CeMSIIS), Medical University of Vienna, Spitalgasse 23, 1090 Vienna, Austria

² Institute for Nuclear Research and Nuclear Energy (INRNE), Bulgarian Academy of Sciences, 72, Tzarigradsko Chaussee, 1784 Sofia, Bulgaria

Correspondence should be addressed to Rudolf Karch, rudolf.karch@meduniwien.ac.at

Received 29 June 2012; Revised 1 August 2012; Accepted 7 August 2012

Academic Editor: Francesco Pappalardo

Copyright © 2012 Wolfgang Schreiner et al. This is an open access article distributed under the Creative Commons Attribution License, which permits unrestricted use, distribution, and reproduction in any medium, provided the original work is properly cited.

Molecular dynamics simulations have to be sufficiently long to draw reliable conclusions. However, no method exists to prove that a simulation has converged. We suggest the method of “lagged RMSD-analysis” as a tool to judge if an MD simulation has not yet run long enough. The analysis is based on RMSD values between pairs of configurations separated by variable time intervals Δt . Unless $\text{RMSD}(\Delta t)$ has reached a stationary shape, the simulation has not yet converged.

1. Introduction

Mathematical modeling and computational biology have proved extremely successful in the efforts to understand the mechanisms of immunologic reactions, for example, in modeling the T-cell proliferation dynamics following hepatitis C, HIV infection [1], or the growth of an immunogenic tumor [2]. Methods of statistical mechanics may successfully be applied in order to quantitatively understand the immune system [3, 4], and different modeling approaches are adequate for acquired immunity, as surveyed in a seminal paper by Perelson and Weisbush [5]. Modeling and simulation can be performed on different levels, starting at the top level with agent-based models [6, 7] for the cooperation of numerous large biomolecules in the formation of the immune synapse [8–11] down to more detailed models of antigen binding [12], recognition, and signaling [13–20]. T-cell proliferation modulated by interleukin 2 has been simulated [21]. Applications aiming to predict the reaction to epitopes [22] improved vaccine design [23], vaccination

against tumors [24], and for improved patient care have been devised [25–27], also in personalized medicine [28]. In particular, the mechanisms how T-cell receptors (TCRs) detect antigen peptides (p) presented by major histocompatibility complex (MHC) molecules can be investigated by molecular dynamics (MD) on a molecular or even atomic level [29–32]. However, TCRpMHC complexes are huge protein complexes, which have to be studied in water, which adds an even larger number of atoms to model and simulate. For these reasons, sufficiently long simulations are mandatory in order to obtain realistic results. This is even more so since molecular recognition phenomena may operate on rather long timescales as compared to the length of usual MD trajectories. Hence, efforts to assess sampling quality are mandatory in such simulations.

Given the trajectory of an actual MD simulation, it is clear from first principles that no formal check whatsoever can prove that complete sampling has been achieved. If parts of the phase space have not been visited yet, there is no possibility that this becomes evident from looking

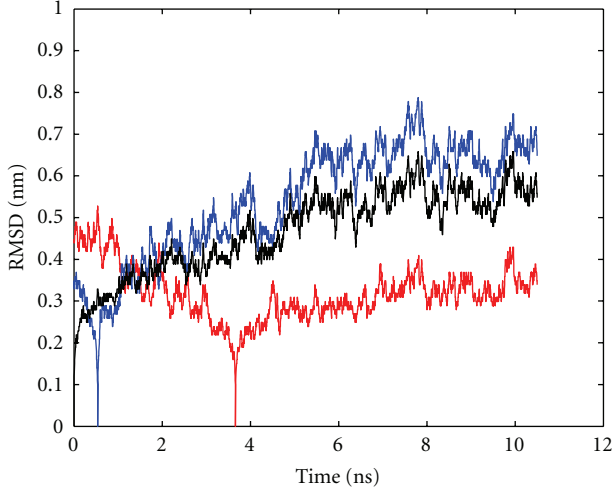


FIGURE 1: RMSD as a function of time for trajectory 1 (10 ns). Black curve: RMSD between first configuration and all successive ones. Blue curve: for a given configuration (t_j), RMSD to each of the other configurations of the same trajectory was computed and averaged, yielding $\overline{\text{RMSD}}(t_j)$. That value of t_j for which $\overline{\text{RMSD}}(t_j)$ is maximum is then adopted as a reference (t_1) to plot RMSD values of the whole trajectory. Red curve: as blue curve, but for minimum $\overline{\text{RMSD}}(t_j)$. Note that the RMSD between the reference configuration and itself is zero by definition.

only at data from those other parts that have been visited. Zhang et al. [33] proposed a formal approach to decompose the phase space into Voronoi polyhedra [34, 35].

At any rate, formal checks of sampling quality can only draw on simulation data already produced and *at the most detect possible shortcomings* of those trajectories. The situation is analogous to tests for the randomness of pseudorandom-number generators [36]. One can never prove randomness as such. It is only possible to detect specific deviations from randomness, such as serial correlations—and any such detection works only with a preselected error rate.

Likewise, MD trajectories may be investigated for specific markers of nonrandomness, the most important type being trends of energy and molecular deformations. This work focuses on the latter, deviations in shape being quantified via the *root mean square deviation* (RMSD) [37] at time t_2 with respect to a given reference structure at time t_1 :

$$\text{RMSD}(t_1, t_2) = \left[\frac{1}{N} \sum_{i=1}^N \|\mathbf{x}_i(t_2) - \mathbf{x}_i(t_1)\|^2 \right]^{1/2}, \quad (1)$$

where $\mathbf{x}_i(t)$ is the position of atom i at time t and N is the total number of atoms in the molecule.

Often, the first frame of a trajectory (t_1) is used as a reference, and values of $\text{RMSD}(t_1, t_2)$ are computed for all successive ($t_2 > t_1$) frames; see the black curve in Figure 1. RMSD monitored this way shows large rapid fluctuations on top of long-term variations and jumps. Generally, it is difficult to identify such long-term variations, which may

relate to functional modes. A recent study [38] reflected the insufficiency of visual RMSD inspection alone.

Extensive work has been published on using the RMSD for the characterization of structural changes, drifts, and trends; see [33] and the references cited therein. Grossfield and Zuckerman [39] gives a seminal conceptual discussion of ergodicity, absolute and relative convergence and proposes checks for overall sampling quality. Block averaging was proposed [40] to reduce short-term fluctuations and to obtain more reliable indicators of long-term trends. However, averaging RMSD over all configurations within a block involves many different time intervals $\Delta t = t_j - t_i$, thus reducing the specificity of the resulting average for one particular time interval.

For this reason we consider the RMSD between pairs of configurations separated by a constant time lag Δt as described in Section 2.2.1. In this way we obtain more stable estimates (averages) which are nevertheless perfectly specific for a given time interval Δt .

2. Materials and Methods

2.1. Molecular Dynamics Simulations

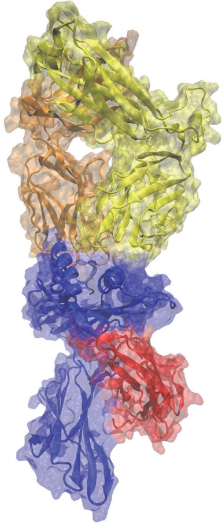
2.1.1. Employed Structures. We applied the proposed methodology to a total of 6 MD simulations. For this purpose we used 2 different TCRpMHC complexes: an immunogenic wild-type peptide bound between TCR/MHC and the same TCR/MHC with a less immunogenic mutant peptide. We employed the crystal structure of the LC13 TCR bound to HLA-B*08:01 and the Epstein Barr Virus peptide FLRGRAYGL. This structure is available from the Protein Data Bank (PDB) [41] via PDB accession code 1mi5 [42] and is referred to as wild-type. For the mutant complex we substituted the side chain of tyrosine at position 7 of the peptide to alanine (Y7A). This was performed using SCWRL [43] since we could previously show that this tool is most appropriate for mutations in pMHC complexes [44, 45].

The LC13 TCR in complex with the FLRGRAYGL peptide and HLA-B*08:01 is an ideal test set for molecular dynamics simulations since this complex was crystallized and described in its parts and as a whole. Initially Kjer-Nielsen et al. crystallized the TCR [46] and the MHC [47] separately while they published a structure of the whole TCRpMHC system [42] afterwards. These available data give substantial insight into the LC13/EBV/HLA-B*08:01 system and led to the choice of our wild-type and mutated system for this study. The whole system is illustrated in Figure 2.

2.1.2. Molecular Dynamics Simulation Protocol. The wild-type and the mutant complex were simulated in independent runs for 10, 50, and 200 ns yielding a total of 6 simulations (see Table 1). The following protocol for the simulations was employed. First, we minimized the energy of the systems using a steepest descent method. Then we immersed the complexes in explicit SPC [48] artificial water baths allowing for a minimal distance of 2 nm between the box boundary and the protein. Next, we warmed the complex up to

TABLE 1: Molecular dynamics simulation runs.

	t_{\max} (ns)	Δt_{config} (ps)	Peptide	n
Trajectory 1	10	3	FLRGRAYGL	3500
Trajectory 2	50	50	FLRGRAYGL	1000
Trajectory 3	200	50	FLRGRAYGL	4322
Trajectory 4	10	3	FLRGRAAGL	3500
Trajectory 5	50	50	FLRGRAAGL	1000
Trajectory 6	200	50	FLRGRAAGL	4322

FIGURE 2: Illustration of the LC13 TCR in complex with HLA-B*08:01. Blue: MHC, red: $\beta 2$ -microglobulin, gray: peptide, orange: TCR alpha-chain, yellow: TCR beta-chain.

310 K using position restraints. Finally, we carried out the simulations using GROMACS 4 [49] and the GROMOS96 force field [50]. All further parameters were set in accordance with [51].

2.1.3. RMSD Calculation. After the simulations were finished, we calculated the RMSD values for each configuration in a given trajectory with respect to every other configuration of the same trajectory using the standard *g_rms* function of GROMACS. This yields an $n \times n$ matrix of RMSD values where n is the number of configurations in the trajectory.

2.2. RMSD between Configurations of Trajectories

2.2.1. Averaging and Modeling of Lagged RMSD. Given one configuration $\mathbf{x}(t_i)$ of an MD simulation as a reference, the RMSD to some other configuration $\mathbf{x}(t_j)$ may be considered a “distance measure” along the time interval $\Delta t = t_j - t_i$. If Δt is short enough, it may be shifted along the whole trajectory and RMSD values be sampled. The average $\overline{\text{RMSD}}(\Delta t)$ is characteristic for the difference between configurations separated by Δt in the particular simulation run considered.

Small values of Δt characterize configurations close to each other in time. Increasing Δt means to compare configurations more distant to each other in time, which

are—intuitively speaking—“less related” to each other. This fact should be reflected in $\overline{\text{RMSD}}(\Delta t)$ for increasing values of Δt .

As Δt increases, dependences should diminish and approach the level of “unrelated” or “independent” configurations. In order to quantify such a saturation trend, we applied the *Hill equation* [52]:

$$\overline{\text{RMSD}}(\Delta t) = \frac{a \cdot \Delta t^\gamma}{t^\gamma + \Delta t^\gamma}, \quad (2)$$

where the parameter a reflects the maximum value to which the function is asymptotic (“plateau value” $\overline{\text{RMSD}}(\Delta t \rightarrow \infty)$), τ is the time lag Δt for which $\overline{\text{RMSD}}(\Delta t) = a/2$ (i.e., the value of Δt for which half-saturation is achieved), and the *Hill coefficient* γ is a parameter that determines the shape, that is, the level of sigmoidicity, of the model functions. The parameters were estimated by fitting the *Hill equation* (2) to the measured values of $\overline{\text{RMSD}}(\Delta t)$ using the *nlinfit* function as implemented in the *Statistics Toolbox* of MATLAB (Mathworks, Natick, MA, USA). The maximum time lag Δt was chosen half the total simulation time of the respective trajectory.

2.2.2. Assessing the Influence of Initial Conditions. The initial phase $t \leq t_{\text{offset}}$ of each MD simulation strongly depends on the starting configuration, usually a crystal structure, which can by no means be representative for a configuration obtained from a trajectory. This is even true after energy minimization and warming up. Hence, if the initial phase of an MD trajectory is included in $\overline{\text{RMSD}}(\Delta t)$, a bias will result. This is not only true for individual values of $\overline{\text{RMSD}}(\Delta t)$ but also for the parameters estimated from the fit. In particular, the limiting plateau value $a = \overline{\text{RMSD}}(\Delta t = \infty)$ will also be biased and depend on t_{offset} : in fact, $a = a(t_{\text{offset}})$. We modeled this dependence as

$$a(t_{\text{offset}}) = a_0 + \beta \cdot \exp(-\lambda \cdot t_{\text{offset}}), \quad (3)$$

where a_0 is the limiting value, $a_0 = a(t_{\text{offset}} = \infty)$, and β and λ are scaling parameters. Note that a_0 is an extrapolated estimate for $\overline{\text{RMSD}}(\Delta t = \infty)$ and $t_{\text{offset}} = \infty$, that is, the estimate for an RMSD between two totally unrelated configurations of a trajectory, independent of initial phase effects.

Values for t_{offset} were selected in the interval $0 \leq t_{\text{offset}} \leq t_{\max}/2$, where t_{\max} denotes the total simulation time of the respective trajectory.

3. Results and Discussion

3.1. Convergence of RMSD with Increasing Time Lag. Each panel of Figure 3 shows a representative plot (for reasons of conciseness we display results in the figures only for trajectory 1–3) of mean RMSD values (red circles, y -axis) obtained between configurations of one MD trajectory (see figure caption and Table 1), separated by respective time lags Δt (x -axis). As the time-lag between configurations increases, mean RMSD approaches a plateau.

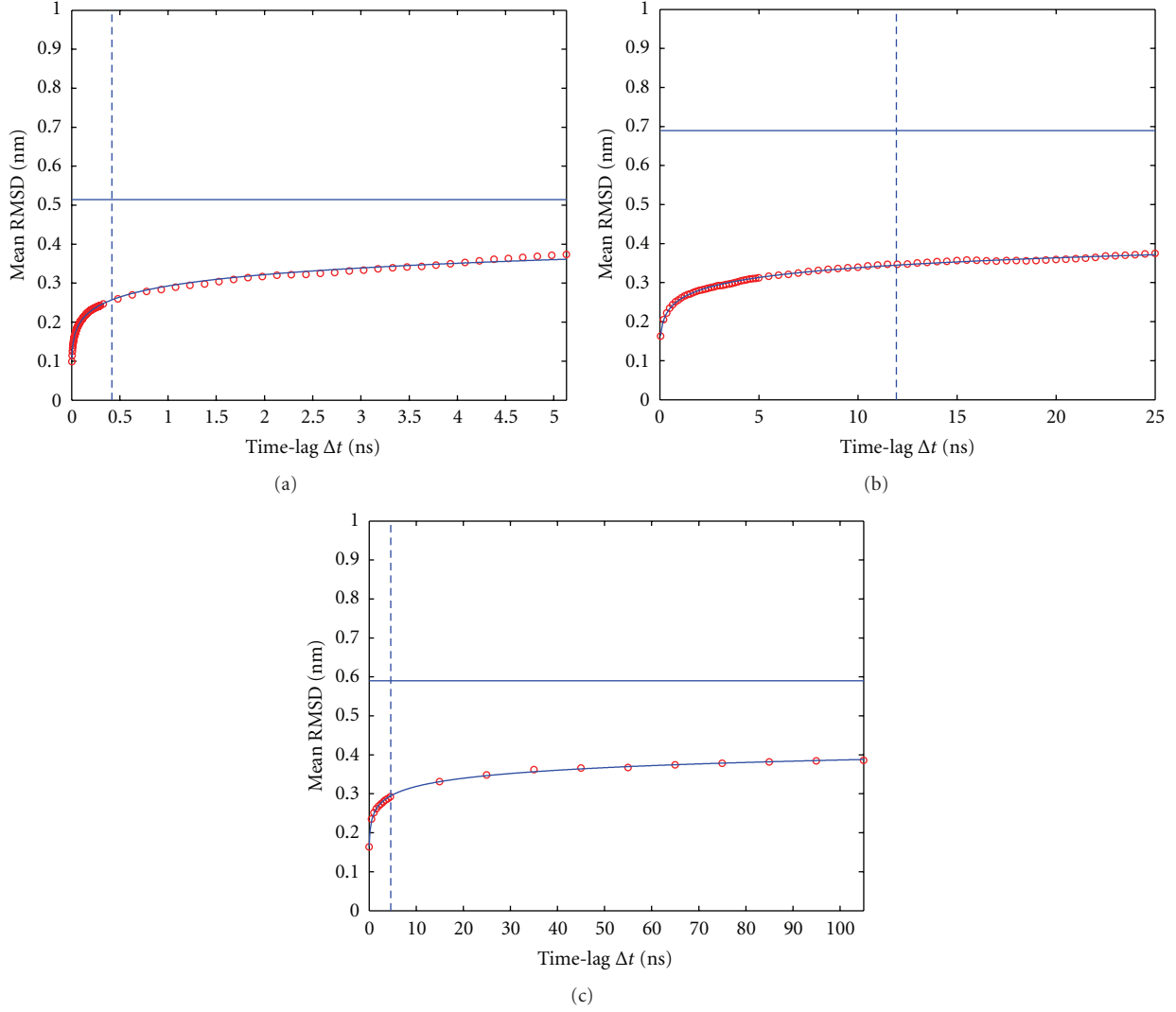


FIGURE 3: Dependence of mean RMSD on the time lag Δt for $t_{\text{offset}} = 0$. (a) 10 ns trajectory 1, (b) 50 ns trajectory 2, (c) 200 ns trajectory 3; see Table 1. Note that due to the different total durations of the simulations, the maximum time lag considered (equal to half the simulation length) varies. Vertical lines indicate the time interval τ , for which half-saturation is achieved; see also (2). The horizontal line indicates the estimated plateau of the mean RMSD, corresponding to the parameter a in (2).

Fits of the model (2) to the values of $\overline{\text{RMSD}}(\Delta t)$ are displayed as solid lines. Parameters obtained from the fits can readily be interpreted as follows. The estimate for parameter a in (2) represents the limiting value of $\overline{\text{RMSD}}(\Delta t)$ and is indicated by the horizontal line. The estimate of the parameter τ corresponds to a “characteristic” (“half-saturation”) time interval Δt and is shown as a vertical line in the plots.

Note that the initial phase of each trajectory strongly determines the shape of $\overline{\text{RMSD}}(\Delta t)$ which should be properly represented by the fitted model. In contrast, the remainder of each trajectory is characteristic for the long-term trend of $\overline{\text{RMSD}}(\Delta t)$. Although it shows much smaller changes in RMSD, the remainder contains naturally by far more data points as compared to the initial phase. To achieve an appropriate balance, we increased the lag length in small steps during an initial phase (cf. the initially dense succession

of red circles in Figure 3) and in larger steps (more loose succession of circles) later on. This procedure puts increased weight on the data points for the initial phase.

3.2. Influence of the Offset. Applying different temporal offsets t_{offset} before starting to analyze the respective trajectories changes the dependence of $\text{RMSD}(\Delta t)$ as a function of the time lag Δt ; see the typical results displayed in Figure 4.

The larger the offset t_{offset} from the start configuration, the smaller the time lag Δt necessary for the system to level off to its $\overline{\text{RMSD}}$ plateau. The exemplary display of the dependence of fitted parameters on t_{offset} , as shown previously, is systematically analyzed as follows; see Figure 5. With increasing t_{offset} both the plateau value a and the half-saturation parameter t decrease, whereas the shape

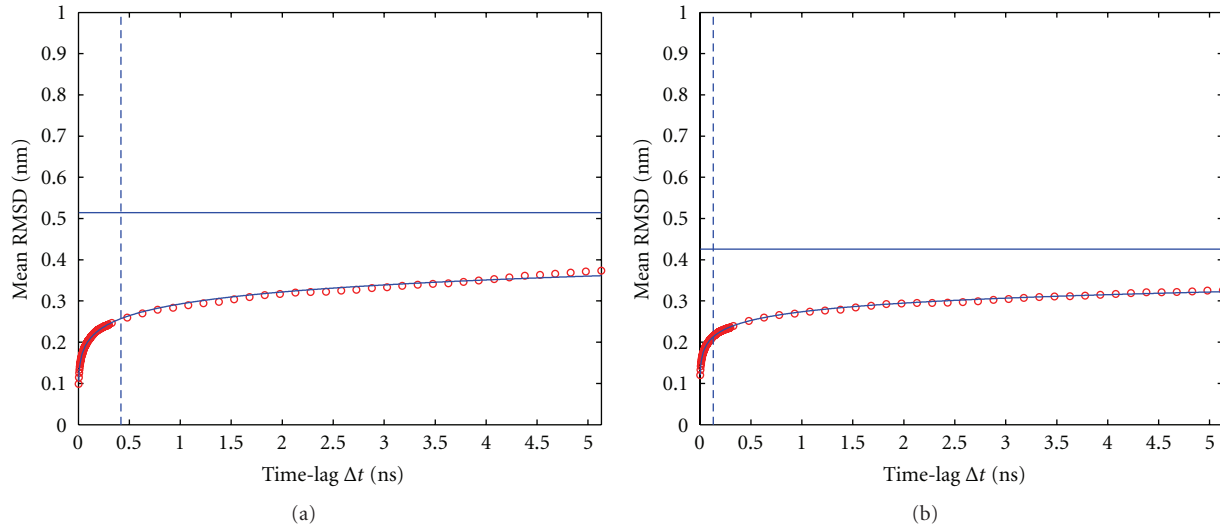


FIGURE 4: Dependence of mean RMSD on t_{offset} for trajectory 1 (10 ns). (a): $t_{\text{offset}} = 0$ ps, (b): $t_{\text{offset}} = 200$ ps. Vertical lines indicate the time lag τ , for which half-saturation is achieved; see also (2). The horizontal line indicates the estimated plateau of the mean RMSD, corresponding to the parameter a in (2).

parameter γ is fairly constant and almost independent of t_{offset} .

In a next step the systematic dependence of the extrapolated plateau on t_{offset} was fitted via (3); see Figure 6. The monoexponential decay model of (3) represents the most parsimonious choice, given the shape of the simulation results as displayed in Figure 6.

Figures 6(a)–6(c) illustrates the influence of the offset t_{offset} from the start configuration on the respective $\overline{\text{RMSD}}$ plateau values as estimated from the parameter a of the model (2). $\overline{\text{RMSD}}$ plateau values tend to decrease with increasing t_{offset} .

4. Conclusions

For molecular dynamics simulations of proteins, questions of “convergence” and sampling are important issues if sensible conclusions are to be drawn from such simulations. Since convergence of a particular simulation (in the sense that statistical sampling of the phase space is complete enough with respect to the specific phenomena studied) cannot be judged in advance [39], various techniques have been advised to demonstrate that a simulation has not yet converged [37, 53–56].

Here, we propose a method to assess if a simulation has *not* yet run long enough, based on RMSD analysis of successive configurations of a given MD trajectory, separated by time lags Δt of varying length (up to half the total simulation time). As long as a simulation has not yet converged, the shape of the function $\overline{\text{RMSD}}(\Delta t)$ still considerably depends on t_{offset} , that is, the time point along the trajectory, where the analysis interval Δt starts. As t_{offset} is large enough, the shape of $\overline{\text{RMSD}}(\Delta t)$ becomes stationary; that is, in Figure 4 the shape of the mean RMSD curve is different in the left and right panel, but further increasing

t_{offset} would not further change its overall appearance. This is also reflected in the respective model parameters, converging to constant values for large values of t_{offset} ; see Figure 5.

To describe this Δt dependence of the mean RMSD values, $\overline{\text{RMSD}}(\Delta t)$, for a given t_{offset} , the Hill function was used. This function type is frequently applied in enzyme kinetics to model saturation phenomena together with the number of reactive sites on an enzyme. In the present work, the Hill function proved flexible enough to model the functional form of $\overline{\text{RMSD}}(\Delta t)$ and to identify the respective parameters (plateau value, shape parameter, and half-saturation time). Contrary to a simple exponential saturation function, the Hill function is able to model different levels of sigmoidicity.

In order to quantify the influence of the initial conditions and the equilibration phase on $\text{RMSD}(\Delta t)$, we systematically increased the time t_{offset} before starting to analyze each trajectory. With the exception of the shape parameter γ all the other parameters of the Hill function describing $\overline{\text{RMSD}}(\Delta t)$ exhibit a distinctive dependence on the initial phase of the trajectories and thus indicate that biased estimates would result if the initial phase would be included in the analysis.

As pointed out in the introduction, the method proposed here combines the smoothing effect of averaging, while retaining the specificity of a precise time interval between configurations being compared. For example, the height of the extrapolated $\overline{\text{RMSD}}$ plateau a_0 (see Figure 6) may be interpreted as “configurational distance” between two arbitrarily selected, totally unrelated configurations of the particular part of phase space currently visited. If one chooses an arbitrary configuration out of it as the reference, all others visited by the trajectory will have an average distance a_0 . In contrast, Figure 1 shows two limiting cases of reference configurations: (i) the configuration with maximum average distance (i.e., RMSD) to all others (blue curve),

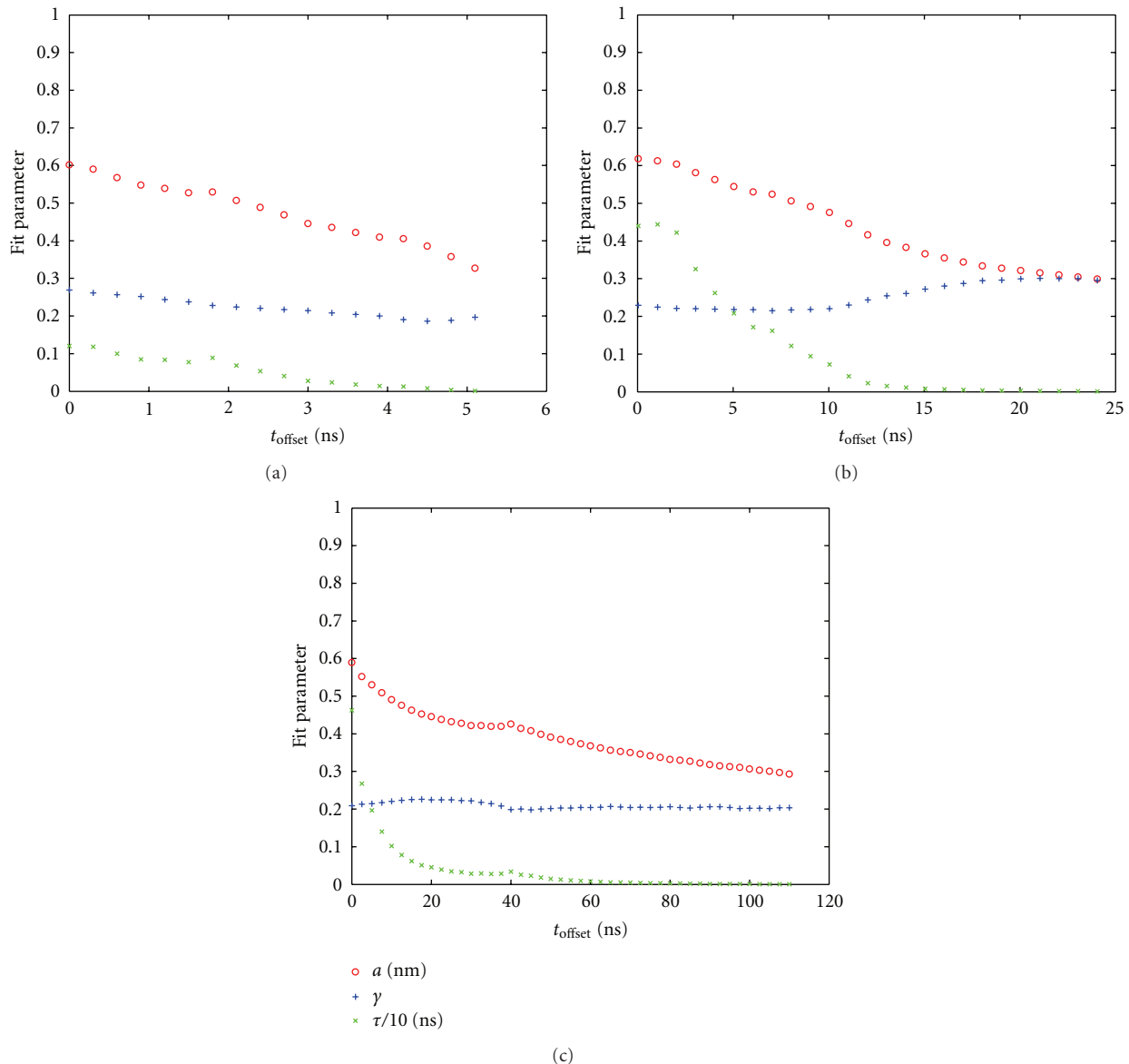


FIGURE 5: Increasing t_{offset} changes fitted parameters of $\overline{\text{RMSD}}(\Delta t)$, (2). (a) 10 ns trajectory, (b) 50 ns trajectory, (c) 200 ns trajectory; see Table 1.

which represents the “maximum outlier” ever seen in this trajectory and (ii) the configuration with minimum average distance (i.e., RMSD) to all others (red curve), which is “most central” within the trajectory.

Note that extrapolated plateau values are significantly larger than the $\overline{\text{RMSD}}(\Delta t)$ actually reached in the trajectories (see Figure 3). Only if we consider the extrapolated plateau as a function of t_{offset} , we obtain realistic (i.e., lower) estimates (see Figure 6) to aim at during actual simulations. In this sense, we may attribute the proposed fitting procedure some forecast capability regarding the level of RMSD to be finally expected if the trajectory were carried on. This extrapolated mean RMSD corresponds to pairs of configurations separated by time intervals large enough to consider such configurations approximately uncorrelated,

independent representatives of the configuration space of the respective molecule.

Likewise, the “half-saturation time” τ obtained from the fit decreases with increasing t_{offset} . Thus, taking configurations with large enough t_{offset} as a reference, it takes only a short time to get close to the $\overline{\text{RMSD}}$ plateau a_0 . In each panel of Figure 5, the parameter τ approaches an almost constant level at about half the maximum t_{offset} considered (i.e., 25% of the total simulation time). This might suggest that—regardless of the total simulation length—the fraction of usable (independent) configurations remains the same (final 75% of the trajectory). As the length of the simulation run increases, the criterion derived from the run itself gets increasingly more stringent. From the 200 ns run the first 50 ns should be discarded, which is more than 5 times the

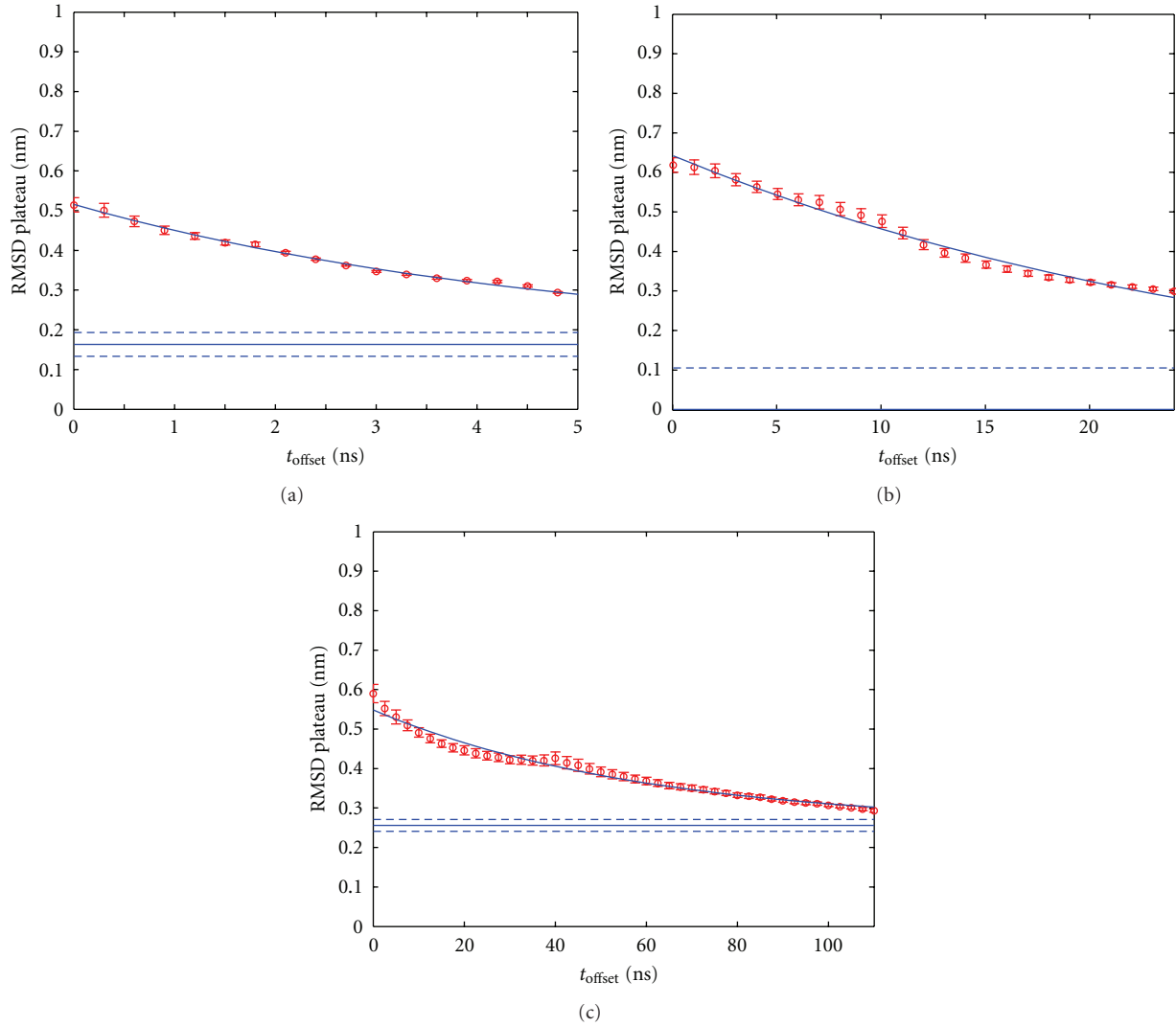


FIGURE 6: Fit and extrapolation of $\overline{\text{RMSD}}$ plateau values for increasing t_{offset} . (a) 10 ns trajectory 1, (b) 50 ns trajectory 2, (c) 200 ns trajectory 3; see Table 1. Red circles represent plateau values $a(t_{\text{offset}})$ the error bars denote their asymptotic standard errors. The solid blue curve shows a nonlinear least-squares fit of (3) to the plateau values $a(t_{\text{offset}})$. From the latter fit the limiting plateau value $a_0 = a(t_{\text{offset}} = \infty)$ was extracted and is shown as a solid horizontal line together with its asymptotic standard error as obtained from the fit of (3).

total length of the 10 ns trajectory. If using the latter as a basis of estimate, however, the last 7.5 ns seem to be trustable.

Although the analysis reported in the present work is specific to TCRpMHC complexes, we expect the method of lagged RMSD analysis to be applicable to similar molecular systems, such as membrane proteins comparable in size and structure. The approach presented here is designed to assess the degree of convergence of MD simulations and hence the statistical quality of conclusions drawn from such simulations.

Acknowledgments

The authors are thankful to L. Litov and P. Petkov for the discussions and constructive remarks. This work was supported in part by the Bulgarian Science Fund under Grant

DCoE-02/1/2009 and in part by the Austrian Science Fund (FWF P22258-B12).

References

- [1] A. S. Perelson, “Modelling viral and immune system dynamics,” *Nature Reviews Immunology*, vol. 2, no. 1, pp. 28–36, 2002.
- [2] V. A. Kuznetsov, I. A. Makalkin, M. A. Taylor, and A. S. Perelson, “Nonlinear dynamics of immunogenic tumors: parameter estimation and global bifurcation analysis,” *Bulletin of Mathematical Biology*, vol. 56, no. 2, pp. 295–321, 1994.
- [3] A. Barra and E. Agliari, “A statistical mechanics approach to autopoietic immune networks,” *Journal of Statistical Mechanics*, vol. 2010, no. 7, Article ID P07004, 2010.
- [4] A. Barra and E. Agliari, “Stochastic dynamics for idiotypic immune networks,” *Physica A*, vol. 389, no. 24, pp. 5903–5911, 2010.

- [5] A. S. Perelson and G. Weisbush, "Immunology for physicists," *Reviews of Modern Physics*, vol. 69, no. 4, pp. 1219–1267, 1997.
- [6] J. A. Adam, "Effects of vascularization on lymphocyte/tumor cell dynamics: qualitative features," *Mathematical and Computer Modelling*, vol. 23, no. 6, pp. 1–10, 1996.
- [7] Y. Vodovotz, G. Clermont, C. Chow, and G. An, "Mathematical models of the acute inflammatory response," *Current Opinion in Critical Care*, vol. 10, no. 5, pp. 383–390, 2004.
- [8] N. J. Burroughs and C. Wülfing, "Differential segregation in a cell-cell contact interface: the dynamics of the immunological synapse," *Biophysical Journal*, vol. 83, no. 4, pp. 1784–1796, 2002.
- [9] M. L. Dustin, "Stop and go traffic to tune T cell responses," *Immunity*, vol. 21, no. 3, pp. 305–314, 2004.
- [10] B. Favier, N. J. Burroughs, L. Wedderburn, and S. Valitutti, "TCR dynamics on the surface of living T cells," *International Immunology*, vol. 13, no. 12, pp. 1525–1532, 2001.
- [11] A. Lanzavecchia and F. Sallusto, "Antigen decoding by T lymphocytes: from synapses to fate determination," *Nature Immunology*, vol. 2, no. 6, pp. 487–492, 2001.
- [12] H. H. Lin, S. Ray, S. Tongchusak, E. L. Reinherz, and V. Brusic, "Evaluation of MHC class I peptide binding prediction servers: applications for vaccine research," *BMC Immunology*, vol. 9, article 8, 2008.
- [13] K. H. Lee, A. D. Holdorf, M. L. Dustin, A. C. Chan, P. M. Allen, and A. S. Shaw, "T cell receptor signaling precedes immunological synapse formation," *Science*, vol. 295, no. 5559, pp. 1539–1542, 2002.
- [14] E. Bell, "T-cell activation—T-cell-APC interactions," *Nature Reviews Immunology*, vol. 4, article 930, 2004.
- [15] Z. Borovsky, G. Mishan-Eisenberg, E. Yaniv, and J. Rachmilewitz, "Serial triggering of T cell receptors results in incremental accumulation of signaling intermediates," *Journal of Biological Chemistry*, vol. 277, no. 24, pp. 21529–21536, 2002.
- [16] K. Choudhuri, D. Wiseman, M. H. Brown, K. Gould, and P. A. van der Merwe, "T-cell receptor triggering is critically dependent on the dimensions of its peptide-MHC ligand," *Nature*, vol. 436, no. 7050, pp. 578–582, 2005.
- [17] M. L. Dustin, "The cellular context of T cell signaling," *Immunity*, vol. 30, no. 4, pp. 482–492, 2009.
- [18] D. Gil, A. G. Schrum, B. Alarcón, and E. Palmer, "T cell receptor engagement by peptide—MHC ligands induces a conformational change in the CD3 complex of thymocytes," *Journal of Experimental Medicine*, vol. 201, no. 4, pp. 517–522, 2005.
- [19] L. L. Jones, L. A. Colf, A. J. Bankovich et al., "Different thermodynamic binding mechanisms and peptide fine specificities associated with a panel of structurally similar high-affinity T cell receptors," *Biochemistry*, vol. 47, no. 47, pp. 12398–12408, 2008.
- [20] A. Lanzavecchia, G. Iezzi, and A. Viola, "From TCR engagement to T cell activation: a kinetic view of T cell behavior," *Cell*, vol. 96, no. 1, pp. 1–4, 1999.
- [21] C. T. H. Baker, G. A. Bocharov, and C. A. H. Paul, "Mathematical modelling of the interleukin-2 T-cell system: a comparative study of approaches based on ordinary and delay differential equations," *Journal of Theoretical Medicine*, vol. 2, pp. 117–128, 1997.
- [22] C. Bianca, "Mathematical modeling for keloid formation triggered by virus: malignant effects and immune system competition," *Mathematical Models and Methods in Applied Sciences*, vol. 21, no. 2, pp. 389–419, 2011.
- [23] F. Pappalardo, M. D. Halling-Brown, N. Rapin et al., "ImmunoGrid, an integrative environment for large-scale simulation of the immune system for vaccine discovery, design and optimization," *Briefings in Bioinformatics*, vol. 10, no. 3, pp. 330–340, 2009.
- [24] C. Bianca and M. Pennisi, "The triplex vaccine effects in mammary carcinoma: a nonlinear model in tune with SimTriplex," *Nonlinear Analysis: Real World Applications*, vol. 13, pp. 1913–1940, 2012.
- [25] F. Pappalardo, P. L. Lollini, F. Castiglione, and S. Motta, "Modeling and simulation of cancer immunoprevention vaccine," *Bioinformatics*, vol. 21, no. 12, pp. 2891–2897, 2005.
- [26] M. Pennisi, R. Catanuto, F. Pappalardo, and S. Motta, "Optimal vaccination schedules using simulated annealing," *Bioinformatics*, vol. 24, no. 15, pp. 1740–1742, 2008.
- [27] G. L. Zhang, D. S. DeLuca, D. B. Keskin et al., "MULTIPRED2: a computational system for large-scale identification of peptides predicted to bind to HLA supertypes and alleles," *Journal of Immunological Methods*, vol. 374, no. 1–2, pp. 53–61, 2011.
- [28] F. Pappalardo, P. Zhang, M. Halling-Brown et al., "Computational simulations of the immune system for personalized medicine: state of the art and challenges," *Current Pharmacogenomics and Personalized Medicine*, vol. 6, no. 4, pp. 260–271, 2008.
- [29] S. Wan, P. V. Coveney, and D. R. Flower, "Molecular basis of peptide recognition by the TCR: affinity differences calculated using large scale computing," *Journal of Immunology*, vol. 175, no. 3, pp. 1715–1723, 2005.
- [30] M. Zacharias and S. Springer, "Conformational flexibility of the MHC Class I $\alpha 1$ - $\alpha 2$ domain in peptide bound and free states: a molecular dynamics simulation study," *Biophysical Journal*, vol. 87, no. 4, pp. 2203–2214, 2004.
- [31] B. Knapp, U. Omasits, B. Bohle et al., "3-Layer-based analysis of peptide-MHC interaction: in silico prediction, peptide binding affinity and T cell activation in a relevant allergen-specific model," *Molecular Immunology*, vol. 46, no. 8-9, pp. 1839–1844, 2009.
- [32] B. Knapp, U. Omasits, W. Schreiner, and M. M. Epstein, "A comparative approach linking molecular dynamics of altered peptide ligands and MHC with *In Vivo* immune responses," *PLoS ONE*, vol. 5, no. 7, Article ID e11653, 2010.
- [33] X. Zhang, D. Bhatt, and D. M. Zuckerman, "Automated sampling assessment for molecular simulations using the effective sample size," *Journal of Chemical Theory and Computation*, vol. 6, no. 10, pp. 3048–3057, 2010.
- [34] M. Held, "VRONI: an engineering approach to the reliable and efficient computation of Voronoi diagrams of points and line segments," *Computational Geometry*, vol. 18, no. 2, pp. 95–123, 2001.
- [35] A. Okabe, B. Boots, K. Sugihara, S. N. Chiu, and D. G. Kendall, *Spatial Tessellations: Concepts and Applications of Voronoi Diagrams*, Chichester John Wiley & Sons, 2nd edition, 2000.
- [36] D. Knuth, *The Art of Computer Programming*, vol. 2 of *Seminumerical Algorithms*, Addison-Wesley, Reading, Mass, USA, 2nd edition, 1989.
- [37] A. E. García, "Large-amplitude nonlinear motions in proteins," *Physical Review Letters*, vol. 68, no. 17, pp. 2696–2699, 1992.
- [38] B. Knapp, S. Frantal, M. Cibena, W. Schreiner, and P. Bauer, "Is an intuitive convergence definition of molecular dynamics simulations solely based on the root mean square deviation possible?" *Journal of Computational Biology*, vol. 18, no. 8, pp. 997–1005, 2011.

- [39] A. Grossfield and D. M. Zuckerman, "Chapter 2 quantifying uncertainty and sampling quality in biomolecular simulations," *Annual Reports in Computational Chemistry*, vol. 5, pp. 23–48, 2009.
- [40] H. Flyvbjerg and H. G. Petersen, "Error estimates on averages of correlated data," *The Journal of Chemical Physics*, vol. 91, no. 1, pp. 461–466, 1989.
- [41] H. M. Berman, J. Westbrook, Z. Feng et al., "The protein data bank," *Nucleic Acids Research*, vol. 28, no. 1, pp. 235–242, 2000.
- [42] L. Kjer-Nielsen, C. S. Clements, A. W. Purcell et al., "A structural basis for the selection of Dominant $\alpha\beta$ T cell receptors in antiviral immunity," *Immunity*, vol. 18, no. 1, pp. 53–64, 2003.
- [43] A. A. Canutescu, A. A. Shelenkov, and R. L. Dunbrack, "A graph-theory algorithm for rapid protein side-chain prediction," *Protein Science*, vol. 12, no. 9, pp. 2001–2014, 2003.
- [44] B. Knapp, U. Omasits, and W. Schreiner, "Side chain substitution benchmark for peptide/MHC interaction," *Protein Science*, vol. 17, no. 6, pp. 977–982, 2008.
- [45] B. Knapp, U. Omasits, S. Frantal, and W. Schreiner, "A critical cross-validation of high throughput structural binding prediction methods for pMHC," *Journal of Computer-Aided Molecular Design*, vol. 23, no. 5, pp. 301–307, 2009.
- [46] L. Kjer-Nielsen, C. S. Clements, A. G. Brooks, A. W. Purcell, J. McCluskey, and J. Rossjohn, "The 1.5 Å crystal structure of a highly selected antiviral T cell receptor provides evidence for a structural basis of immunodominance," *Structure*, vol. 10, no. 11, pp. 1521–1532, 2002.
- [47] L. Kjer-Nielsen, C. S. Clements, A. G. Brooks et al., "The structure of HLA-B8 complexed to an immunodominant viral determinant: peptide-induced conformational changes and a mode of MHC class I dimerization," *Journal of Immunology*, vol. 169, no. 9, pp. 5153–5160, 2002.
- [48] H. J. Berendsen, J. P. M. Postma, W. F. Van Gunsteren, and J. Hermans, "Interaction models for water in relation to protein hydration," *Intermolecular Forces*, pp. 331–342, 1981.
- [49] B. Hess, C. Kutzner, D. van der Spoel, and E. Lindahl, "GRGMACS 4: algorithms for highly efficient, load-balanced, and scalable molecular simulation," *Journal of Chemical Theory and Computation*, vol. 4, no. 3, pp. 435–447, 2008.
- [50] C. Oostenbrink, A. Villa, A. E. Mark, and W. F. Van Gunsteren, "A biomolecular force field based on the free enthalpy of hydration and solvation: the GROMOS force-field parameter sets 53A5 and 53A6," *Journal of Computational Chemistry*, vol. 25, no. 13, pp. 1656–1676, 2004.
- [51] U. Omasits, B. Knapp, M. Neumann et al., "Analysis of key parameters for molecular dynamics of pMHC molecules," *Molecular Simulation*, vol. 34, no. 8, pp. 781–793, 2008.
- [52] A. V. Hill, "The possible effects of the aggregation of the molecules of haemoglobin on its dissociation curves," *Journal of Physiology*, vol. 40, supplement, pp. 4–7, 1910.
- [53] J. D. Faraldo-Gómez, L. R. Forrest, M. Baaden et al., "Conformational sampling and dynamics of membrane proteins from 10-nanosecond computer simulations," *Proteins*, vol. 57, no. 4, pp. 783–791, 2004.
- [54] J. D. Chodera, W. C. Swope, J. W. Pitera, C. Seok, and K. A. Dill, "Use of the weighted histogram analysis method for the analysis of simulated and parallel tempering simulations," *Journal of Chemical Theory and Computation*, vol. 3, no. 1, pp. 26–41, 2007.
- [55] L. J. Smith, X. Daura, and W. F. Van Gunsteren, "Assessing equilibration and convergence in biomolecular simulations," *Proteins*, vol. 48, no. 3, pp. 487–496, 2002.
- [56] B. Hess, "Convergence of sampling in protein simulations," *Physical Review E*, vol. 65, no. 3, Article ID 031910, 10 pages, 2002.

Research Article

How the Interval between Prime and Boost Injection Affects the Immune Response in a Computational Model of the Immune System

F. Castiglione,¹ F. Mantile,² P. De Berardinis,³ and A. Prisco²

¹ Institute for Computing Applications “M. Picone”, National Research Council of Italy, via dei Taurini 19, 00185 Roma, Italy

² Institute of Genetics and Biophysics “A. Buzzati Traverso”, National Research Council of Italy, via Pietro Castellino 111, 08013 Naples, Italy

³ Institute of Protein Biochemistry National Research Council of Italy, via Pietro Castellino 111, 08013 Naples, Italy

Correspondence should be addressed to F. Castiglione, f.castiglione@iac.cnr.it

Received 15 June 2012; Accepted 23 July 2012

Academic Editor: Francesco Pappalardo

Copyright © 2012 F. Castiglione et al. This is an open access article distributed under the Creative Commons Attribution License, which permits unrestricted use, distribution, and reproduction in any medium, provided the original work is properly cited.

The immune system is able to respond more vigorously to the second contact with a given antigen than to the first contact. Vaccination protocols generally include at least two doses, in order to obtain high antibody titers. We want to analyze the relation between the time elapsed from the first dose (priming) and the second dose (boost) on the antibody titers. In this paper, we couple *in vivo* experiments with computer simulations to assess the effect of delaying the second injection. We observe that an interval of several weeks between the prime and the boost is necessary to obtain optimal antibody responses.

1. Introduction

Immunological memory, defined as the capacity of the immune system to respond more vigorously to the second contact with a given antigen than to the first contact, is the basis of the persistent protection afforded by the resolution of some infections and is the goal of vaccination. Memory is a system-level property of the immune system, which arises from the increase in the frequency of antigen specific B and T cells as well as from the differentiation of antigen specific lymphocytes into memory cells, which are able to respond faster to antigen and to self-renew [1–3].

The protection afforded by vaccines currently in use correlates well with the magnitude of the antibody response. The persistence of antigen-specific antibody titers over a protective threshold and the ability to exhibit a “recall response” to encounter with antigen have long been the only measurable correlates of vaccine “take” and immune memory. However, these methods for the evaluation of immune memory suffer from the disadvantage of relying on long-term monitoring of the immune response. Thus, optimizing the vaccination schedule to obtain high and persisting

antibody titers, an important step in the development of novel vaccines and immunotherapies, is a long trial and error process [4, 5].

The magnitude of the immune response can usually be increased by multiple administrations of vaccine; the notable exception being represented by virus-vectored vaccines and whereby immunity to the viral capsid induced by the first dose prevents cell infection by subsequent doses.

When a new prototype vaccine is tested for the first time *in vivo*, the injection schedule is designed empirically, using a combination of immunological knowledge, previous experience, and practical constraints, and it is refined on the basis of the observed immunological responses and protection. However, *in vivo* experimentation poses practical limits to the number of different immunization schedules that can be tried to find the protocol that maximizes the antibody titer, while minimizing the number of doses. Thus, *in silico* simulations of the kinetics of the antibody response can be useful to generate predictions, that can then be tested experimentally, and to generate novel hypotheses on early correlates of immune memory.

The vaccine used to generate the experimental data reported in this study and described in Section 2, namely-(1-11)E2, consists of “virus-like particles” formed by a domain of the bacterial protein E2 that is able to self-assemble into a 60-mer peptide [6]. Each particle displays on its surface 60 copies of peptide “DAEFRHDSGYE,” corresponding to the first 11 N-terminal residues of beta-amyloid, a peptide that forms aggregates in the brain of Alzheimer’s disease patients.

A single “prime” dose of the (1-11)E2 vaccine induces measurable titers of anti-beta-amyloid antibodies in all treated mice, and in 4/5 mice that received a “boost” dose 6 months later, we observed a clear memory response, namely, a fast rise of anti-beta-amyloid antibody titers to a peak serum concentration between 1 and 7 mg/mL.

Studies performed in transgenic mouse models of Alzheimer’s disease have demonstrated that antibodies against beta-amyloid are able to reduce plaques and improve cognition (reviewed in [7–10]. In mouse models as well as in clinical trials in Alzheimer’s disease patients, induction of a high titer of anti-beta-amyloid antibodies correlates with the therapeutic efficacy of vaccination [10, 11].

In this study, the effect of the time delay between the first and the second injection of antigen on the peak antibody titer is explored in a computer model of the immune system response.

2. Materials and Methods

2.1. Animals. BALB/c mice were obtained from Charles River Laboratory, Italy. Ethics Committee of the institution within which the work was undertaken have approved the protocols involving mice and these conform to the provisions of the Declaration of Helsinki and Italian National Guidelines for animal use in research.

2.2. Generation of Virus-Like Particles (VLP) (1-11)E2. Synthetic complementary oligonucleotides encoding the sequence 1–11 (sequence DAEFRHDSGYE) of beta-amyloid were cloned into the pETE2DISP vector cut with NcoI and XmaI, to obtain plasmid pET(1-11)E2. Successful construction of the plasmid was confirmed by DNA sequence analysis. (1-11)E2 VLP was produced and characterized as previously described [5].

2.3. Immunizations. Mice were immunized intraperitoneally with 200 μ L of a 1 : 1 mixture of antigen and adjuvant. Complete Freund’s Adjuvant (CFA) was used in the first injection, and Incomplete Freund’s Adjuvant (IFA) in the second one. Each mouse received an amount of antigen carrying 6 μ g of the beta-amyloid epitope. Blood was collected at indicated time points, and ELISA was performed on serum.

2.4. Enzyme-Linked Immunosorbent Assay (ELISA). Wells of a 96-well Nunc Immunoplate were coated with streptavidin at 37°C over night until complete evaporation. Wells were blocked with 0.5% bovine serum albumin in 20 mM TrisHCl pH 7.3, and 120 mM NaCl, incubated with 50 ng biotinylated

peptide, incubated with mouse sera diluted in 0.25% bovine serum albumin, 20 mM TrisHCl pH 7.3, 0.5 M NaCl, 0.05% Tween 20, and detected with anti-mouse IgG peroxidase conjugate (SIGMA A-2554).

All incubations were carried out for 1 hr at 37°C, and after each step wells were washed twice with Elisa wash buffer (EWB) (20 mM TrisHCl pH 7.3, 130 mM NaCl, 0.05% Tween 20) and once with Tris buffered saline (TBS) (20 mM TrisHCl pH 7.3, 0.5 M NaCl). Wells were incubated for 45 min at room temperature with 0.4 mg mL⁻¹ O-phenylenediamine dihydrochloride dissolved in 30 mM citric acid, 70 mM Na₂HPO₄, 0.8 mM H₂O₂. Absorbance was read at 492 nm, after blocking color development was blocked with 0.8 M sulfuric acid.

Each serum was tested against synthetic peptides 1–11 of beta-amyloid (the synthetic peptide 23–29 of beta-amyloid was used as a negative control). Titer of a serum was defined as the highest dilution yielding an absorbance value equal to twofold of the background value obtained against an irrelevant antigen.

2.5. The Computational Model. The *in silico* experiments are performed by a computational model of the immune system [12] that uses binary strings to represent the *binding site* of cells and molecules (i.e., lymphocytes receptors, BCRs, TCRs, Major Histocompatibility Complexes MHC, antigen peptides and epitopes, immunocomplexes IC, etc.).

The model is based on the agent-based modeling (ABM) paradigm, in that all entities are individually represented [13, 14] as in cellular automata models [15]. It includes the major classes of cells of the lymphoid lineage, that is, T helper lymphocytes, cytotoxic T lymphocytes, B lymphocytes, antibody-producer plasma cells, and natural killer cells (NK) and some of the myeloid lineage, that is, macrophages (M ϕ) and dendritic cells (DC). These entities cooperate following a set of algorithms (or logical rules) carrying out the different phases of the immune recognition and response to a generic pathogen. In particular, the model takes into account phagocytosis, antigen presentation, cytokine release, cell activation from inactive or anergic states to active states, cytotoxicity, and antibody secretion. The model simulates a simplified form of innate immunity and a more elaborate form of adaptive immunity, including both humoral and cytotoxic immune responses [16].

In the model, a single human lymph node (or a portion of it) is mapped onto a three-dimensional ellipsoid Cartesian lattice. The primary lymphoid organs thymus and bone marrow are modeled apart: the thymus [17] is implicitly represented by the positive and negative selection of immature thymocytes before they enter into the lymphatic system, while the bone marrow generates already mature B lymphocytes. Hence, only immunocompetent lymphocytes are represented on the primary lymphoid organ modeled.

This computational model can be seen as a collection of working assumptions or theories, most of which are regarded as established immunological mechanisms. In details, the model includes: the clonal selection theory of Burnet [18]; the idiotypic network theory of Jerne [19]; the clonal deletion

TABLE 1: Biological rules coding for interactions between cells or among cells and molecules and other specific mechanisms of the immune system. Each of the entries of this list corresponds to an algorithm implementing a specific activity of the immune cells.

Interactions	Activations
B phagocytosis of antigen	Activation of Mφ
Mφ phagocytosis of antigen	B cells anergy
DC phagocytosis of antigen	TH cells anergy
B presentation to TH	Priming of TH cells
Mφ presentation to TH	TC cells anergy
DC presentation to TH	Activation of TC cells
Formation of immunocomplexes (IC)	
Mφ phagocytosis	
Infection of EP cells	
Cytotoxicity of infected cells by TC	
Antigen ingestion and presentation	Other procedures
B exogenous pathway	Clone divisions
Mφ exogenous pathway	Hematopoiesis
DC exogenous pathway	Plasma secretion of immunoglobulins
EP endogenous pathway	Entity movement
	Hypermutation of antibody

B: B cell, Mφ: macrophage, DC: dendritic cell, TC: cytotoxic CD8+ T cell, Th: CD4+ T cell.

theory (i.e., thymus education of T lymphocytes, [20]); the hypermutation of antibodies [21]; the danger theory of Matzinger [22]; the replicative senescence of T cells, or the Hayflick limit (i.e., a limit in the number of cell divisions, [23]); T-cell anergy [24]; Ag-dose-induced tolerance in B cells [25]. These features can be selectively toggled on or off, allowing for general investigations of immunological hypothesis. Moreover, other specific biological processes can be added to the model with relatively little effort. For example, customizations of the basic model have been used to simulate different phenomena ranging from viral infection (e.g., HIV, EBV [26, 27]) to type I hypersensitivity [28] and cancer [29, 30].

A simulated time step is roughly equivalent to eight hours. The interactions among the cells determine their functional behavior (Table 1). Interactions are coded as probabilistic rules defining the transition of each cell entity from one state to another. Each interaction requires the involved cellular entities to be in a specific state out of a set of possible states (e.g., naïve, active, resting, duplicating) that is dependent on the cell type. Once these conditions are fulfilled, the interaction is driven by a probability that is directly related to the effective level of binding between ligands and receptors.

Strings of 0s and 1s are used to represent specificity elements like receptors and other molecular binding specificities (see Figure 1). The length of this string is specified as a parameter ℓ . Two bit-strings complement each other (or are a perfect match) if every 0 in one corresponds to a 1 in

the other and conversely. More generally, an m -bit match is defined as a pair where exactly m bits complement each other. Therefore, in order to compute the binding probability, we first define the function $h(a, b)$ giving us the number of matching bits between two strings a and b (i.e., the Hamming distance in the space of the bit-strings). Then, we define the function $\alpha(m)$ as the affinity of an m -bit match. To ensure that perfect matches prevail over imperfect ones, we set $\alpha(\ell)$ to a high value and $\alpha(m)$ (with $m < \ell$) to lower values. To specify the vector α , one method is to specify it directly by simply listing out its components. Another method uses the additional parameter arguments \underline{m} , that is, the minimum match allowed, $\underline{a} = \alpha(\underline{m})$, that is, the minimum level of affinity, and δ_α a parameter specifying the gain in affinity proportional to a one bit more match, to calculate in the following way: (i) using the parameter \underline{m} , set $\alpha(\underline{m}) = \underline{a}$ whereas for $m < \underline{m}$ set $\alpha(m)$ to 0 (this provides a level below which binding cannot occur); (ii) the increase of strength on increasing a match by one bit is set to be the inverse of the ratio of number of clones with match $m + 1$ and m multiplied by the parameter δ_α . In formula,

$$\frac{\alpha(m+1)}{\alpha(m)} = \frac{\delta_\alpha \binom{\ell}{m}}{\binom{\ell}{m+1}}. \quad (1)$$

This allows to set the lower end value of $\alpha(m)$ and the steepness of its increase as the number of matching bits is incremented. It is usually more convenient than supplying the α vector directly. Generally, it is advisable to set \underline{m} somewhat close to ℓ bits in order to restrict the range of allowable matches to a few bits, so that the number of antibodies raised in response to a given antigen remains manageable.

Unlike the many immunological models, the present one not only simulates the cellular level of the intercellular interactions but also the intra-cellular processes of antigen uptake and presentation. Both the cytosolic and endocytic pathways are modeled. In the model, endogenous antigen is fragmented and combined with MHC class I molecules for presentation on the cell surface to CTLs receptors, whereas the exogenous antigen is degraded into smaller parts (i.e., peptides), which are then bound to MHC class II molecules for presentation to the THs receptors (Table 1). The affinity among MHC molecules and the antigen peptides is computed in a slightly different manner than those between cell receptors and antigenic epitopes. Firstly, the match is computed over half bit string; secondly, there is no minimum match. The affinity value between two half strings whose match is m , for all $m = 0, \dots, \ell/2$, is defined as

$$\beta(m) = \left(\frac{1}{2}\right)^{\ell/2-m}. \quad (2)$$

The function $\beta(m)$ represents the probability that a peptide with match m to the MHC molecule binds and is presented alongside with it on the cell surface for subsequent TCR recognition.

While macroscopic entities like cells are individually represented (i.e., they are considered as agents), low-molecular,

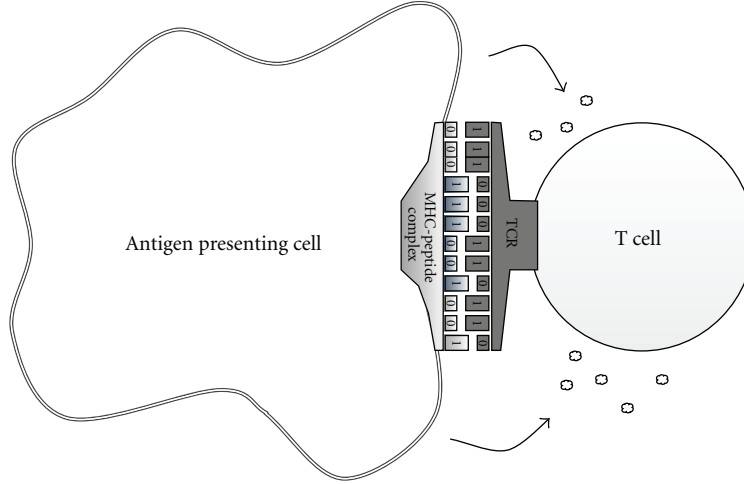


FIGURE 1: Molecular affinity is calculated on the basis of the Hamming distance of the binary strings representing the binding sites of the interacting entities. In the figure a T lymphocyte receptor binds the MHC-peptide complex of an antigen presenting cell.

weight molecules, such as interleukins or chemokines, are represented in terms of their concentration. The corresponding dynamics is modeled by the following parabolic partial differential equation that describes a uniform diffusion process with the addition of a degradation term that takes into account the finite half-life of molecules:

$$\frac{\partial c}{\partial t} = D \nabla^2 c - \lambda c + s(x, t), \quad (3)$$

where $c = c(x, t)$ is the concentration of chemokines, $s(x, t)$ is the source term, D is the diffusion coefficient, and $\lambda = \ln 2/\tau$ where τ is the half-life. We assume $D = 3000 \mu\text{m}^2/\text{min}$ and $\tau = 3 \text{ hrs}$ for all chemokines [31, 32]. Differences in cell mobility also are taken into account. TH cells are the fastest with an average velocity of $11 \mu\text{m}/\text{min}$, followed by B cells with $6 \mu\text{m}/\text{min}$ and DC with a velocity of $3 \mu\text{m}/\text{min}$ [32].

The rules listed in Table 1 are executed for each time step. The stochastic execution of these rules, as in a Monte Carlo methods, produces a logical causal/effect sequence of events culminating in the immune response and development of immunological memory. The starting point of this series of events is the injection of antigen (the priming).

The system is designed to maintain a steady state of the global population of cells (*homeostasis*) if no infection is applied. This is achieved by modeling the birth/death process as a mean reverting process of the type:

$$\frac{dx_i(t)}{dt} = \frac{\log_2}{\tau_i} (x_i(0) - x_i(t)) + \sigma(t), \quad (4)$$

where $x_i(t)$ is the population i at time t , τ_i is the specific half-life parameter, and $\sigma(t)$ is a Gaussian random noise.

Initially the system is naïve in the sense that there are neither T and B memory cells nor plasma cells and antibodies. The various steps of the simulated immune response depends on what is actually injected, for example, a recombinant virus or bacteria.

The model contains a number of parameters whose value has been determined as follows. These parameters

can be classified into three categories: (i) unknown values or free parameters, which are set after a tuning procedure that begins with an initial estimation of their values and iteratively improves the results of the simulations by small modifications of the parameters; (ii) parameters that correspond to the initial conditions of the system and that determine the problem under investigation; (iii) parameters whose value is well known and available from immunology literature.

Given the initial condition represented by the simulated volume determining the number of cells populating the space according to known leukocyte formulas, the model runs in a metastable state assured by homeostasis. In absence of antigenic stimulus, the populations of immune cells randomly fluctuates around the average values given. Upon an antigenic challenge performed by injecting a certain amount of a pathogen, the system moves away from the metastable state to recognize the insulting molecules and to mount an immune response that may or not include the deployment of both the humoral and the cytotoxic artillery. Once the antigen is cleared, the system goes back to an equilibrium state that is not the same as before as it contains a shift in the system specificity amounting to the immune memory. This memory allows for a faster and stronger reaction to a later encounter of the same (or similar) pathogen.

Figure 2 shows this dynamics as an example of a typical immunization experiment consisting in injecting at day zero and about ten weeks after a generic immunogenic substance as a vaccine. The result of the priming is that the antigen is cleared in about four days (panel up-left) as the antibodies elicited peak within the second and the third week (bottom-left panel). The different specificities (i.e., binary strings) of the antibodies elicited are shown in the same figure. The figure also shows the corresponding antibody-producing plasma cells (bottom-right panel) and the immunocomplexes titer (up-right panel) consisting of antigen clotted with antibodies.

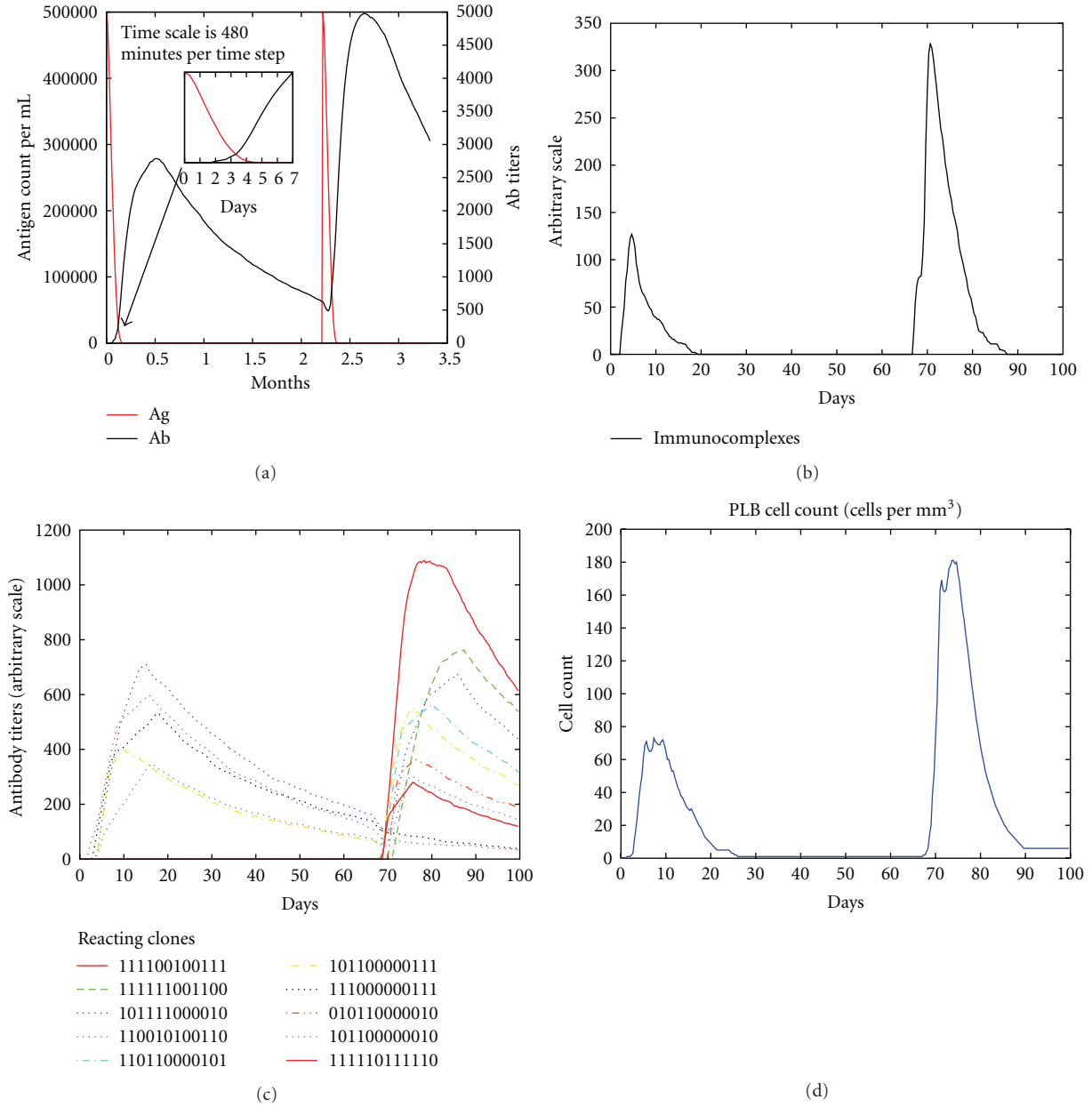


FIGURE 2: The virtual experiments are conducted priming at day zero and later after a certain time interval. In this case the boost has been performed after about ten weeks. While the antibodies are produced by plasma cells derived by expanding clones of B cells, the injected antigen is cleared and immunocomplexes are formed. The secondary immune response to the boost is stronger and faster than the response to the priming because of the immunological memory (not shown).

Whereas the immunogenicity of the injected substance is the main responsible for the immune response, a secondary but not less important factor is the timing. Indeed, as anticipated above, the question investigated here is what is the optimal timing for boosting in terms of higher antibody titers. Intuitively, one expects a window of optimality since a too close boost does not elicit a strong memory as it simply add, (and compete for resources) to the prime, whereas an overly delayed boost may fail to wake up the memory simply because it already faded away. Computer simulations allow to easily broadening the search for the optimality,

something that would be costly and time consuming with animal models.

3. Validating the Model against the Experimental Dataset

Before use, the simulator needs to be validated against the specific experimental data available and described in Section 2. Interestingly, matching experimental data was not straightforward. Indeed, the first set of simulations did not

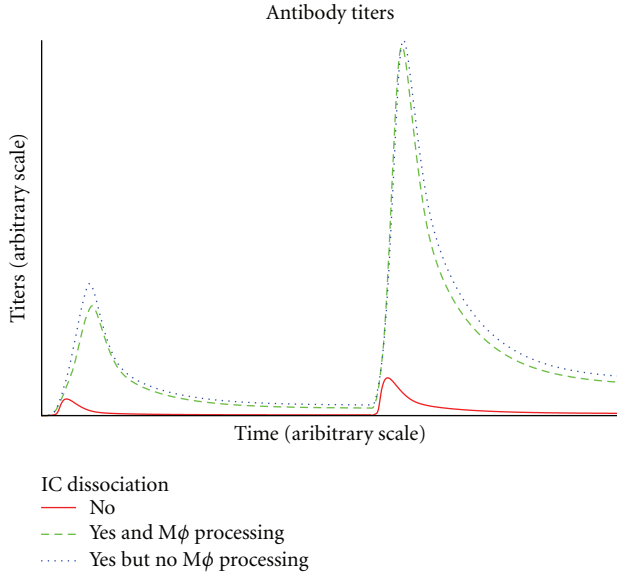


FIGURE 3: Dissociation of immunocomplexes and successive phagocytosis and presentation by APCs of the antigenic molecules increases vaccine persistence hence increasing the magnitude of the immune response.

yield reasonable fit with the data indicating that the model was lacking of some specific mechanism.

In particular, the model failed to reproduce a correct kinetic for both antigen clearance and antibody expansion (it goes without saying that the two issues are connected) as we obtained faster than experimentally observed rates. Discussions pointed us to identify a mechanism of vaccine delivery that was missing in the computational model and could account for the divergence observed. Therefore, in order to correct this inconsistency, we implemented two mechanism: (i) one to implement what is called the “depot effect,” that is, the gradual release of the vaccine so as to cover a long period of antigen exposure, and (ii) a mechanism accounting for immunocomplexes dissociation actually providing a further longer exposition time to the injected vaccine.

The modified model incorporating these two effects effectively increased the targeted adherence to the experimental data. Since the depot effect resulted in a minor difference, we show hereafter the effects of implementing the dissociation of immunocomplexes on the simulation outcome. Note that the overall expected effect of the antigen-antibody compound dissociation is to have a longer exposition to the antigen and also a better affinity maturation since weak binders have a higher dissociation rate. Specifically, the instability of immunocomplexes (ICs) favors re-ingestion of the immunogenic peptides by antigen presenting cells (APCs) and representation to specific lymphocytes, who, on their side, opt for higher affinity ones. See Figure 3 to compare the antibodies responses in three different cases: without IC dissociation, with IC dissociation but no direct ingestion and following presentation of IC by macrophages and with both IC dissociation but no competing mechanism

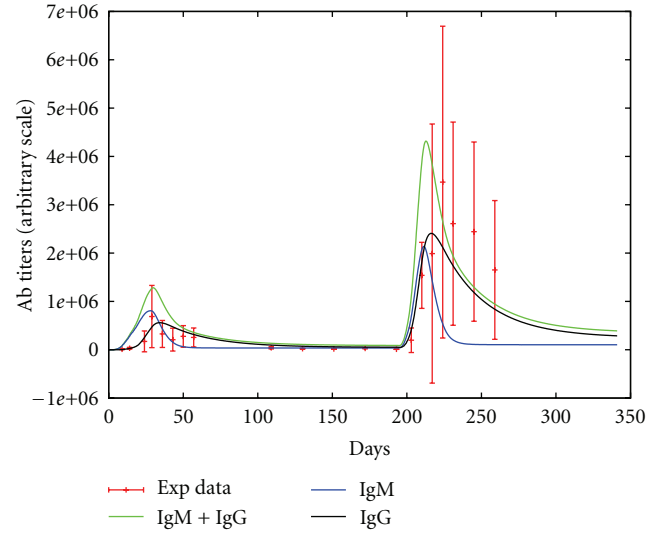


FIGURE 4: Comparison with mice data: antibody (IgG) titers as average of four mice experiments with relative standard deviation. Mice received a prime injection at day 0 and a boost six months later.

of IC elimination by macrophages. We can see that without IC dissociation, the antibody titers are low compared to the case of higher antigen-antibody instability whereas the effect of a direct ingestion and following presentation of IC by macrophages does not account for the same big effect but nevertheless shows that IC ingestion by $M\phi$ actually represents a suboptimal situation compared to the “neat” IC dissociation because of the waste of antibodies bound to the antigen in the complexes that are effectively thrown away by macrophages upon ingestion.

After these modifications the simulator showed titers that are comparable to that observed in real data. Figure 4 show the fit with mice data calculated as average of four mice experiments. Error bars show the standard deviation of IgG antibodies receiving a vaccine priming at day zero and a boost six months later. The solid line in Figure 3 show a good agreement of the simulated mice with the experimental data.

This data set allowed to fine tune the parameters of the simulator. Further experiments have been performed afterwards to investigate the relationships among the prime-boost time distance and the magnitude of the immune response measured as IgG antibody titers. This is show in the next section.

4. Results

In order to investigate the relationship between the interdose delay and the immune response, we have performed a set of virtual experiments by running the simulation with different initial conditions. In particular, we injected the antigen at time step $t_1 = 0$ and successively at t_2 . We performed simulations for T time steps, corresponding to about $T/3$

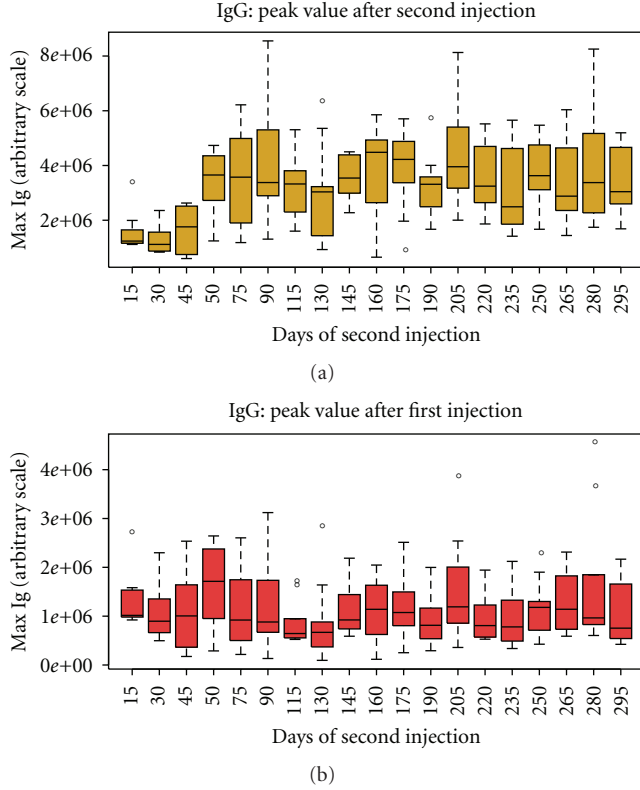


FIGURE 5: The lower panel shows that m_1 is trivially independent of t_2 whereas the upper panel showing m_2 tells that, overall, there exists an optimal timing for the boost that is greater than 45 days.

days of real life. The delay $\delta_t = t_2 - t_1$ is the free variable of the experiment, whereas the outcome is the differences in the amount of antibodies produced to the prime and the boost vaccination. More specifically, we call $ab(t)$ the antibody titers at time t , $m_1 = \max\{ab(t) : t \in [t_1, t_2]\}$ the maximum level of ab relative to the injection of antigens at time t_0 (i.e., the prime injection), and analogously $m_2 = \max\{ab(t) : t \in [t_2, T]\}$ the maximum level of IgG antibodies relative to the injection of antigens at time t_2 (i.e., the boost injection). We can assume that $m_1 \leq m_2$ since the injected antigen is the same for the two injections and, therefore, the immune memory is such that the second immune response is faster and stronger than the first [33, 34].

We call $\Delta_{ab} = m_2 - m_1$ the differences in the peak values of antibody titers during the two responses. Since t_1 is fixed, $t_1 = 0$ and m_1 and m_2 both depend on the time of the second injection t_2 , we have that $\delta_t = t_2$, $m_2 \equiv m_2(t_2)$ and $\Delta_{ab} \equiv \Delta_{ab}(t_2)$.

In Figure 5, we show a boxplot to compare $m_1(0)$ and $m_2(t_2)$ for different values of $\delta_t = t_2$. This has been computed averaging over 20 simulations of 10 micro liters of volume. The lower panel of that figure shows that, apart from large stochastic fluctuation, $m_1(t_2) = \text{const}$, that is, it is independent of t_2 , whereas the upper panel showing $m_2(t_2)$ tells that, overall, there exists an optimal timing for the boost that is greater than 45 days.

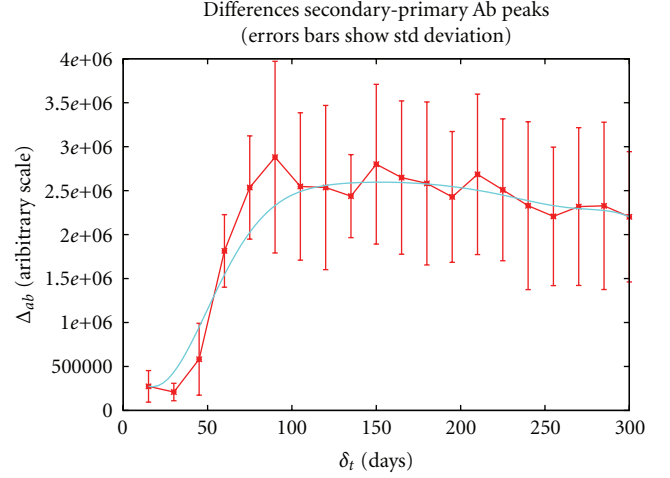


FIGURE 6: When the boost is given in the first month after the prime, our measure of the efficiency of the boost, $\Delta_{ab}(\delta_t)$, is quite low whereas it increases when the second dose is given 45 to 90 days after the prime.

The same information is better displayed in Figure 6 that plots $\Delta_{ab}(\delta_t)$ as a function of $\delta_t = t_2$. In particular, an interval of several weeks between the prime and the boost is necessary to obtain an optimal humoral response, as hypothesized and reported in experimental studies. Indeed, when the boost is given in the first month after the prime, the difference between the peaks of the secondary and primary responses, that is a measure of the efficiency of the boost, is quite low. The boost efficiency increases when the second dose is given 45 to 90 days after the prime, whereas further delaying the boost does not improve the secondary antibody peak.

5. Discussion

Optimizing prime-boost regimens is key to developing novel vaccines. What is the optimal time for boosting is a fundamental question that remains unanswered [4]. It has been suggested that an interval of at least 2-3 months between the prime and the boost is necessary to obtain optimal responses, as memory T cells with high proliferative potential do not form until several weeks after the first immunization, and memory B cells have to go through the germinal center reaction and take several months to develop [4].

Immunization schedules are designed empirically and are then refined on the basis of the observed immunological responses and protection. In some instances, different countries that implement the same vaccine in their national immunization programs use different schedules [35, 36].

The United States Advisory Committee on Immunization Practices (ACIP) publishes each year a recommended immunization schedules for licensed vaccines, to reflect current recommendations [37, 38]. For individuals whose vaccinations have been delayed, catch up schedules and minimum intervals between doses are indicated [37]. For most vaccines currently in use, the minimum recommended

interval between dose 1 and dose 2, for children, is 4 weeks, however, for some vaccines a minimum interval of 8 weeks, 3 months, or 6 months is recommended [37].

In preclinical experimentation of prototype vaccines, on the other hand, shorter intervals between doses are often used, to obtain a rapid rise in antibody titers above protective values. In the case of vaccination against beta-amyloid in mouse models of Alzheimer's disease, a schedule that has been used with a variety of prototype vaccines involves doses at day 0, 2 weeks and 4 weeks, and monthly doses thereafter. When multiple doses are administered within a short timeframe, understanding the contribution of each dose to the peak antibody titer can be practically impossible.

In this study we have analyzed the effect of the interval between prime and boost injection on the antibody response in a computational model of the immune system.

We have shown that in the computational model an interval of several weeks between the prime and the boost is necessary to obtain optimal responses, as hypothesized and reported for real immune responses. In particular, in the simulations, when the boost is given in the first month after the prime, the difference between the peaks of the secondary and primary responses, our measure of the efficiency of the boost, is low. The boost efficiency increases when the second dose is given 45 to 90 days after the prime, whereas further delaying the boost does not improve the secondary antibody peak (simulations of boosts administered up to 300 days after the prime are shown in Figure 6).

Thus, the computational model displays the qualitative features of real immune responses, and it can be useful to understand which component of the immune system is in charge for the time-dependent differences in boost efficacy that are observed *in vivo*. Interestingly, the efficacy of the boost does not parallel the number of T helper cells and B cells. In the model, the number of T and B cells increases after the prime, as cells are activated and duplicate. Cell numbers then decline, as a consequence of cell death. Thus, at day 15 there are more T or B cells than at day 90. Interestingly, also memory T cells are more abundant at the 15 and 45 time point than at later time points, revealing that the better memory response obtained at later time points is not correlated to higher numbers of memory T cell. On the contrary, the boost is optimal at a time point when the populations generated by the prime, in particular, activated cells, duplicating cells, and also memory cells, have all contracted. The T and B cells that are present in the system at late time points after the prime are qualitatively different from earlier cells. It is important here to emphasize that, in the model, a memory cell is a cell that, having been activated by antigen, has increased its average lifespan. Further encounters with antigen lead to further increases in the lifespan. Thus, memory cells are not all equal in their proliferative potential, and the memory of the system matures over time, as cells with high proliferative capacity are generated. This model, therefore, demonstrates that cell populations dynamics, and a simple assumption, namely the fact that a "survival signal" is received by memory cells at each encounter with antigen, are sufficient to reproduce the need for an optimal delay between prime and boost, observed *in vivo*.

On the other hand, different vaccines are known to have different requirements with respect to the minimum interval between doses. The simulations reported in this study refer to a "generic vaccine," and the time scales that were obtained, which are quite realistic, anyway do not refer to a specific vaccine, although parameters have been set to fit data obtained with a nonreplicating protein antigen, namely, virus-like particle (1-11)E2 (6). The computational model can be useful to explore the role of different features of the primary response on the optimal time point for boost, and on boost efficiency, at a set time point.

A deeper analysis of the overall system dynamics is currently underway to pinpoint which immune component is in charge for the observed behavior and will be published in due course. Furthermore, vaccine specificities like the number of peptides are likely to play a distinct role the quest optimality and therefore they have to be incorporated in the computer model as well.

Author's Contribution

P. De Berardinis and A. Prisco equally contributed to this study.

Acknowledgments

A. Prisco acknowledges support from FIRB-Merit RBNE08LN4P_002. P. De Berardinis acknowledges support from Grant MIUR-PON01_00117.

References

- [1] L. J. McHeyzer-Williams and M. G. McHeyzer-Williams, "Antigen-specific memory B cell development," *Annual Review of Immunology*, vol. 23, pp. 487–513, 2005.
- [2] T. Yoshida, H. Mei, T. Dörner et al., "Memory B and memory plasma cells," *Immunological Reviews*, vol. 237, no. 1, pp. 117–139, 2010.
- [3] R. A. Seder, P. A. Darrah, and M. Roederer, "T-cell quality in memory and protection: implications for vaccine design," *Nature Reviews Immunology*, vol. 8, no. 4, pp. 247–258, 2008.
- [4] F. Sallusto, A. Lanzavecchia, K. Araki, and R. Ahmed, "From vaccines to memory and back," *Immunity*, vol. 33, no. 4, pp. 451–463, 2010.
- [5] A. Prisco and P. De Berardinis, "Memory immune response: a major challenge in vaccination," *BioMolecular Concepts*, In press.
- [6] F. Mantile, C. Basile, V. Cicatiello et al., "A multimeric immunogen for the induction of immune memory to beta-amyloid," *Immunology and Cell Biology*, vol. 89, no. 5, pp. 604–609, 2011.
- [7] C. A. Lemere and E. Masliah, "Can Alzheimer disease be prevented by amyloid- β immunotherapy?" *Nature Reviews Neurology*, vol. 6, no. 2, pp. 108–119, 2010.
- [8] D. L. Brody and D. M. Holtzman, "Active and passive immunotherapy for neurodegenerative disorders," *Annual Review of Neuroscience*, vol. 31, pp. 175–193, 2008.
- [9] H. L. Weiner and D. Frenkel, "Immunology and immunotherapy of Alzheimer's disease," *Nature Reviews Immunology*, vol. 6, no. 5, pp. 404–416, 2006.

- [10] M. Esposito, I. Luccarini, V. Cicatiello et al., “Immunogenicity and therapeutic efficacy of phage-displayed beta-amyloid epitopes,” *Molecular Immunology*, vol. 45, no. 4, pp. 1056–1062, 2008.
- [11] C. Holmes, D. Boche, D. Wilkinson et al., “Long-term effects of A β 42 immunisation in Alzheimer’s disease: follow-up of a randomised, placebo-controlled phase I trial,” *The Lancet*, vol. 372, no. 9634, pp. 216–223, 2008.
- [12] M. Bernaschi and F. Castiglione, “Design and implementation of an immune system simulator,” *Computers in Biology and Medicine*, vol. 31, no. 5, pp. 303–331, 2001.
- [13] F. Castiglione, “Agent based modeling,” *Scholarpedia*, vol. 1, no. 10, p. 1562, 2006.
- [14] F. Castiglione, “Introduction to agent-based modeling and simulation,” in *Encyclopedia of Complexity and Systems Science*, R. Meyers, Ed., vol. 1, pp. 197–200, Springer, New York, NY, USA, 2009.
- [15] S. Wolfram, *A New Kind of Science*, Wolfram Media, Champaign, Ill, USA, 2002.
- [16] F. Castiglione, B. Ribba, and O. Brass, “Comparing in-silico results to in vivo and ex-vivo of influenza-specific immune responses after vaccination or infection in humans,” in *Innovation in Vaccinology, from Design, through to Delivery and Testing*, S. Baschieri, Ed., Springer, New York, NY, USA, 2012.
- [17] F. Castiglione, D. Santoni, and N. Rapin, “CTLs’ repertoire shaping in the thymus: a Monte Carlo simulation,” *Autoimmunity*, vol. 44, no. 4, pp. 261–270, 2011.
- [18] F. M. Burnet, *The Clonal Selection Theory of Acquired Immunity*, Vanderbilt University, Nashville, Tenn, USA, 1959.
- [19] N. K. Jerne, “Towards a network theory of the immune system,” *Annual Review of Immunology*, vol. 125, no. 1-2, pp. 373–389, 1974.
- [20] J. Lederberg, “Genes and antibodies,” *Science*, vol. 129, no. 3364, pp. 1649–1653, 1959.
- [21] S. Brenner and C. Milstein, “Origin of antibody variation,” *Nature*, vol. 211, no. 5046, pp. 242–243, 1966.
- [22] P. Matzinger, “Tolerance, danger, and the extended family,” *Annual Review of Immunology*, vol. 12, pp. 991–1045, 1994.
- [23] L. Hayflick and P. S. Moorhead, “The serial cultivation of human diploid cell strains,” *Experimental Cell Research*, vol. 25, no. 3, pp. 585–621, 1961.
- [24] R. H. Schwartz, “T cell anergy,” *Annual Review of Immunology*, vol. 21, pp. 305–334, 2003.
- [25] G. J. V. Nossal and B. L. Pike, “Clonal anergy: persistence in tolerant mice of antigen-binding B lymphocytes incapable of responding to antigen or mitogen,” *Proceedings of the National Academy of Sciences of the United States of America*, vol. 77, no. 3, pp. 1602–1606, 1980.
- [26] F. Castiglione, F. Poccia, G. D’Offizi, and M. Bernaschi, “Mutation, fitness, viral diversity, and predictive markers of disease progression in a computational model of HIV type 1 infection,” *AIDS Research and Human Retroviruses*, vol. 20, no. 12, pp. 1314–1323, 2004.
- [27] F. Castiglione, K. Duca, A. Jarrah, R. Laubenbacher, D. Hochberg, and D. Thorley-Lawson, “Simulating Epstein-Barr virus infection with C-ImmSim,” *Bioinformatics*, vol. 23, no. 11, pp. 1371–1377, 2007.
- [28] D. Santoni, M. Pedicini, and F. Castiglione, “Implementation of a regulatory gene network to simulate the TH1/2 differentiation in an agent-based model of hypersensitivity reactions,” *Bioinformatics*, vol. 24, no. 11, pp. 1374–1380, 2008.
- [29] F. Pappalardo, M. D. Halling-Brown, N. Rapin et al., “ImmunoGrid, an integrative environment for large-scale simulation of the immune system for vaccine discovery, design and optimization,” *Briefings in Bioinformatics*, vol. 10, no. 3, pp. 330–340, 2009.
- [30] A. Palladini, G. Nicoletti, F. Pappalardo et al., “In silico modeling and in vivo efficacy of cancer-preventive vaccinations,” *Cancer Research*, vol. 70, no. 20, pp. 7755–7763, 2010.
- [31] K. Francis and B. O. Palsson, “Effective intercellular communication distances are determined by the relative time constants for cyto/chemokine secretion and diffusion,” *Proceedings of the National Academy of Sciences of the United States of America*, vol. 94, no. 23, pp. 12258–12262, 1997.
- [32] J. L. Segovia-Juarez, S. Ganguli, and D. Kirschner, “Identifying control mechanisms of granuloma formation during *M. tuberculosis* infection using an agent-based model,” *Journal of Theoretical Biology*, vol. 231, no. 3, pp. 357–376, 2004.
- [33] R. A. Goldsby, T. J. Kindt, and B. A. Osborne, *Kuby Immunology*, W.H. Freeman, New York, NY, USA, 4th edition, 2000.
- [34] K. Murphy, P. Travers, C. Janeway, and M. Walport, *Janeway’s Immunology*, Garland Science, Taylor and Francis, New York, NY, USA, 2008.
- [35] P. Kaaijk, A. van der Ende, G. Berbers, G. P. van den Dobbelsteen, and N. Y. Rots, “Is a single dose of meningococcal serogroup C conjugate vaccine sufficient for protection? Experience from the Netherlands,” *BMC Infectious Diseases*, vol. 12, article 35, 2012.
- [36] R. Verma, P. Khanna, M. Bairwa, S. Chawla, S. Prinja, and M. Rajput, “Introduction of a second dose of measles in national immunization program in India: a major step towards eradication,” *Human Vaccines*, vol. 7, no. 10, pp. 1109–1111, 2011.
- [37] Centers for Disease Control and Prevention, “Recommended immunization schedules for persons aged 0 through 18 years—United States, 2012,” *Morbidity and Mortality Weekly Report*, vol. 61, no. 5, pp. 1–4, 2012.
- [38] J. Midwifery, “Recommended adult immunization schedule&United States, 2012,” *Centers For Disease Control and Prevention. Womens Health*, vol. 57, no. 2, pp. 188–195, 2012.

Review Article

Understanding Immunology via Engineering Design: The Role of Mathematical Prototyping

David J. Klinke II^{1,2} and Qing Wang³

¹Department of Chemical Engineering and Mary Babb Randolph Cancer Center, West Virginia University, Morgantown, WV 25606, USA

²Department of Microbiology, Immunology and Cell Biology, West Virginia University, Morgantown, WV 25606, USA

³Department of Computer Sciences, Mathematics, and Engineering, Shepherd University, Shepherdstown, WV 25433, USA

Correspondence should be addressed to David J. Klinke II, david.klinke@mail.wvu.edu

Received 15 June 2012; Accepted 2 August 2012

Academic Editor: Francesco Pappalardo

Copyright © 2012 D. J. Klinke II and Q. Wang. This is an open access article distributed under the Creative Commons Attribution License, which permits unrestricted use, distribution, and reproduction in any medium, provided the original work is properly cited.

A major challenge in immunology is how to translate data into knowledge given the inherent complexity and dynamics of human physiology. Both the physiology and engineering communities have rich histories in applying computational approaches to translate data obtained from complex systems into knowledge of system behavior. However, there are some differences in how disciplines approach problems. By referring to mathematical models as mathematical prototypes, we aim to highlight aspects related to the process (i.e., prototyping) rather than the product (i.e., the model). The objective of this paper is to review how two related engineering concepts, specifically prototyping and “fitness for use,” can be applied to overcome the pressing challenge in translating data into improved knowledge of basic immunology that can be used to improve therapies for disease. These concepts are illustrated using two immunology-related examples. The prototypes presented focus on the beta cell mass at the onset of type 1 diabetes and the dynamics of dendritic cells in the lung. This paper is intended to illustrate some of the nuances associated with applying mathematical modeling to improve understanding of the dynamics of disease progression in humans.

1. Introduction

One of the great challenges in the field of health science is understanding how to integrate the knowledge obtained about individual molecules and cells to predict integrated system behavior [1]. Advances in the techniques associated with molecular biology during the twentieth century provided immense insight into the individual components of complex biological systems. Integration of this new technology has also changed the nature of immunological research—from static single measurements to large-scale data-intensive assays obtained at multiple time points. As highlighted in Figure 1, research costs associated with these new techniques have escalated dramatically, but the commercialization rate of new therapeutic products has been unable to keep pace [2]. This increasing disconnect between

cost and commercialization also corresponds to a growing awareness of the need to improve understanding of how the identified biological parts function together in biological systems and how dysfunction manifests itself as disease [3, 4].

Historically, engineering is an applied field in which knowledge of how components of a system work, which is obtained through basic research, is synthesized into commercially viable products and processes. A fundamental pillar in this field is the use of computational frameworks for interpreting and predicting the behavior of complex systems [6]. These computational frameworks integrate fragmented knowledge and enable one to explore novel experimental conditions, as a type of *in silico* screening. By recreating a real system *in silico*, the predictive power of the simulation (or lack thereof) may be used to infer hidden components or unknown relationships among existing ones. Engineering

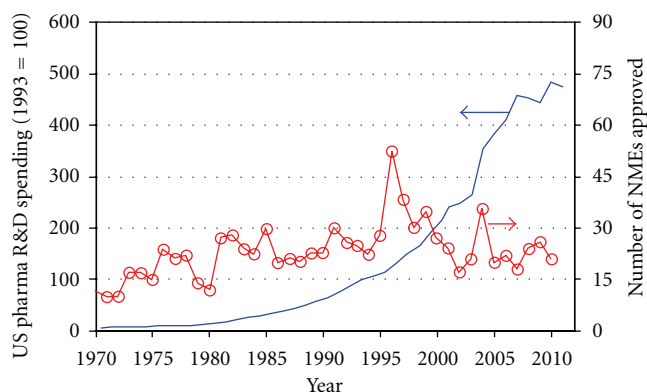


FIGURE 1: Productivity metrics of the United States pharmaceutical industry. Research and development spending by the United States pharmaceutical industry has escalated dramatically during the last several decades (solid line—left axis) [5]. However, the translation of this increased research spending into new therapeutic products, as represented by the number of new medical entities (NMEs) approved by the Food and Drug Administration (circles—right axis), has failed to keep pace [2].

can provide value to the drug development process by translating observations of the state of a system, that is, experimental data, into quantitative knowledge about how biological systems work. In particular, this approach can aid in understanding the implications of dynamic relationship among biological components of a system and can identify knowledge gaps in the collective understanding of a biological system.

Interestingly, parallels can be drawn between the development of the modern experimental techniques of molecular biology and the advances in experimental chemistry during the middle part of the 20th century. These advances in experimental chemistry were critical driving forces for the emergence of modern chemical engineering [7]. During this period, modern chemical engineering played a central role in developing computational tools that helped transform chemistry from a qualitative into a predictive science. More recently, chemical engineering is evolving to incorporate molecular biology as another enabling science, in addition to physics and chemistry [8]. Our increased ability to probe the molecular basis for cellular response provides an intriguing context for applying engineering principles, such as thermodynamics, transport phenomena, chemical kinetics, and multiscale analysis. From the biology perspective, the National Research Council in the United States identified a need for deeper integration of theory into biological research [9]. All immunologists, to some extent, act as theorists in designing and interpreting experiments. However in this context, theory is encoded in a computable form that facilitates quantitative validation of the theory against data. In fact, mathematical approaches have a rich history in physiology (e.g., [10]). Computational frameworks are also used quite extensively in engineering for interpreting and predicting the behavior of complex systems [6]. However, there are some nuances associated with mathematical modeling within the context of the engineering discipline that may

be helpful outside of the discipline. One of the challenges facing the integration of engineering approaches into the drug development process is that there is little understanding of what engineers actually do [11]. To help bridge that gap, the objective of this paper is to review how two related concepts in engineering, namely prototyping and “fitness for use”, are applied to improve understanding of immunology in the context of human physiology.

2. What Are Prototyping and “Fitness for Use”?

Engineers synthesize scientific and mathematical knowledge to solve problems using an iterative process called engineering design. A traditional application of engineering design includes developing a physical representation of the solution in the form of a prototype, such as a scale-model of an aircraft for use in a wind tunnel (see Figure 2). However, our knowledge of the system of interest is invariably uncertain. Uncertainties create options in the design process that one must select among. Prototypes developed at intermediate stages during the design process can represent alternative solutions and thereby provide a mechanism for making informed decisions. Informed decisions during the design process guide researchers iteratively towards a global solution to all of the design objectives. Collectively, the engineering design process is a knowledge generating activity [12]. Thus, these prototypes provide an essential role by improving the understanding of the problem, by identifying gaps in knowledge (i.e., uncertainties), by soliciting feedback from end users, and by providing a mechanism to evaluate the fitness of the solution against design objectives [13]. It is this last role that relates to the term “fitness for use.” Fitness for use is used to characterize how well an object fulfills its intended purpose, no more or no less [14]. Details that have no influence on fitness of the solution can be removed from consideration. Conversely, clarity about the intended purpose is required prior to creating a prototype. It is this iterative back and forth between clarifying the purpose and creating the prototype that enables reaching an optimal succinct solution.

Prototypes can also include nonphysical objects, such as a mathematical model. A mathematical model is a complete and consistent set of mathematical equations that describe the behavior of the system of interest [15]. The equations represent an explicit external description of a mental solution to the problem of synthesizing new knowledge from inspecting data. The process of constructing a mathematical model forces the researcher to wrestle with these same engineering design concepts (e.g., problem definition, uncertainties, feedback, and fitness). Mathematical models can be particularly valuable in drug discovery by improving the understanding of the problem and by identifying uncertainties in domain knowledge relevant to the target of interest. How uncertainties influence the ability of a prototype to achieve the design objectives can be quantified using well-defined techniques, such as sensitivity analysis [16] or empirical Bayesian approaches for model-based inference [17].



FIGURE 2: A common example of a prototype. A prototype of a blended wing body aircraft, the X-48B, is shown in a wind tunnel at NASA's research center in Langley Air Force Base, VA. The wind tunnel was used by researchers to evaluate this prototype against structural, aerodynamic, and operational design objectives for an advanced aircraft concept (NASA photo/Jeff Caplan).

Interdisciplinary work can also be facilitated by using “boundary” objects that reside between two different cultures [18], such as engineering and health science. A mathematical model, as a type of boundary object, imposes formalism by requiring an explicit account of the interacting elements and their relationships. In addition, boundary objects facilitate common understanding through debate and building consensus with regard to what should be included or excluded from the model. By explicitly representing knowledge associated with different scientific domains, the process of modeling can also help improve problem definition.

In essence, the primary goal of making a mathematical model is to make predictions: what do we expect to happen in a particular interacting system under particular conditions, given our current understanding of interactions among components of the system? Similarities between the simulated behaviors and observed data confirm our explicit statements while differences highlight areas of uncertainty in our understanding and provide the engine for scientific progress [19]. By referring to mathematical models as mathematical prototypes, it is the process that one uses to generate the model (i.e., prototyping) that we are intending to highlight rather than the product (i.e., a mathematical model). In the following sections, two examples are presented where a mathematical prototype that was created to address questions related to type 1 diabetes and the role of dendritic cells in adaptive immunity.

3. Example 1: Beta Cell Mass and Onset of Type 1 Diabetes

Type 1 diabetes mellitus is characterized by an impaired ability to produce insulin due to the progressive and selective destruction of beta cells in the pancreatic islets of Langerhans by the immune system [20]. A reduction in endogenous insulin production results in an increase in plasma glucose (hyperglycemia). Chronic hyperglycemia exposes patients

with type 1 diabetes to an increased risk for death if left untreated. Pathogenesis of the disease has been attributed to a variety of environmental and genetic risk factors [21]. Yet, two of the most significant challenges facing the clinical management of this disease is the increase in incidence of type 1 diabetes mellitus across the globe [22] and the lack of a cure.

One of the persistent challenges with understanding the etiology of type 1 diabetes mellitus is the inability to observe directly the events in the human pancreas that lead to the onset of hyperglycemia. It is clear that a reduction in endogenous insulin production precipitates the onset of hyperglycemia. It is common wisdom that the onset of hyperglycemia occurs when 80–95% of an individual's beta cells are destroyed [23, 24]. However, this wisdom is based largely on a small number of biopsy studies from individuals with recent disease onset who died soon after diabetes onset (e.g., [25–27]). One might infer from this common wisdom that the ability to enhance beta cell function or preserve the remaining beta cells would have a limited therapeutic potential [28]. As a result, the research effort has focused on developing prognostic tools for identifying individual, who will develop type 1 diabetes, prior to onset. Given the clinical importance of this question, the objective of a recent study [29] was to develop a mathematical model to test the conceptual model for the pathophysiology of type 1 diabetes mellitus against the histopathological evidence.

A meta-analysis was used to extract and assess the significance of embedded trends within these landmark studies. The data reported in these landmark studies provide measurements of the remaining beta cells (i.e., beta cell mass) at the time of death. Patients included in these studies died between 0 and 69 months following diagnosis. While beta cell mass or endogenous insulin production is not measured directly following onset, C-peptide is used as a surrogate measure of endogenous insulin production [30–32]. The measurement of C-peptide in a cohort of patients with type 1 diabetes has been shown to vary nonlinearly with time following onset. In the years subsequent to onset of type 1 diabetes, the beta cell mass slowly declines until there is no endogenous insulin production. Therefore, inferring the beta cell mass at onset must control for this variability in the time of beta cell mass measurement. In this new analysis, the length of time following diagnosis was controlled by limiting the analysis to a subset of patients who died within three weeks following diagnosis. As shown in Figure 3, a linear regression of this subset of recent onset patients (dotted line) revealed that the percent reduction in beta cell mass at onset is not fixed but varies with age. This trend is significant ($P < 0.01$) and suggests that, in a 20-year old individual, as little as a 40% reduction in beta cell mass is sufficient to precipitate clinical symptoms of type 1 diabetes. As this trend is at odds with the existing model for the natural history of the disease [21], a mathematical model was created to explain this behavior [29].

The mathematical model was based on the observation that the growth of the human body is a dynamic nonlinear process where different parts of the body grow at different rates. Of particular relevance to type 1 diabetes mellitus,

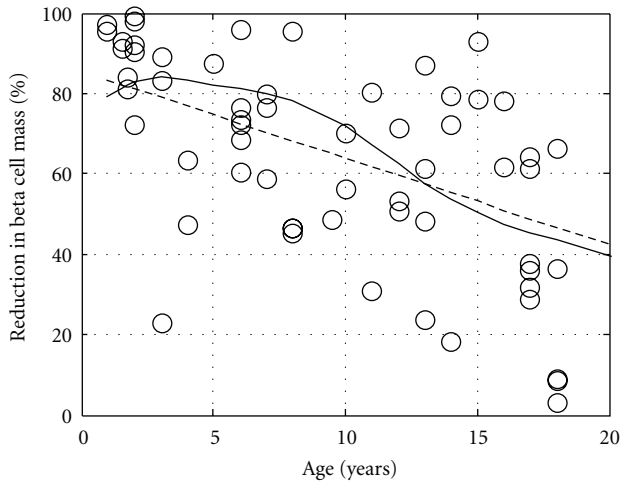


FIGURE 3: Comparison between the predicted and measured excess beta cell mass. Comparison of the excess beta cell mass predicted by the mathematical model (solid curve) compared against the trendline obtained by linear regression (dotted line) for the measured reduction in beta cell mass in 63 patients that died within three weeks of diagnosis of type 1 diabetes mellitus. Figure was originally published in [29].

body weight changes [33] at a different rate than beta cell mass [27]. One possible explanation for this observed trend in extent of reduction in beta cell mass at onset could be attributed to the dynamic imbalance between the number of beta cells and the insulin requirements for a growing body.

A mathematical model was used to predict the “excess” beta cell mass (EBCM) as a function of age by capturing the dynamic balance between changes in body weight and beta cell mass. The “excess” beta cell mass corresponds to the reduction in beta cell mass that is required before hyperglycemia occurs and is directly related to the measurements obtained in these landmark studies. This model, shown schematically in Figure 4, is derived from a mass balance on insulin and has a single adjustable parameter. Applying a mass balance to a system of interest is a common theme woven throughout the chemical engineering curriculum. In this instance, the rate of change in insulin is equal to the source of insulin, which is proportional to beta cell mass, minus the sinks for insulin, which are proportional to body weight [29]. The resulting model prediction for EBCM as a function of age is shown in Figure 3 (solid line). The trendline obtained by linear regression (dotted line) and the observed reduction in beta cell mass in pancreata obtained from the subset of recent onset patients (i.e., died within three weeks of diagnosis) are also shown for comparison. The EBCM relationship exhibits a similar dependence with age, as the youngest patients exhibited an 85% reduction in beta cell mass while only a 40% reduction was observed by the age of 20. In other words, the beta cell mass initially grows at a faster rate relative to the whole body. The beta cell mass peaks at 8 years of age and remains constant while the overall body weight peaks at 20 years of age. The net result of the different growth dynamics is that the “excess” beta cell mass declines with age. In addition, the mathematical model provides a

prediction of the beta cell mass required to maintain glucose homeostasis. As a validation of the model, one finds that the difference between the observed and predicted beta cell mass (i.e., residual beta cell mass) parallels the observed changes in C-peptide following diagnosis (see Figure 5), as described in [34].

In summary, this model (i.e., prototype) suggests that clinical presentation of the disease is not attributed solely to the destruction of beta cell mass but is the result of a dynamic balance between the production of insulin (i.e., beta cell mass) and the size of the system (i.e., body weight). The agreement between the model-based predictions and the reported changes in C-peptide suggests two points. First, the methods that were used in these landmark studies exhibit a certain degree of accuracy in estimating beta cell mass, while the methods may not have had good precision. By using a mathematical model to interpret the trends in the data, we are able to correct for the imprecision of the assays used. Second, the similar dynamic trends suggest that the natural history of the disease is similar across the collection of clinical studies. While the biological details associated with the autoimmune attack on the pancreas and regulation of human metabolism are missing in this simplified model, the model exhibits a fitness for use in that it is sufficiently complex to answer the question posed. Using a mathematical model to represent our prior knowledge of the biology, the model provides a unique perspective to interpret these landmark studies which challenges the common wisdom in the field of type 1 diabetes. Improved understanding of the natural history of the disease—as it helps suggest causality—is a necessary prerequisite for improving the clinical management of the disease. Understanding causality is essential for developing new drugs that hold promise for a cure.

4. Example 2: The Role of Dendritic Cells in Adaptive Immunity

The human immune system provides the body with natural defenses against the constant onslaught of overt and opportunistic pathogens. This defense against invading pathogens is an emergent behavior of a collection of heterogeneous cell subsets and typifies a complex system [35]. Individually, each of these subsets have unique roles in orchestrating an immune response. Together, these cell subsets integrate information across a range of spatial and temporal timescales. Despite the impressive advances in the field of immunology in the past decades, we know relatively little about the interplay between the individual components responsible for immunity [1, 36]. A mathematical model provides a quantitative framework where fragmented knowledge can be synthesized to predict integrated behavior of these components. In the remainder of this section, we will discuss a prototype that focuses on a cell subset that plays a central role in orchestrating an immune response—dendritic cells (DC)—in the lung.

As the sentinels of the immune system, dendritic cells (DCs) play an important role in initiating and maintaining T-cell responses, such as T-helper cell polarization and

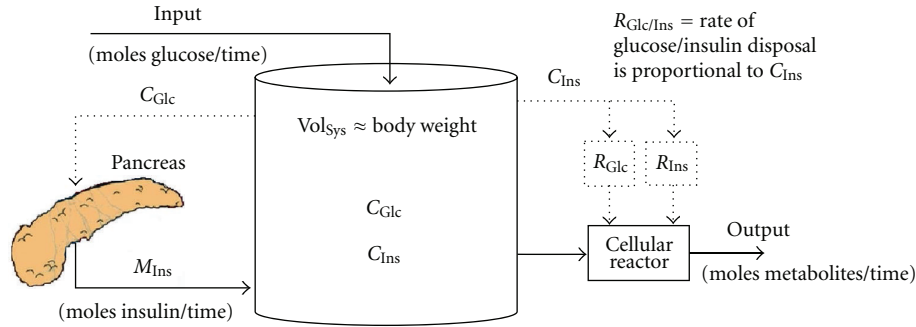


FIGURE 4: A schematic process diagram of the interplay between insulin production and glucose homeostasis. The regulation of substrate metabolism is modeled as an open system, where the concentrations of insulin (C_{Ins}) and glucose (C_{Glc}) are influenced by flows in (e.g., a glucose input and pancreatic production of insulin (M_{Ins})) and out (e.g., the disposal of glucose through cellular metabolism or the disposal of insulin through cellular proteolysis) of the system. Material flows are represented by solid lines while the flow of information is represented as a dotted line. For instance, the production of insulin by the pancreas—a material flow—is regulated by concentration of plasma glucose—a flow of information. The molar production of insulin by the pancreas is the product of the beta cell mass times the insulin production per beta cell. Similarly, the rates of disposal of insulin and glucose within the system (R_{Ins} and R_{Glc}) are regulated by the concentration of plasma insulin. The concentration of insulin is a derived intrinsic quantity where the moles of insulin produced by the pancreas are distributed throughout the system volume, which is proportional to body weight.

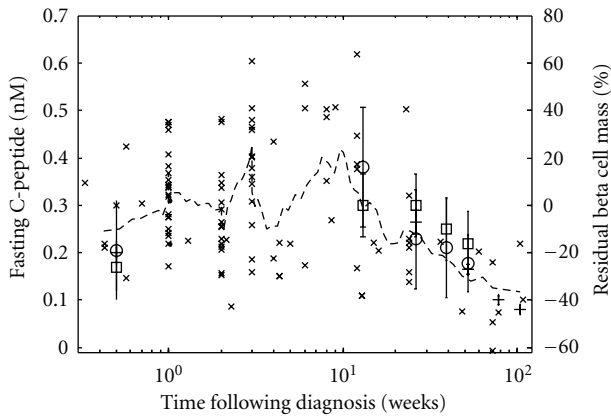


FIGURE 5: Dynamic change in residual beta cell mass corresponds to the dynamic change in plasma C-peptide following onset of type 1 diabetes. The residual beta cell mass (x: right axis) and plasma C-peptide (square [31], circle [32], and + [30]: left axis) are shown as a function of time following clinical diagnosis of type 1 diabetes. A 9-point moving average of the residual beta cell mass is shown for comparison (dotted line). The residual beta cell mass is the difference between the observed beta cell mass and predicted beta cell mass. The dynamic change in observed beta cell mass was obtained from pancreata obtained from patients with type 1 diabetes [25–27]. The predicted beta cell mass is an estimate of the minimum beta cell mass required to maintain glucose homeostasis. Figure was originally published in [34].

crosspresentation of exogenous antigens to cytotoxic T cells [37, 38]. The precise role played by DC in *de novo* activation of T cells is the culmination of a series of steps distributed across both space and time. These sequential steps include the recruitment into a peripheral tissue, capture of antigen, trafficking to a draining lymph node, and presentation of antigen to T cells [37, 39]. A generalized schematic of this process is shown in Figure 6. Human biopsy data

suggest that the majority of dendritic cells in the lung epithelium are derived from either blood monocytes (BMs) or blood dendritic (BD) cells [40]. Individually, BM and BD represent 97% and 3% of the DC precursor population in the blood. Although these DC precursor cells can be easily assayed in the blood, their relative contributions to the dendritic cell population within the lung epithelium and their functional roles in driving an immune response are unknown. Moreover, the role of BD has been largely ignored due to its relative rarity as a DC precursor.

To explore the implications of DC precursor recruitment into the lung, we created a mathematical model that captures the dynamics and origin of tissue dendritic cells [41, 42]. The dynamic model suggests that BDs are selectively enriched within the lung as they comprise 20% of the DC population in the lung [41]. While it is intriguing that BD may exhibit a higher affinity for the recruitment stimuli compared to BM, a more important question is whether this observation is functionally significant. The structure of the model was designed to capture an important aspects of dendritic cell biology—an age-structure.

As a dendritic cell traverses from blood to lung to lymph node, it turns on different “subroutines” encoded within its genes enabling it to perform different functions within each compartment. The dynamic execution of these subroutines is represented by dynamic changes in proteins expressed on the surface of a DC. The sequence of cellular changes are collectively referred to as DC maturation. Proteins expressed on the cell surface enable a cell to sense and respond to its environment. These dynamic changes in DC proteins indicate that the particular cellular response of a DC to the environmental context is highly dependent on the DC’s particular maturational age. In addition, the ability of a DC to capture and process protein antigens derived from invading pathogens is also highly dependent on the maturational state of a DC. Given the dynamic nature of the DC population, the appropriate computational paradigm

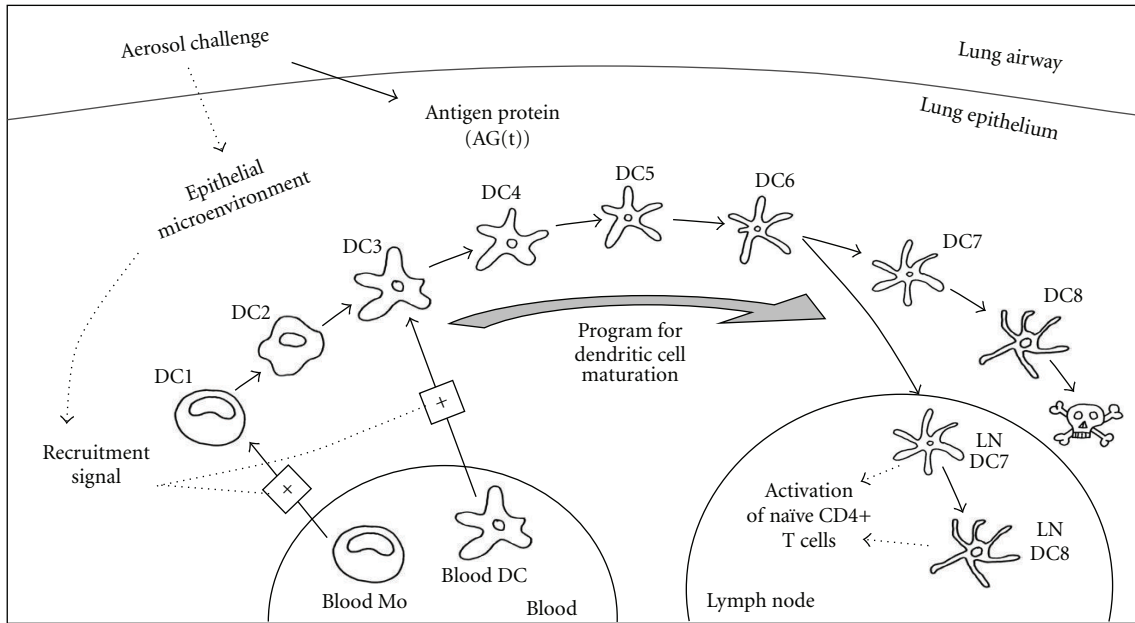


FIGURE 6: Schematic diagram of mathematical model for dendritic cell trafficking within the lung epithelial microenvironment. An aerosol challenge results in the increase of antigenic proteins and the recruitment of DC precursors from the blood into the lung epithelium. DCs dynamically traffic through the lung epithelium and become programmed by the prevailing epithelial microenvironment. Upon maturation, DCs migrate into the lymph nodes and present antigenic peptides obtained in the lung epithelium to naïve CD4+ T helper cells.

for representing DC populations is a model structured by maturational age [41, 42].

While physiologically-structured models have been proposed since the mid-1960s [43], they are seldom used to describe cell populations due to the difficulty in obtaining appropriate experimental data and the mathematical complexity of the resulting models. Given appropriate data, the additional complexity enables asking different questions. The dynamic response of cell populations in the blood to perturbations has been represented using physiologically-structured models (e.g., [44, 45]). In this case, age-associated differences in antigen processing ability of these two DC precursor populations can be compared by explicitly tracking the functionally unique subpopulations. Differences between BM- and BD-derived DC become especially apparent when antigen proteins also change with time. When antigen proteins have a half-life in the tissue of 60 minutes, BD-derived DC presents 250% more antigen peptide per cell relative to the DC derived from BM. *De novo* activation of T-helper cells requires that signals, including the density of antigen peptides, exceed activation thresholds [46, 47]. If the density of antigen peptides is averaged across all DC subsets, the dynamic change in density of peptides may be below the threshold required for activation of T-helper cells. By explicitly accounting for variability in DC phenotypes, the density of peptides presented by this minority DC subset may exceed the threshold for activation. While these studies highlight the importance of measuring DC heterogeneity, they also highlight how computer models can be used to integrate heterogeneous data into a quantitative picture of the dynamic role of dendritic cells in coordinating immunity.

5. Reflecting Back: Goldilocks and the Two Maxims

The use of models to aid in understanding system behavior is a central theme in science that transcends disciplinary boundaries [48]. In the previous sections, two examples served to illustrate some of the nuances associated with mathematical modeling from an engineering perspective, namely, the concepts of prototyping and fitness for use.

In the case of the type 1 diabetes model, the two competing theories are that the degree of beta cell reduction at onset is a fixed value or that the observed reduction is a result of a dynamic balance between beta cell mass and body weight. From a mathematical perspective, the models exhibit similar complexity as both models use a single adjustable parameter to predict the observed behavior. The Akaike Information Criterion [49–51], based upon information theory, is used to distinguish between these competing models using the available data. Intensive computing techniques, like nonparametric bootstrap resampling [52, 53] and empirical Bayesian methods [17], complement information-theoretic metrics by assessing the uncertainty of those metrics, given the inherent uncertainty in measuring biological systems. Moreover, this simplified model was also able to compare changes in beta cell mass to changes in C-peptide following diagnosis [34]. Finally, one could construct a model that includes more detail regarding the different timescales for insulin production [54–56], insulin signaling [57], and beta cell autoimmunity [58]. However, the simplified model exhibits a fitness for use as inclusion of such detail is unnecessary to test the prevailing theory.

In the case of the dendritic cell trafficking study, a new model is proposed to represent cellular heterogeneity and to provide an estimate of its potential importance. In contrast, existing models that assume that all dendritic cells are homogeneous (e.g., [59]) are unable to capture with the observed dynamic patterns of cell surface marker expression during dendritic cell maturation [60–62]. Additional structure is required to represent this cellular heterogeneity within the model. Using computational techniques, such as parameter identification [63, 64], the increased cost, in terms of parameters, associated with a more complex model that captures a larger set of data is justified. Yet, the age-structured modeling framework is not well suited to explore questions related to the spatial organization of the lymph node or the discrete nature of cell-to-cell interactions. The form of the age-structured model, which is a set of coupled ordinary differential equations, assumes that the age compartments are well mixed, that is the cells are homogeneous within an age compartment. Agent-based models of the lymph node are better suited to such questions [65–68]. Historically, agent-based models focus on cell population-level behavior and neglect the molecular details associated with cellular decision making, such as an evolution in cell phenotype due to local changes in developmental cues. Although, models that aim to combine cellular-level with population-level behavior are emerging [69]. This highlights the iterative nature of the engineering design process. As additional data become available, the mathematical prototype can be revised to reflect this new information. Moreover, the form of the model may change depending on the fitness for use of the particular mathematical framework (e.g., ordinary differential equation-based or agent-based model) to address the questions of interest.

Reminiscent of the notable children's story "Goldilocks and the Three Bears," a common criticism of a particular mathematical model is that it is either too complicated or too simplistic. In many cases, these statements are subjective as they are based upon the collective experience of the critic [19]. One of the benefits of representing theory in a computable form is that computational tools can be used to assess objectively the complexity of the model. Implied in the criticism is the question of model parsimony. Conventionally, there are two maxims that bracket the range of plausible explanations for observed phenomena: Ockham's Razor and Einstein's Safety Shield. The concept of Ockham's Razor is that if there are a series of theories and the available data cannot distinguish between the different theories, then the simplest theory should receive priority. The concept of Einstein's Safety Shield is that one should construct the simplest theory to explain observed phenomena but no simpler. The emergence of information-theoretic approaches provides a quantitative basis for these maxims (see [70] for an introduction to the topic). While these are important topics to consider when modeling immunology [71], information-theoretic concepts have been infrequently applied to modeling efforts in the field [72]. Recent developments in rule-based modeling [73–75], time scale analysis [76], and in silico model-based inference [17] all help reduce the barrier for integrating theory—in the

form of mathematical models and engineering concepts—with experimental immunology. Within the domain of cellular decision making, the combination of these three modeling developments allow one to specify a mathematical model with limited a priori bias in the model structure and use the available data to determine objectively the appropriate level of complexity, as illustrated in this sequence of papers [76–78].

In summary, engineering is historically a field in which basic research is translated into commercially viable products and processes. The commercial synthesis of basic science data is achieved using computational frameworks. Translating data into knowledge is a major challenge facing contemporary health science research. Two examples discussed in the previous paragraphs aim to illustrate how the computational toolkit of an engineer can be integrated into experimental immunology via mathematical prototyping. These examples also serve to illustrate that embracing a quantitative perspective provides an opportunity to integrate focused experimentation into a larger mosaic that describes human immunity. Through mathematical prototyping we are able to represent explicitly our prior knowledge of the dynamics of immunity and test this prior knowledge against experimental data. Moreover, the process of creating a mathematical model provides a roadmap for future experimental effort by identifying important knowledge gaps in the collective scientific understanding. Ultimately, improved understanding of the complexity of biological systems is essential for promoting human health and restoring health through the rational design of new therapeutics.

Acknowledgments

This work was supported by grants from the National Science Foundation (CAREER 1053490 to David J. Klinke II), the National Cancer Institute (R15CA132124 to David J. Klinke II), and the National Institute of General Medical Sciences (P20GM103434 to QingWang). The content is solely the responsibility of the authors and does not necessarily represent the official views of the NSF, the National Cancer Institute, the National Institute of General Medical Sciences, or the NIH.

References

- [1] A. K. Abbas and C. A. Janeway Jr., "Immunology: improving on nature in the twenty-first century," *Cell*, vol. 100, no. 1, pp. 129–138, 2000.
- [2] FDA, "Innovation or stagnation: challenge and opportunity on the critical path to new medical products," 2004.
- [3] D. B. Searls, "Data integration: challenges for drug discovery," *Nature Reviews Drug Discovery*, vol. 4, no. 1, pp. 45–58, 2005.
- [4] P. K. Sorger and S. R. B. Allerheiligen, "Quantitative and systems pharmacology in the postgenomic era: new approaches to discovering drugs and understanding therapeutic mechanisms," Tech. Rep., 2011, An NIH white paper by the QSP workshop group, NIGMS.
- [5] The Congress of the United States and Congressional Budget Office, Research and development in the pharmaceutical industry, 2006.

- [6] J. M. Ottino, "New tools, new outlooks, new opportunities," *AIChE Journal*, vol. 51, no. 7, pp. 1840–1845, 2005.
- [7] National Research Council (U.S.) Committee on Challenges for the Chemical Sciences in the 21st Century, *Beyond the Molecular Frontier: Challenges for Chemistry and Chemical Engineering*, National Academies Press, Washington, DC, USA, 2003.
- [8] G. Stephanopoulos, "Chemical and biological engineering," *Chemical Engineering Science*, vol. 58, pp. 3291–3293, 2003.
- [9] National Research Council (U.S.). Committee on Defining and Advancing the Conceptual Basis of Biology in the 21st Century, *The Role of Theory in Advancing 21st Century Biology: Catalyzing Transformative Research*, National Academies Press, Washington, DC, USA, 2008.
- [10] J. Keener and J. Sneyd, *Mathematical Physiology*, Springer, New York, NY, USA, 2001.
- [11] L. S. Hirsch, S. J. Gibbons, H. Kimmel, R. Rockland, and J. Bloom, "High school students—attitudes to and knowledge about engineering," *Frontiers in Education*, FIE, 33rd Annual, 2:2, 2003.
- [12] W. G. Vincenti, *What Engineers Know and How They Know It*, John Hopkins Press, Baltimore, Md, USA, 1990.
- [13] P. G. Dominick, J. T. Demel, W. M. Lawbaugh, R. J. Freuler, G. L. Kinzel, and E. Fromm, *Tools and Tactics of Design*, John Wiley & Sons, New York, NY, USA, 2001.
- [14] J. M. Juran, *Juran on Leadership for Quality*, Free Press, New York, NY, USA, 1989.
- [15] R. Aris, *Mathematical Modelling Techniques*, Dover Publications, Mineola, NY, USA, 1995.
- [16] A. Saltelli, K. Chan, and E. M. Scott, *Sensitivity Analysis Wiley Series in Probability and Statistics*, John Wiley & Sons, New York, NY, USA, 2000.
- [17] D. J. Klink, "An empirical Bayesian approach for model-based inference of cellular signaling networks," *BMC Bioinformatics*, vol. 10, no. 1, article 371, 2009.
- [18] S. L. Star and J. R. Griesemer, "Institutional ecology, translations and boundary objects—amateurs and professionals in berkeleys museum of vertebrate zoology," *Social Studies of Science*, vol. 19, pp. 387–420, 1989.
- [19] National Research Council (U.S.). Committee on Learning, *How People Learn: Brain, Mind, Experience, and School*, National Academies Press, Washington, DC, USA, 2000.
- [20] World Health Organization, "Report of a WHO consultation," Part 1: diagnosis and classification of diabetes mellitus, 1999.
- [21] M. A. Atkinson and G. S. Eisenbarth, "Type 1 diabetes: new perspectives on disease pathogenesis and treatment," *The Lancet*, vol. 358, no. 9277, pp. 221–229, 2001.
- [22] P. Onkamo, S. Väänänen, M. Karvonen, and J. Tuomilehto, "Worldwide increase in incidence of type I diabetes—the analysis of the data on published incidence trends," *Diabetologia*, vol. 42, no. 12, pp. 1395–1403, 1999.
- [23] E. A. M. Gale, "Can we change the course of beta-cell destruction in type 1 diabetes?" *The New England Journal of Medicine*, vol. 346, no. 22, pp. 1740–1742, 2002.
- [24] J. Daaboul and D. Schatz, "Overview of prevention and intervention trials for type 1 diabetes," *Reviews in Endocrine and Metabolic Disorders*, vol. 4, no. 4, pp. 317–323, 2003.
- [25] A. K. Foulis, C. N. Liddle, M. A. Farquharson, J. A. Richmond, and R. S. Weir, "The histopathology of the pancreas in type I (insulin-dependent) diabetes mellitus: a 25-year review of deaths in patients under 20 years of age in the United Kingdom," *Diabetologia*, vol. 29, no. 5, pp. 267–274, 1986.
- [26] A. K. Foulis, M. A. Farquharson, and R. Hardman, "Aberant expression of class II major histocompatibility complex molecules by B cells and hyperexpression of Class I major histocompatibility complex molecules by insulin containing islets in Type 1 (insulin-dependent) diabetes mellitus," *Diabetologia*, vol. 30, no. 5, pp. 333–343, 1987.
- [27] W. Gepts, "Pathologic anatomy of the pancreas in juvenile diabetes mellitus," *Diabetes*, vol. 14, no. 10, pp. 619–633, 1965.
- [28] N. A. Sherry, E. B. Tsai, and K. C. Herold, "Natural history of β -cell function in type 1 diabetes," *Diabetes*, vol. 54, supplement 2, pp. S32–S39, 2005.
- [29] D. J. Klink, "Extent of beta cell destruction is important but insufficient to predict the onset of type 1 diabetes mellitus," *PLoS ONE*, vol. 3, no. 1, Article ID e1374, 2008.
- [30] J. Komulainen, M. Knip, R. Lounamaa et al., "Poor beta-cell function after the clinical manifestation of type 1 diabetes in children initially positive for islet cell specific autoantibodies," *Diabetic Medicine*, vol. 14, pp. 532–537, 1997.
- [31] P. Pozzilli, D. Pitocco, N. Visalli et al., "No effect of oral insulin on residual beta-cell function in recent-onset type I diabetes (the IMDIAB VII)," *Diabetologia*, vol. 43, no. 8, pp. 1000–1004, 2000.
- [32] L. Chaillous, H. Lefevre, C. Thivolet et al., "Oral insulin administration and residual β -cell function in recent-onset type 1 diabetes: a multicentre randomised controlled trial," *The Lancet*, vol. 356, no. 9229, pp. 545–549, 2000.
- [33] R. J. Kuczmarski, C. L. Ogden, L. M. Grummer-Strawn et al., "CDC growth charts: United States," *Advance Data*, no. 314, pp. 1–27, 2000.
- [34] D. J. Klink, "Age-corrected beta cell mass following onset of type 1 diabetes mellitus correlates with plasma C-peptide in humans," *PLoS ONE*, vol. 6, no. 11, Article ID e26873, 2011.
- [35] R. N. Germain, "The art of the probable: system control in the adaptive immune system," *Science*, vol. 293, no. 5528, pp. 240–245, 2001.
- [36] A. O'Garra, L. Gabryšová, and H. Spits, "Quantitative events determine the differentiation and function of helper T cells," *Nature Immunology*, vol. 12, no. 4, pp. 288–294, 2011.
- [37] H. Ueno, E. Klechevsky, R. Morita et al., "Dendritic cell subsets in health and disease," *Immunological Reviews*, vol. 219, no. 1, pp. 118–142, 2007.
- [38] R. M. Steinman, "Decisions about dendritic cells: past, present, and future," *Annual Review of Immunology*, vol. 30, pp. 1–22, 2012.
- [39] J. Banchereau, F. Briere, C. Caux et al., "Immunobiology of dendritic cells," *Annual Review of Immunology*, vol. 18, pp. 767–811, 2000.
- [40] F. L. Jahnsen, E. D. Moloney, T. Hogan, J. W. Upham, C. M. Burke, and P. G. Holt, "Rapid dendritic cell recruitment to the bronchial mucosa of patients with atopic asthma in response to local allergen challenge," *Thorax*, vol. 56, no. 11, pp. 823–826, 2001.
- [41] D. J. Klink, "An age-structured model of dendritic cell trafficking in the lung," *American Journal of Physiology*, vol. 291, no. 5, pp. L1038–L1049, 2006.
- [42] D. J. Klink, "A multi-scale model of dendritic cell education and trafficking in the lung: implications for T cell polarization," *Annals of Biomedical Engineering*, vol. 35, no. 6, pp. 937–955, 2007.
- [43] A. G. Fredrickson, "Population balance equations for cell and microbial cultures revisited," *AIChE Journal*, vol. 49, no. 4, pp. 1050–1059, 2003.
- [44] J. Bélair, M. C. Mackey, and J. M. Mahaffy, "Age-structured and two-delay models for erythropoiesis," *Mathematical Biosciences*, vol. 128, no. 1–2, pp. 317–346, 1995.

- [45] J. M. Mahaffy, J. Bélair, and M. C. Mackey, "Hematopoietic model with moving boundary condition and state dependent delay: applications in erythropoiesis," *Journal of Theoretical Biology*, vol. 190, no. 2, pp. 135–146, 1998.
- [46] R. H. Schwartz and D. L. Mueller, "Immunological tolerance," in *Fundamental Immunology*, W. E. Paul, Ed., Lippincott Williams & Wilkins, Philadelphia, Pa, USA, 2003.
- [47] S. E. Henrickson, T. R. Mempel, I. B. Mazo et al., "T cell sensing of antigen dose governs interactive behavior with dendritic cells and sets a threshold for T cell activation," *Nature Immunology*, vol. 9, no. 3, pp. 282–291, 2008.
- [48] American Association for the Advancement of Science, *Science for All Americans*, Oxford University Press, New York, NY, USA, 1990.
- [49] H. Akaike, "A new look at the statistical model identification," *IEEE Transactions on Automatic Control*, vol. 19, no. 6, pp. 716–723, 1974.
- [50] K. Yamaoka, T. Nakagawa, and T. Uno, "Application of Akaike's information criterion (AIC) in the evaluation of linear pharmacokinetics equations," *Journal of Pharmacokinetics and Biopharmaceutics*, vol. 6, no. 2, pp. 165–175, 1978.
- [51] R. Horn, "Statistical methods for model discrimination. Applications to gating kinetics and permeation of the acetylcholine receptor channel," *Biophysical Journal*, vol. 51, no. 2, pp. 255–263, 1987.
- [52] B. Efron and R. Tibshirani, "Bootstrap methods for standard errors, confidence intervals, and other measures of statistical accuracy," *Statistical Science*, vol. 1, pp. 54–75, 1986.
- [53] M. R. Chernick, *Bootstrap Methods: A Practitioner's Guide*, John Wiley & Sons, New York, NY, USA, 1999.
- [54] M. G. Pedersen, R. Bertram, and A. Sherman, "Intra- and inter-islet synchronization of metabolically driven insulin secretion," *Biophysical Journal*, vol. 89, no. 1, pp. 107–119, 2005.
- [55] R. Nesher and E. Cerasi, "Modeling phasic insulin release: immediate and time-dependent effects of glucose," *Diabetes*, vol. 51, supplement 1, pp. S53–S59, 2002.
- [56] A. E. Butler, J. Janson, S. Bonner-Weir, R. Ritzel, R. A. Rizza, and P. C. Butler, " β -cell deficit and increased β -cell apoptosis in humans with type 2 diabetes," *Diabetes*, vol. 52, no. 1, pp. 102–110, 2003.
- [57] A. R. Sedaghat, A. Sherman, and M. J. Quon, "A mathematical model of metabolic insulin signaling pathways," *American Journal of Physiology*, vol. 283, no. 5, pp. E1084–E1101, 2002.
- [58] L. Shoda, H. Kreuwel, K. Gadkar et al., "The type 1 diabetes physioLab platform: a validated physiologically based mathematical model of pathogenesis in the non-obese diabetic mouse," *Clinical and Experimental Immunology*, vol. 161, no. 2, pp. 250–267, 2010.
- [59] S. Marino and D. E. Kirschner, "The human immune response to Mycobacterium tuberculosis in lung and lymph node," *Journal of Theoretical Biology*, vol. 227, no. 4, pp. 463–486, 2004.
- [60] V. E. Woodhead, M. H. Binks, B. M. Chain, and D. R. Katz, "From sentinel to messenger: an extended phenotypic analysis of the monocyte to dendritic cell transition," *Immunology*, vol. 94, no. 4, pp. 552–559, 1998.
- [61] A. Dzionic, A. Fuchs, P. Schmidt et al., "BDCA-2, BDCA-3, and BDCA-4: three markers for distinct subsets of dendritic cells in human peripheral blood," *Journal of Immunology*, vol. 165, no. 11, pp. 6037–6046, 2000.
- [62] C. Caux, C. Massacrier, B. Vanbervliet et al., "CD34+ hematopoietic progenitors from human cord blood differentiate along two independent dendritic cell pathways in response to granulocyte- macrophage colony-stimulating factor plus tumor necrosis factor α : II. Functional analysis," *Blood*, vol. 90, no. 4, pp. 1458–1470, 1997.
- [63] J. A. Jacquez and T. Perry, "Parameter estimation: local identifiability of parameters," *American Journal of Physiology*, vol. 258, no. 4, pp. E727–E736, 1990.
- [64] S. Audoly, G. Bellu, L. D'Angiò, M. P. Saccomani, and C. Cobelli, "Global identifiability of nonlinear models of biological systems," *IEEE Transactions on Biomedical Engineering*, vol. 48, no. 1, pp. 55–65, 2001.
- [65] J. Hu, G. Nudelman, Y. Shimoni et al., "Role of cell-to-cell variability in activating a positive feedback antiviral response in human dendritic cells," *PLoS ONE*, vol. 6, no. 2, Article ID e16614, 2011.
- [66] J. J. Linderman, T. Riggs, M. Pande, M. Miller, S. Marino, and D. E. Kirschner, "Characterizing the dynamics of CD4+ T cell priming within a lymph node," *Journal of Immunology*, vol. 184, no. 6, pp. 2873–2885, 2010.
- [67] G. Bogle and P. R. Dunbar, "Agent-based simulation of T-cell activation and proliferation within a lymph node," *Immunology and Cell Biology*, vol. 88, no. 2, pp. 172–179, 2010.
- [68] V. Baldazzi, P. Paci, M. Bernaschi, and F. Castiglione, "Modeling lymphocyte homing and encounters in lymph nodes," *BMC Bioinformatics*, vol. 10, article 387, 2009.
- [69] S. D. Hester, J. M. Belmonte, J. S. Gens, S. G. Clendenon, and J. A. Glazier, "A multicell, multi-scale model of vertebrate segmentation and somite formation," *PLoS Computational Biology*, vol. 7, no. 10, Article ID e1002155, 2011.
- [70] A. R. A. Anderson and V. Quaranta, "Integrative mathematical oncology," *Nature Reviews Cancer*, vol. 8, no. 3, pp. 227–234, 2008.
- [71] C. T. H. Baker, G. A. Bocharov, J. M. Ford et al., "Computational approaches to parameter estimation and model selection in immunology," *Journal of Computational and Applied Mathematics*, vol. 184, no. 1, pp. 50–76, 2005.
- [72] S. M. Andrew, C. T. H. Baker, and G. A. Bocharov, "Rival approaches to mathematical modelling in immunology," *Journal of Computational and Applied Mathematics*, vol. 205, no. 2, pp. 669–686, 2007.
- [73] J. R. Faeder, M. L. Blinov, and W. S. Hlavacek, "Rule-based modeling of biochemical systems with BioNetGen," *Methods in Molecular Biology*, vol. 500, pp. 113–167, 2009.
- [74] J. Feret, V. Danos, J. Krivine, R. Harmer, and W. Fontana, "Internal coarse-graining of molecular systems," *Proceedings of the National Academy of Sciences of the United States of America*, vol. 106, no. 16, pp. 6453–6458, 2009.
- [75] J. A. Bachman and P. Sorger, "New approaches to modeling complex biochemistry," *Nature Methods*, vol. 8, no. 2, pp. 130–131, 2011.
- [76] D. J. Klinke and S. D. Finley, "Timescale analysis of rule-based biochemical reaction networks," *Biotechnology Progress*, vol. 28, pp. 33–44, 2012.
- [77] S. D. Finley, D. Gupta, N. Cheng, and D. J. Klinke, "Inferring relevant control mechanisms for interleukin-12 signaling in nave CD4 T cells," *Immunology and Cell Biology*, vol. 89, no. 1, pp. 100–110, 2011.
- [78] D. J. Klinke, N. Cheng, and E. Chambers, "Quantifying cross-talk among interferongamma, interleukin-12 and tumor necrosis factor signaling pathways within a Th1 cell model," *Science Signaling*, vol. 5, no. 220, article ra32, 2012.

Research Article

A Mathematical Model of Immune-System-Melanoma Competition

Marzio Pennisi

Department of Mathematics & Computer Science, University of Catania, V.le A Doria 6, 95125 Catania, Italy

Correspondence should be addressed to Marzio Pennisi, mpennisi@dm.unict.it

Received 9 March 2012; Accepted 2 April 2012

Academic Editor: Francesco Pappalardo

Copyright © 2012 Marzio Pennisi. This is an open access article distributed under the Creative Commons Attribution License, which permits unrestricted use, distribution, and reproduction in any medium, provided the original work is properly cited.

We present a mathematical model developed to reproduce the immune response entitled with the combined administration of activated OT1 cytotoxic T lymphocytes (CTLs) and Anti-CD137 monoclonal antibodies. The treatment is directed against melanoma in B16 OVA mouse models exposed to a specific immunotherapy strategy. We model two compartments: the injection point compartment where the treatment is administered and the skin compartment where melanoma tumor cells proliferate. To model the migration of OT1 CTLs and antibodies from the injection to the skin compartment, we use delay differential equations (DDEs). The outcomes of the mathematical model are in good agreement with the in vivo results. Moreover, sensitivity analysis of the mathematical model underlines the key role of OT1 CTLs and suggests that a possible reduction of the number of injected antibodies should not affect substantially the treatment efficacy.

1. Introduction

Melanoma is a malignant tumor caused by the mutation of melanocytes, that is, the cells that produce the melanin and are responsible of the color of the skin. Despite intensive research, melanoma still represents one of the most aggressive malignant cancers [1]. Many experimental approaches are now focused on targeting cytotoxic T lymphocytes (CTLs) against cancer. A common strategy to enable CTL efficacy against tumor is to activate naïve CTLs in vitro through the use of cells engineered to present the tumor antigen, and to reinject them in the host. However, even if activated CTLs are able to infiltrate into tumor masses, in most cases they remain unable to contrast cancer growth [2]. As experimental evidence suggests, tumor-infiltrating lymphocytes are rendered ineffective by coinhibitory molecules expressed by tumor and stroma cells surfaces [3].

In order to gain complete rejection of tumors, injection and stimulation of CTLs is not sufficient and should be, therefore, coupled with complementary measures voted at boosting CTLs migration inside tumor masses, and conjugation and killing of target cells [4–6]. One way of boosting CTLs actions is represented by stimulation through the binding of costimulatory proteins expressed on CTLs

surface. Among possible surface proteins, Anti-CD137, also known as 4-1BB, represents a valuable target. This protein is expressed by multiple IS cells such as activated T, NK, B-lymphocytes, dendritic cells and also by tumor endothelium cells [7]. Its natural ligand (CD137L) can be found on activated antigen-presenting cells surface [8].

The combined administration of monoclonal antibodies specifically targeted to bind Anti-CD137 proteins and in vitro activated-OT1 CTLs was demonstrated to be able to prevent the melanoma formation in B16-OVA mouse models [7]. Moreover, the combined treatment avoided appearing of undesired side effects like the hepatotoxicity, observed only under anti-CD137 only high-dosage treatment [9]. The IS stimulation mechanisms of Anti-CD137 immunostimulatory monoclonal antibodies are multilayered and include the improving of cytotoxicity, duplication rates, and chemotaxis sensitivity of activated-OT1 CTLs [6, 10–12].

To reproduce the dynamics of this biological process, a delay differential-equation-(DDE-) based model has been developed. The model reproduces two different compartments: the injection point compartment, where both antibodies and OT1 cells are injected and the skin compartment where melanoma develops.

2. Biological Background

The in vivo experiment is carried on B16-OVA mice, mice transduced with the chicken ovalbumin gene. The ovalbumin is used as a model tumor antigen. B16 melanoma cell line was derived from an aggressive spontaneous melanoma in pure C57BL6, and B16F10 was derived as a clonal variant from a lung metastasis of this cell line. In tumor immunology, these variants of melanoma are considered poorly immunogenic in the sense that immune-mediated rejections or growth retardations are difficult to achieve.

The experimental setup is oriented to model therapeutic synergy between anti-CD137 monoclonal antibodies and adoptive T cell therapy in melanoma. B16-OVA is a poorly immunogenic murine tumor. The treatment protocol includes a single injection of anti-CD137 mAb and adoptive T cell transfer of OVA-specific TCR-transgenic CD8 CTLs.

In vivo experiments have been executed by Professor Melero and coworkers at the University of Navarra [13]. Mice are divided in five different groups; all groups are composed by five individuals. Each group is treated with a different treatment: Untreated (control) mice, mice treated with naïve OT1 CTLs, mice treated with naïve OT1 CTLs and Anti-CD137 monoclonal antibodies, and mice treated with in vitro activated OT1 CTLs, mice treated with Anti-CD137 monoclonal antibodies, mice treated with in vitro activated OT1 CTLs and Anti-CD137 monoclonal antibodies. The experiment runs for 30 days. At day 0, all B16-OVA mice receive one injection of melanoma malignant cells. The therapeutic treatment used during in vivo experiments is composed by one single boost, and it is administered at day 3. Melanoma surface measurements (mm^2) are taken at given times for each treatment and are used to estimate the efficacy of each vaccination strategy. We note here that in order to compare in vivo and in silico results we computed the estimated mean surfaces entitled with the use of each treatment. Among the tested treatments, only the combined administration of activated OT1 CTLs and antibodies was able to show complete depletion of the tumor burden, whereas the other treatments remained almost ineffective [13].

3. The Model

We realized a model with two compartments in order to reproduce the dynamics of the process. The first compartment is represented by the injection point compartment where the treatment is administered, whereas the second one is represented by the skin compartment where melanoma tumor cells proliferate and where the cancer-IS competition occurs. To this end, a system of seven delay differential equations has been set up. The model takes into account the following entities: injected activated OT1 CTLs (E) and injected antibodies (Ab) for the injection point compartment; melanoma cells (C), tumor antigens (A), activated OT1 CTLs and antibodies that have reached the skin (E_s and A_s) and naïve CTLs (N) for the skin compartment. It has also been assumed that Injected OT1 CTLs, and antibodies move from the injection point to the skin compartment

TABLE 1: Model variables. Each variable describes the total number of the related entity in the associated compartment.

Variable	Description	compartment
E	Injected activated OT1 CTLs	injection point
Ab	Injected anti-CD137 antibodies	injection point
C	Melanoma tumor cells	skin
A	Tumor antigens	skin
E_s	Activated OT1 CTLs	skin
A_s	Injected anti-CD137 antibodies	skin
N	Naïve CTLs	skin

only. Figure 1 shows the conceptual model for the biological problem; model entities are listed in Table 1.

(1) Activated OT1 CTLs (injection point compartment):

$$\frac{dE}{dt} = K_{\text{in}}(t, p) - \alpha_{11}E - \alpha_8E. \quad (1)$$

Equation (1) refers to first compartment and represents the time evolution of injected activated OT1 CTLs. In (1), $K_{\text{in}}(t, p)$ represents a known function that models the number of inoculated entities r at the scheduled injection time t . E cells migrate from the injection point compartment to the skin compartment with given rates $(-\alpha_{11}E)$ and are subject to natural death $(-\alpha_8E)$.

(2) Antibodies (injection point compartment):

$$\frac{dAb}{dt} = K_{\text{in}}(t, q) - \alpha_{11}Ab - \alpha_{10}Ab. \quad (2)$$

Similar to (1), (2) refers to the first compartment and represents the time evolution of antibodies (Ab). Ab are injected at given times t and at given quantities q , according to the function $K_{\text{in}}(t, q)$, and can migrate and disappear from the system by natural degradation at given rates $(-\alpha_{11}Ab$ and $-\alpha_{10}Ab$, resp.).

(3) Activated OT1 CTLs (skin compartment):

$$\frac{dE_s}{dt} = \alpha_7 \left[\frac{A_s}{A_s + k_1} \right] E_s + \alpha_{11}E(t - \tau) + \alpha_6NA - \alpha_8E_s. \quad (3)$$

Activated OT1 CTLs that reach the skin compartment (E_s) are modeled by (3). Antibodies in the skin compartment (A_s) have multiple positive effects on activated OT1 CTLs dynamics (E_s). One of these effects is represented by the ability of promoting E_s duplication. This is modeled through the Holling type II function $\alpha_7[A_s/(A_s + k_1)]E_s$, where α_7 is the maximum biological duplication rate of E_s and k_1 is a tuned threshold. When the number of A_s is high enough, the term $[A_s/(A_s + k_1)]$ tends towards 1, thus entitling maximum duplication rates for E_s . The term $\alpha_{11}E(t - \tau)$ is used to model migration of OT1 CTLs from the injection compartment to the skin compartment. We suppose here that migration from

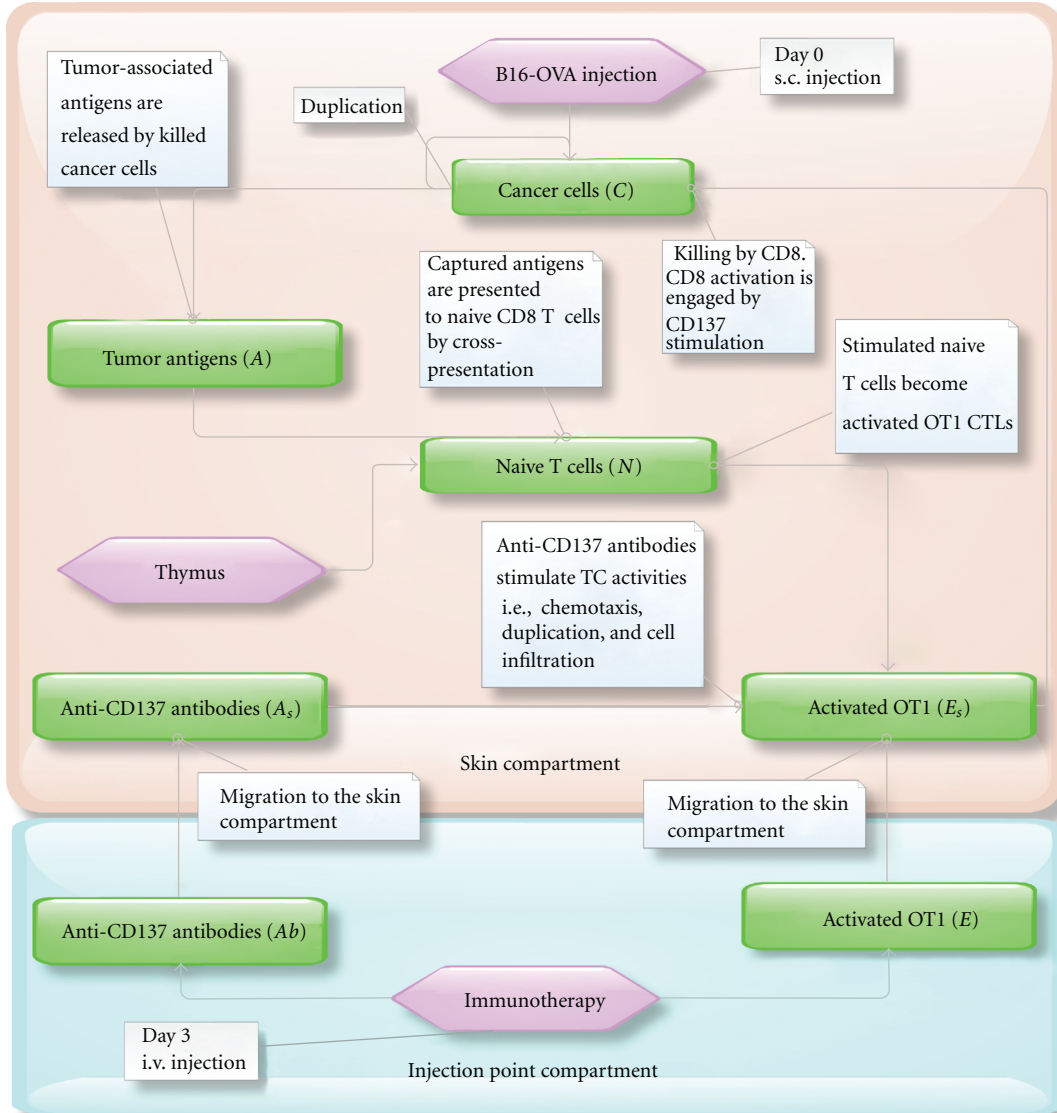


FIGURE 1: Conceptual model of the biological scenario. The model is composed by two compartments: the first compartment (bottom) where the treatment is administered, and the skin compartment (top) where the immune-system-melanoma competition occurs. Arrows are used to indicate the interaction between entities (i.e., the interaction between the antibodies and activated CTLs in the skin compartment), the change of a particular condition of an entity (i.e., the activation of naïve CTLs or the migration of antibodies from a compartment to another), the introduction and disappearing of entities (i.e., the production of newborn naïve CTLs by thymus or the disappearing of antigens that are presented to naïve CTLs). White boxes are used to better explain the meaning of the arrows. Both antibodies (Ab) and activated OT1 CTLs (E) migrate to the skin compartment. In the skin compartment, antibodies (A_s) stimulate duplication and infiltration into tumor mass of activated OT1 CTLs (E_s), which kill melanoma cells (C). Killed melanoma cells release antigens (A) that are captured by antigen presenting cells and presented to antigen-specific naïve OT1 CTLs (N). Naïve OT1 CTLs are then stimulated to become active CTLs (E_s).

the first compartment (E) to the second one (E_s) entitles a time delay of τ and occurs with a given rate α_{11} .

The term $\alpha_6 NA$ models the activation of naïve CTLs N thanks to the presence of antigens (A) released by killed cancer cells. The biological process that explains the presence of this term is summarized as follows. Antigenic sequences released by killed melanoma cells may be captured by antigen presenting cells (APC) such as macrophages and dendritic cells. These cells process the antigens and present them on their cellular surface to naïve CTLs (N). After this

presentation process, naïve CTLs cells may be activated, and if some complementary biological steps are accomplished (i.e., stimulation by cytokines released by T helper cells), they can become able to kill tumor cells. This process is not modeled in depth since it involves the modeling of other entities that are not considered fundamental for the problem. The number of newly activated OT1 CTLs is instead directly estimated on the basis of the quantity of released antigens. The last term ($-\alpha_8 E_s$) is used to take into account natural death of OT1 CTLs.

(4) Melanoma cells:

$$\frac{dC}{dt} = (\alpha_1 - \alpha_2 \ln(C)) \cdot C - \alpha_3 \left[\frac{A_s + k_2}{A_s + k_3} \right] E_s C. \quad (4)$$

Equation (4) describes the melanoma cells (C) behavior in the skin compartment. The first term $((\alpha_1 - \alpha_2 \ln(C)) \cdot C)$ represents a Gompertzian growth [14], whereas the second term denotes killing of C by activated OT1 CTLs that are already in the skin compartment (E_s). One of the most important actions accomplished by antibodies (A_s) is to boost chemotaxis sensitivity of CTLs (E_s) thus enabling better infiltration into the tumor mass. This translates into higher killing rates of melanoma cancer cells by activated CTLs (E_s). This is modeled through the term $-\alpha_3[(A_s + k_2)/(A_s + k_3)]E_s C$, where α_3 is the maximum killing rate of C by E_s , and k_2 and k_3 ($k_2 \ll k_3$) are tuned constants. When the number of A_s is high enough, the term $[(A_s + k_2)/(A_s + k_3)]$ tends towards 1, thus entitling maximum killing rates for E_s . In absence of antibodies, having $k_2 \ll k_3$, the term translates into $-\alpha_3 k_2/k_3 < \alpha_3$, which involves lower killing rates.

(5) Antigens:

$$\frac{dA}{dt} = \alpha_4 \left[\alpha_3 \left[\frac{A_s + k_2}{A_s + k_3} \right] E_s C \right] - \alpha_5 A - \alpha_6 NA. \quad (5)$$

With (5), we describe the tumor-associated antigen (A) dynamics. Antigens are released in the skin compartment by killed melanoma cells ($\alpha_4 \cdot [\alpha_3[(A_s + k_2)/(A_s + k_3)]E_s C]$) and are subject to natural degradation ($-\alpha_5 A$). They can also be captured by APC, which will present the antigen to naïve CTLs. As already stated in (3), capturing of the antigen by APC is not modeled and the number of captured antigens is estimated on the basis of naïve CTLs (N) that are activated by APC ($-\alpha_6 NA$).

(6) Naïve CTLs:

$$\frac{dN}{dt} = h(M - N) - \alpha_6 NA. \quad (6)$$

Equation (6) models the behavior of naïve OT1 CTLs (N). It is supposed here that these cells are already present in the skin compartment. The term $h(M - N)$ is used to model homeostasis. M is the number of circulating naïve CTLs under safe conditions given by the leukocyte formula. If switching of naïve CTLs to activated CTLs occurs, the number of naïve CTLs gets lower. As a consequence of that, the naïve population is repopulated with newborn cells and tends towards M at a rate h . The second term ($-\alpha_6 NA$) models the CTLs state changing from naïve to activated (E_s), thanks to presentation of the antigen by APC.

(7) Antibodies (skin compartment):

$$\frac{dA_s}{dt} = \alpha_{11} Ab(t - \tau) - \alpha_9 A_s E_s - \alpha_{10} A_s. \quad (7)$$

Antibodies that have reached the skin compartment (A_s) are modeled and described by (7). Antibodies in the skin compartment are supposed to be proportional to the number of antibodies in the injection point compartment (Ab) with a proportionality constant α_{11} and a time delay of τ . They also disappear by stimulating OT1 cells activities and are subject to a natural degradation ($-\alpha_9 A_s E_s$ and $-\alpha_{10} A_s$).

According to the considered cell populations and interactions, the mathematical model can be then represented by the following system of seven nonlinear delay differential equations:

$$\begin{aligned} \frac{dE}{dt} &= K_{in}(t, p) - \alpha_{11} E - \alpha_8 E, \\ \frac{dAb}{dt} &= K_{in}(t, q) - \alpha_{11} Ab - \alpha_{10} Ab, \\ \frac{dE_s}{dt} &= \alpha_7 \left[\frac{A_s}{A_s + k_1} \right] E_s + \alpha_{11} E(t - \tau) + \alpha_6 NA - \alpha_8 E_s, \\ \frac{dA_s}{dt} &= \alpha_{11} Ab(t - \tau) - \alpha_9 A_s E_s - \alpha_{10} A_s, \\ \frac{dN}{dt} &= h(M - N) - \alpha_6 NA, \\ \frac{dC}{dt} &= (\alpha_1 - \alpha_2 \ln(C)) \cdot C - \alpha_3 \left[\frac{A_s + k_2}{A_s + k_3} \right] E_s C, \\ \frac{dA}{dt} &= \alpha_4 \left[\alpha_3 \left[\frac{A_s + k_2}{A_s + k_3} \right] E_s C \right] - \alpha_5 A - \alpha_6 NA. \end{aligned} \quad (8)$$

Since we consider mainly populations that appear in the system as a consequence of treatment administrations (except for melanoma and naïve CTLs), the following Cauchy initial conditions have been set for the equations:

$$\begin{aligned} E(0) &= 0, \quad Ab(0) = 0, \quad E_s(0) = 0, \quad A_s(0) = 0, \quad A(0) = 0, \\ N(0) &= M, \quad C(0) = C_0. \end{aligned} \quad (9)$$

The physical time-step $\Delta(t)$ has been chosen equal to 8 hours, and the integration time has been then computed up to $10^2 \cdot \Delta(t) \approx 33$ days. The reason of this choice is biological, and it is given by the fact that in the in vivo experiment it is not possible to observe relevant biological phenomena in smaller time intervals. In particular, the minimum time required for cell division, which represents one of the most important biological phenomena, is usually not lower than 6–8 hours [15]. This may be not true in other in vivo setups, such as in case of allergies, where the time scale varies from seconds to minutes.

Some parameters appearing in the equations have been estimated from the literature (see Table 2), and from measurements made during the in vivo experiment.

In particular, melanoma growth rates have been estimated from diameter measurements made at different times in melanomas in five untreated mice. Melanomas have two growth phases, radial and vertical [16]. The first phase is represented by a radial growth, in which malignant cells grow in a radial fashion in the epidermis. At later stages,

TABLE 2: Model parameters. The “in vivo” label refers to parameters that have been chosen according to in vivo measurements and observations. The “Estimated” label refers to free (unknown) parameters that have been tuned.

Param.	Description	Value (estimate)	Ref.
α_1	C growth parameter (Gompertz)	$0.2165 \Delta(t)^{-1}$	in vivo
α_2	C shrink parameter (Gompertz)	$0.01269 \Delta(t)^{-1}$	in vivo
α_3	C max killing rate by E_s	$0.00000033 \Delta(t)^{-1}$	Estimated
α_4	A release rate by Killed C	$0.21 \Delta(t)^{-1}$	Estimated
α_5	A natural degradation rate	$\ln(2)/9 \Delta(t)^{-1}$	[19]
α_6	Switch rate from N to E_s thanks to A	$0.1 \Delta(t)^{-1}$	Estimated
α_7	E_s max duplication rate	$0.095 \Delta(t)^{-1}$	Estimated
α_8	E and E_s natural death rate	$\ln(2)/15 \Delta(t)^{-1}$	[20]
α_9	Ab death rate due to stimulation of E_s	$0.000001 \Delta(t)^{-1}$	Estimated
α_{10}	Ab and A_s natural degradation rate	$\ln(2)/21 \Delta(t)^{-1}$	[21, 22]
α_{11}	migration rate from injection to skin compartment	$0.009 \Delta(t)^{-1}$	Estimated
h	Reinjection rate of N by thymus	$0.01 \Delta(t)^{-1}$	Estimated
k_1	E_s duplication threshold due to A_s	10	Estimated
k_2	C- E_s min. killing rate threshold	1	Estimated
k_3	C- E_s max. killing rate threshold	50	Estimated
M	Number of N in safe conditions (leukocyte formula)	196000	in vivo
C_0	Initial number of C	180000	in vivo
p	No. of injected E by treatment administration	760000	in vivo
q	No. of injected Ab by treatment administration	1000000	in vivo
τ	Delay value	1	in vivo

most melanomas progress to the vertical growth phase, in which the malignant cells invade the dermis and develop the ability to metastasize. In this case, we supposed that only the radial growth phase is involved. By supposing a disk-shaped layout for the melanoma and having knowledge of the mean diameter of melanoma cancer cells, the number of cancer cells (in the observed melanomas) has been estimated for all the measurements made. This data has been used with a curve fitting procedure to estimate the unknown parameters needed to model the cancer growth kinetics under the hypothesis of a Gompertzian growth for the tumor, used successfully in our previous experience [13, 17, 18]. The Gompertz law, which is commonly considered suitable for describing populations growths, uses two factors: a constant growth term and a shrink term that increases in time and is related to antiangiogenic factors, giving as a result a sigmoid shape to the curve. The initial number of injected cancer cells C_0 , the number of injected OT1 CTLs and antibodies (p and q), and the number of antigen-specific naïve OT1 CTLs under safe conditions (M) have been chosen into reasonable ranges given by in vivo measurements.

Remaining parameters have been chosen in plausible biological ranges in such a way to reproduce the set of experimental data for the activated OT1 CTLs + Anti-CD37 Ab combined treatment, and counterchecked against the other vaccine scenarios taken into account (Table 2).

4. Results

To reproduce the dynamics of the model, we took into account four treatments that have been tested in vivo:

untreated (control), in vitro activated OT1 CTLs, Anti-CD137 monoclonal antibodies, and in vitro activated OT1 CTLs + Anti-CD137 monoclonal antibodies.

Among such treatments, only the last one (treated with activated CTLs + Anti-CD137 monoclonal antibodies) showed complete eradication of the tumor burden, whereas the other treatments remained almost ineffective.

Entities behaviors for all the analyzed treatments are shown in Figure 2. In absence of therapy (blue dashed line), there is no induced immune response and thus the number of melanoma cells grows without any intervention from IS cells, whose plots remain flat.

The same scenario arises when the Anti-CD137 monoclonal antibodies treatment is administered (see Figure 2, green dotted lines). The mechanism that triggers the IS response is driven by the presence of activated OT1 CTLs that can kill melanoma cells, which release antigens able to further stimulate the IS response.

This fact can be partially seen if the treatment based upon the administration of in vitro activated OT1 CTLs is used (Figure 2, red dot-dashed lines). The E_s plots show some evidence of activated OT1 CTLs in the skin. These cells are able to kill melanoma cells (C), which release antigens (A) that are captured by APCs and then used to promote the differentiation of newborn naïve CTLs (N) to activated OT1 CTLs (E_s). However, in absence of Anti-CD137 antibodies, which promote both duplication and infiltration into tumor masses of activated OT1 CTLs, recruitment of newborn naïve CTLs is too bland and tardy to stimulate an IS response able to stop the melanoma.

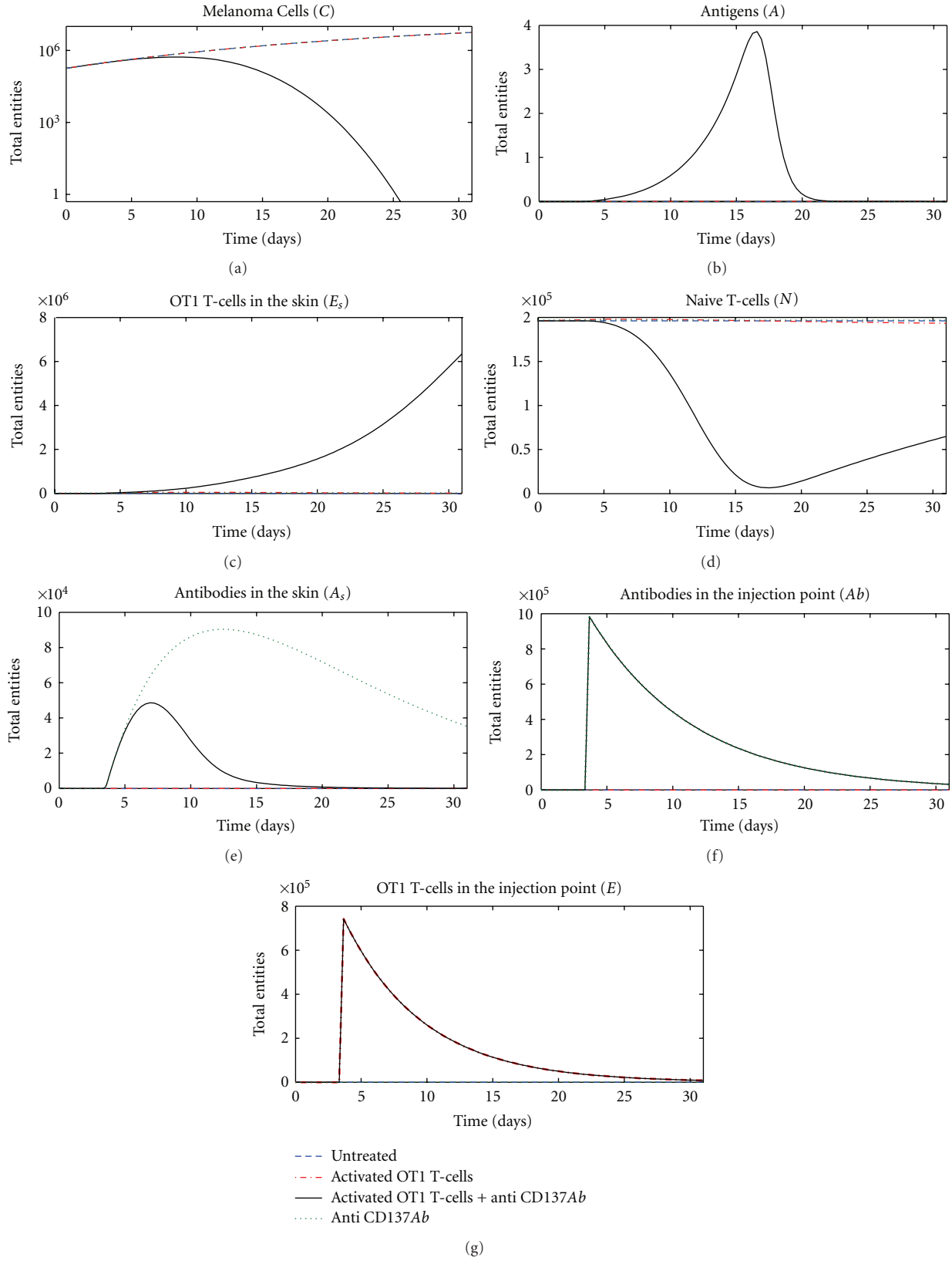


FIGURE 2: System behavior obtained with the use of different vaccination protocols: untreated (blue dashed line), activated OT1 CTLs (red dot-dashed lines), Anti-CD137 monoclonal antibodies (green dotted lines), and activated OT1 CTLs + Anti-CD137 monoclonal antibodies (black solid lines). From left to right, top to bottom: melanoma cells (C), tumor antigens (A), activated OT1 CTLs in the skin (E_s), naïve CTLs (N), antibodies in the skin (A_s), antibodies in the injection point (Ab), and activated OT1 CTLs in the injection point (E).

Only the combined action of activated CTLs + Anti-CD137 monoclonal antibodies is able to contrast the melanoma growth (see Figure 2, black solid line). In this case, both Anti-CD137 antibodies (Ab) and activated OT1 CTLs (E) are injected at day three and then migrate to the skin compartment. Activated OT1 CTLs (E_s) are stimulated to duplicate and to infiltrate into tumor masses thanks to the presence of antibodies in the skin compartment (A_s). As a consequence of this, many more melanoma cells (C) are killed, and copious number of antigens (A) is released, thus promoting the activation of naïve CTLs (N) to activated OT1 CTLs (E_s), which further act against melanoma.

To qualitatively compare the model results with the in vivo data, we estimated (using the number of cancer cells) the melanoma surface given by the mathematical model under the same assumptions made for estimating the Gompertz growth parameters. We then compared the time evolution of the melanoma surface given by the mathematical model with the mean surface observed in the in vivo experiment for the following cases: the untreated (control) case and the activated CTLs + Anti-CD137 monoclonal antibodies combined treatment case. The other cases are not presented since they give back the same scenario observed in the untreated case for both the experiments.

Comparison for the untreated case is shown in Figure 3(a). As expected, since we only observe the melanoma growth, the mathematical model perfectly reproduces the in vivo setup. Comparison for the combined treatment case is shown in Figure 3(b). The mean in vivo melanoma behavior is well reproduced by the mathematical model that is able to quantitatively and qualitatively represent the shape of the curve observed in the in vivo experiments. In Figures 3(c) and 3(d), we show absolute and relative differences between in silico and in vivo measurements for the untreated and activated OT1 CTLs + Anti-CD137 combined treatments, respectively. Relative differences are computed using the following metric: $d(x, y) = |x - y| / (1/2(|x| + |y|))$.

It must be noted here that the initial gap between the mathematical model and the in vivo experiment measurements visible in Figures 3(b) and 3(d) is mainly due to the different nature of measurements. In the simulations, the total number of cells is always known and it is used to estimate the melanoma surface. In the in vivo experiment, melanoma surface is instead measured on mice skin. Even if the injection of tumor cells is done at time 0, melanoma needs some time to arise and become visible even if the melanoma cells are all already present in mice.

5. Sensitivity Analysis

To understand how the system varies under different parameter values, it is important to analyze the sensitivity of the model to variation of parameters. Classical sensitivity analysis is done usually by varying a given parameter in reasonable ranges and keeping the other ones fixed. The results obtained are obviously dependent on the values of the fixed parameters, and different sets of values may entitle completely different results.

In order to overcome the limits of classical sensitivity analysis, many techniques have been developed. One of these is represented by Partial rank correlated coefficients (PRCC) [23], a statistical sensitivity analysis technique, which computes a partial correlation on rank-transformed data between input and output values, represented in this case by the model parameters (input) and the model entities behaviors (output).

It important to note here that the obtained correlation indexes do not depend on a given set of parameters, and it is therefore possible to estimate how the variations of a parameter may influence the results of the model, no matter what the value of the other parameters is. PRCC returned values varying in $[-1, 1]$ and estimated the correlation between input and output parameters. A value near 1 suggests a high (linear) positive correlation, whereas a value near -1 indicates a negative correlation. Values around 0 usually indicate little or no correlation.

Using this methodology in conjunction with the Latin Hypercube Sampling (LHS), which is used to sample the parameters' space, we analyze the effects of the input parameters most influencing the growth of cancer cells (C). We plot PRCCs versus the experiment time for the most important parameters to see how the sensitivity of parameters changes as the system dynamics progresses.

5.1. Impact Variation of the Treatment Quantities p and q on the Number of Melanoma Cells. The two parameters p and q refer to the number of activated OT1 effector cells (E) and Anti-CD137 antibodies (Ab) injected as a single boost treatment against the melanoma, according to the in vivo experiment. In Figure 4, we show the PRCC time plots for the two parameters. As expected, just after the injection of the treatment, both the two parameters show a negative correlation with the number of cancer cells. It is worth to note that p shows good correlation in particular in the first ten days, whereas a weaker and almost constant correlation is related to q . This may suggest that the effects of the treatment are mainly driven by the OT1 effector cells and, even if antibodies are needed to obtain protection (as discussed earlier and shown in Figure 2), a reduction in their quantity may entitle similar treatment effectiveness.

5.2. Impact of Naïve OT1 CTLs Initial Number (M) and Recovery Rate (h) on the Number of Cancer Cells. The M parameter indicates the initial number of antigen-specific naïve CTLs in the host, and the h parameter represents the rate of newborn naïve CTLs generated by thymus selection. The M parameter negatively correlates over time with the number of melanoma cells (Figure 5(a)), thus confirming that the action of naïve OT1 T cells induced by the treatment administration is fundamental for treatment effectiveness. Surprisingly it seems that the variation of the rate of introduced newborn naïve CTLs does not influence the number of melanoma cells, since no correlation is shown over time (see Figure 5(b)).

5.3. Impact of Activated OT1-T-Related Parameters on the Number of Cancer Cells. The activated OT1 CTLs in the skin

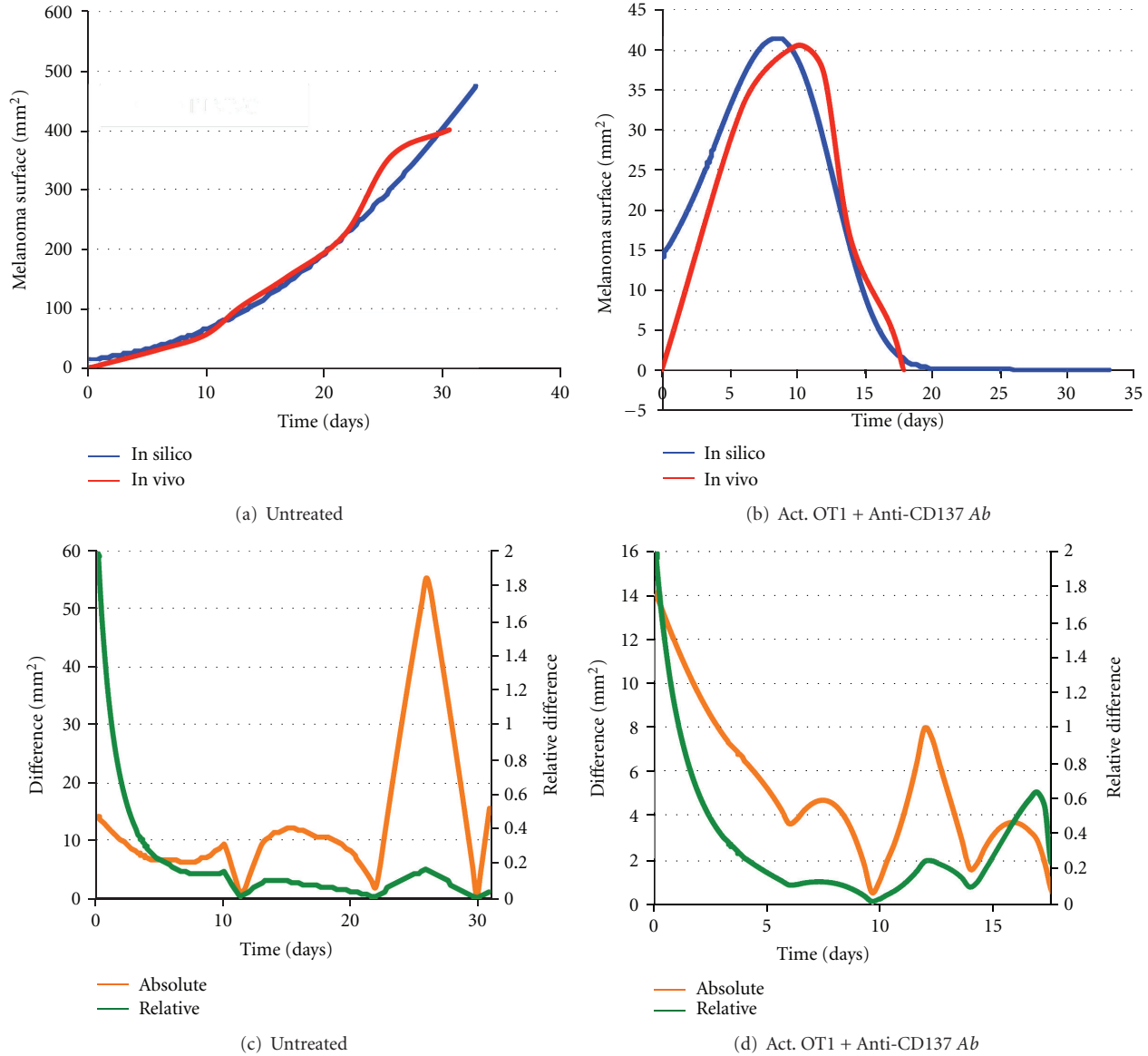


FIGURE 3: Comparison of melanoma surface (mm^2) behavior over time between mean in vivo measurements (red lines) and simulations (blue lines). (a) Comparison for the untreated case (no vaccination). (b) Comparison under the administration of the combined activated OT1 CTLs + Anti-CD137 monoclonal antibodies treatment. In silico melanoma surfaces have been estimated from the total number of melanoma cells by assuming only radial growth and a disk-shaped layout for the melanoma. (c) Absolute (orange line) and relative (green line) differences between in vivo and in silico measurements for the untreated case (no vaccination). (d) Absolute (orange line) and relative (green line) differences between in vivo and in silico measurements under the administration of the combined activated OT1 CTLs + Anti-CD137 monoclonal antibodies treatment.

(E_s) represent the number of entities that are directly able to kill melanoma tumor cells. It is, therefore, trivial to see that α_3 and α_8 , which represent the rate of killed melanoma cells by activated OT1 effector cells and the half-life of OT1 effector cells, have a strong negative and positive correlation with the number of cancer cells, respectively, (see Figures 6(a) and 6(b)). A negative correlation is also present for α_7 , which represents the maximal duplication rate of (E_s) (see Figure 6(c)). However, in this case the correlation remains weaker, thus suggesting how small variations on the cells duplication rates, which can be associated with individual

diversity, do not influence considerably the total behavior of cancer cells.

5.4. Impact of Antibody-Related Parameters on the Number of Cancer Cells. The α_4 parameter is used to represent the rate of antigens released by killed C, whereas the α_5 represents the specific antigen half-life. If the former has a strong negative PRCC correlation with the number of C (Figure 7(a)), particularly in the first period just after treatment administration, the latter interestingly seems to be not correlated with the number of C (Figure 7(b)).

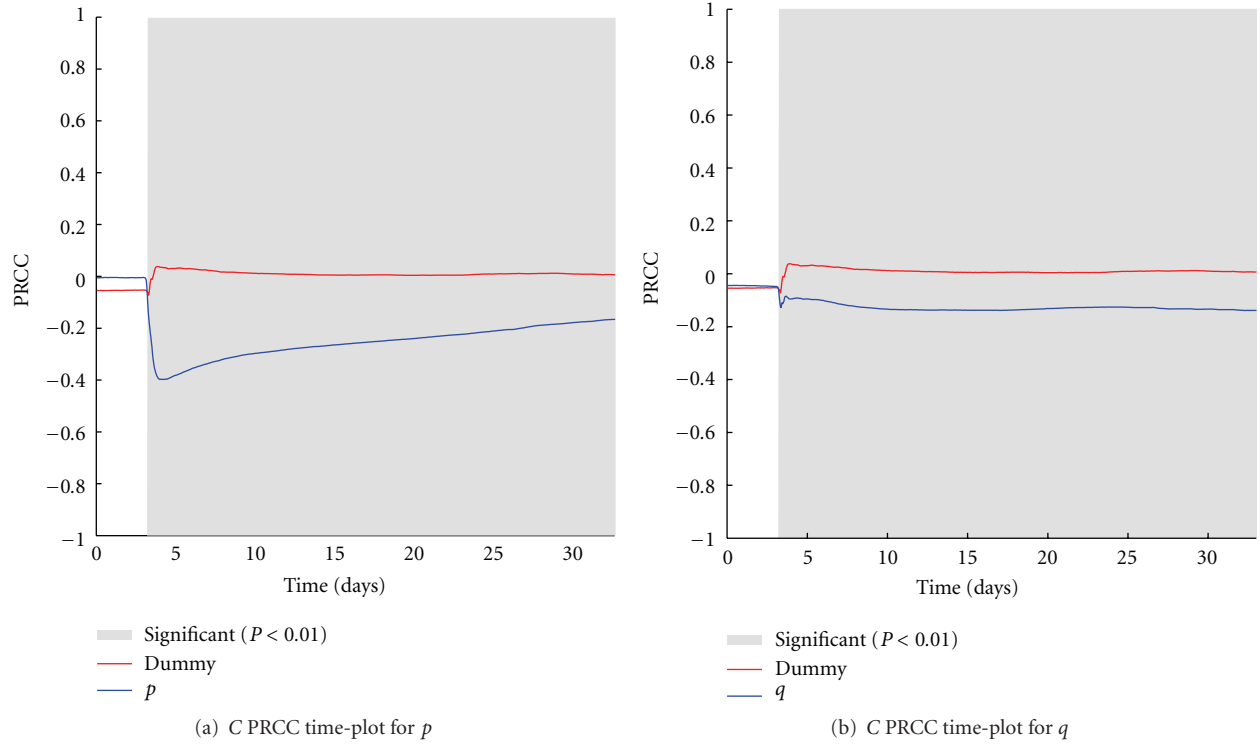


FIGURE 4: p (a) and q (b) PRCC plots computed on C . PRCC values are calculated with respect to the number of melanoma cells (C), plotted over time (blue lines). PRCC time plot of Dummy parameter (red lines) is shown for comparison. Greyed areas represent the plot portions where correlation is significant ($P < 0.01$).

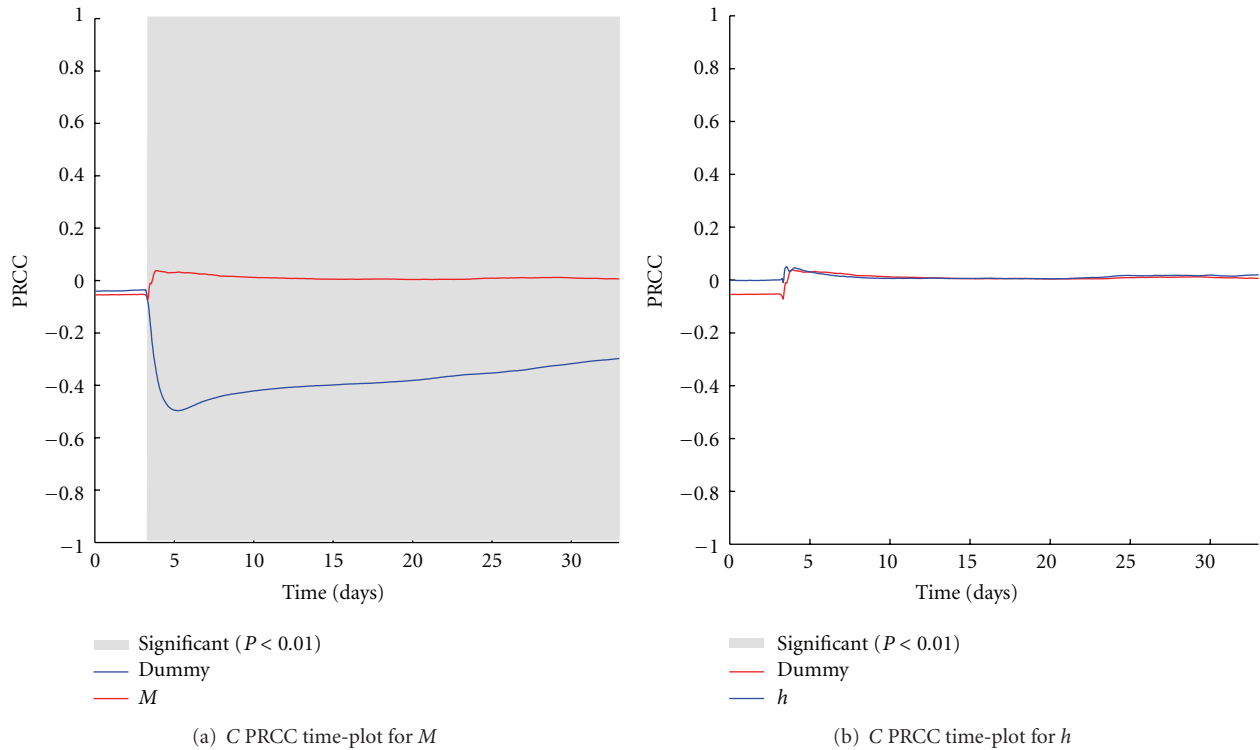


FIGURE 5: M (a) and h (b) PRCC plots computed on C . PRCC values are calculated with respect to the number of melanoma cells (C), plotted over time (blue lines). PRCC time plot of Dummy parameter (red lines) is shown for comparison. Greyed areas represent the plot portions where correlation is significant ($P < 0.01$).

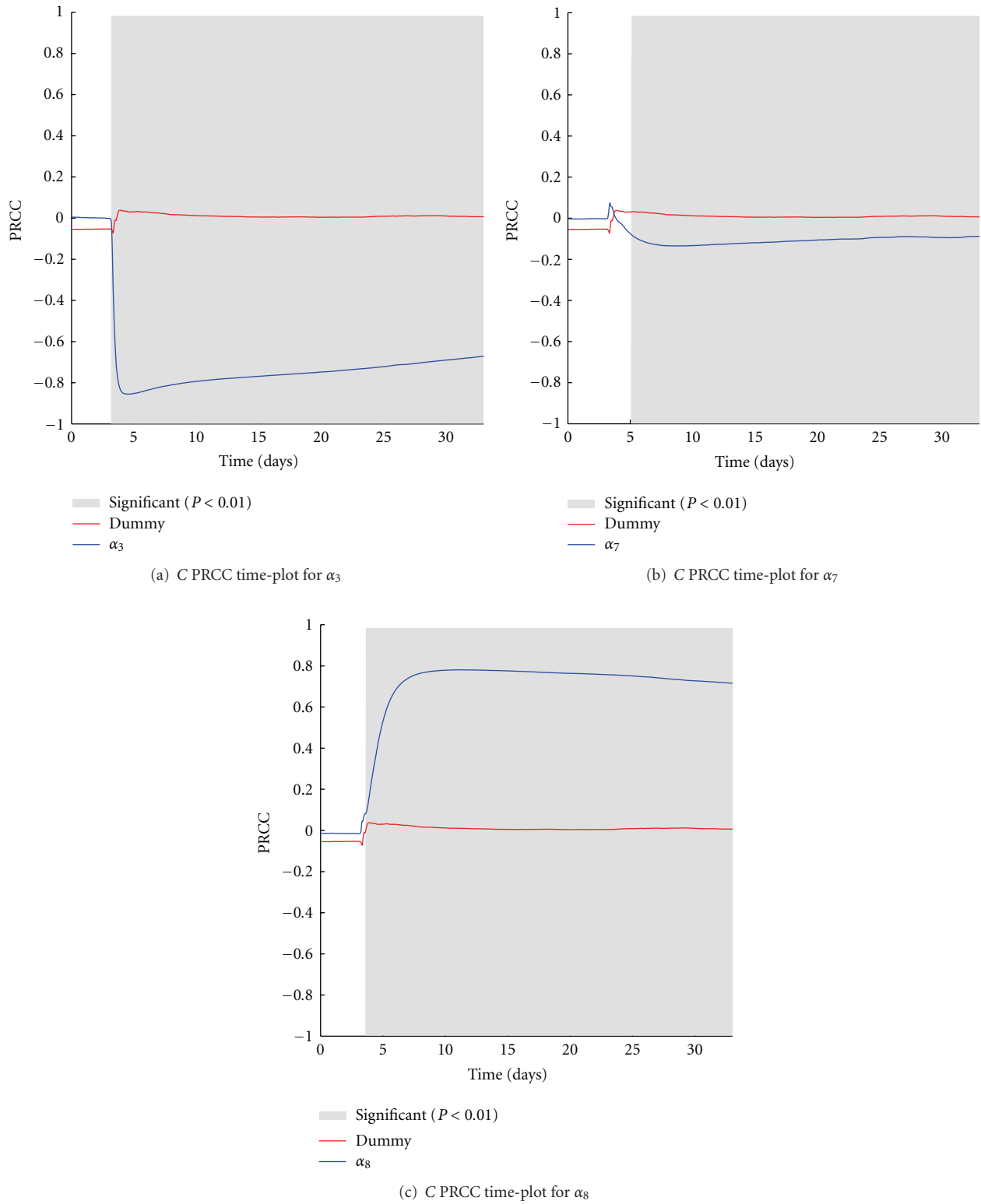


FIGURE 6: α_3 (a), α_7 (b), and α_8 (c) PRCC plots computed on C . PRCC values are calculated with respect to the number of melanoma cells (C), plotted over time (blue lines). PRCC time plot of Dummy parameter (red lines) is shown for comparison. Greyed areas represent the plot portions where correlation is significant ($P < 0.01$).

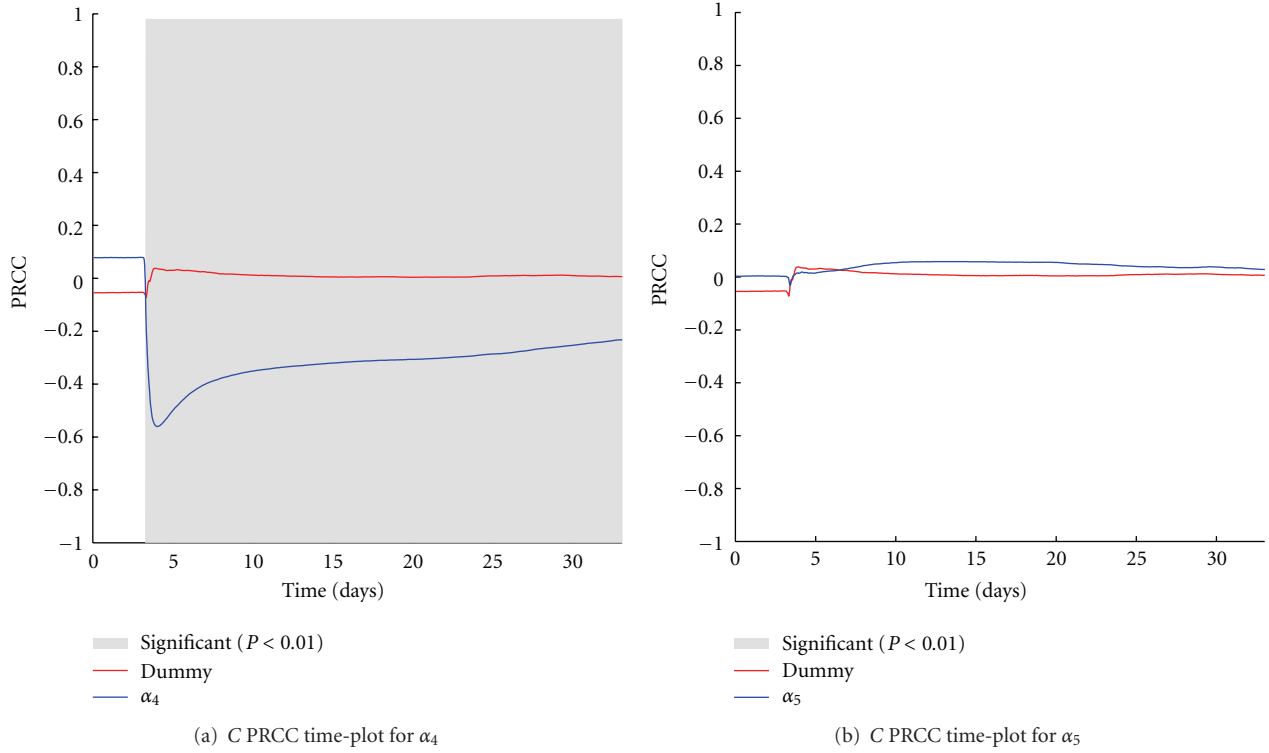


FIGURE 7: α_4 (a) and α_5 (b) PRCC plots computed on C . PRCC values are calculated with respect to the number of melanoma cells (C), plotted over time (blue lines). PRCC time plot of Dummy parameter (red lines) is shown for comparison. Greyed areas represent the plot portions where correlation is significant ($P < 0.01$).

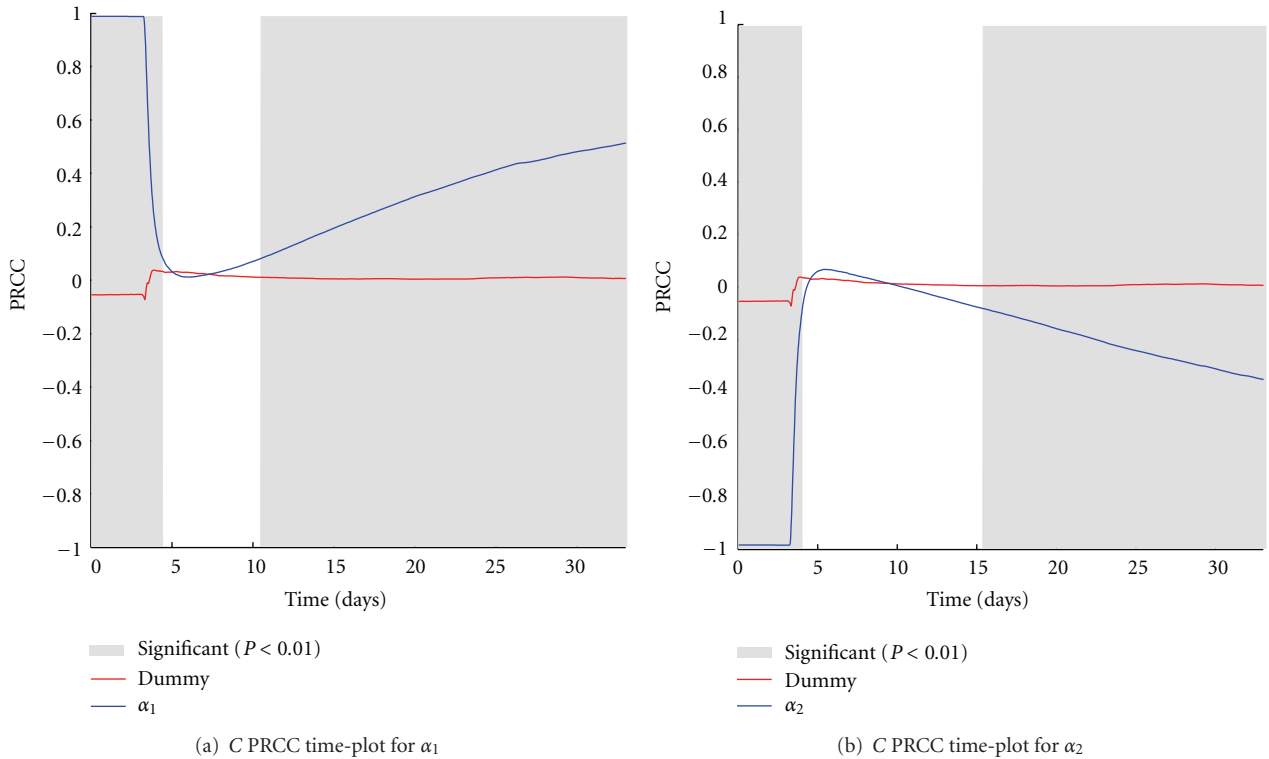


FIGURE 8: α_1 (a) and α_2 (b) PRCC plots computed on C . PRCC values are calculated with respect to the number of melanoma cells (C), plotted over time (blue lines). PRCC time plot of Dummy parameter (red lines) is shown for comparison. Greyed areas represent the plot portions where correlation is significant ($P < 0.01$).

5.5. Impact of the Tumor Growth and Shrink Parameters (α_1 and α_2) on the Number of Cancer Cells. The α_1 and α_2 parameters represent the Gompertz growth parameters used to model the growth of melanoma. The range of variation for these two parameters has been set equal to the confidence range given by the curve fitting procedure used to estimate the parameters' values from in vivo measurements. In this way, we reasonably take into account the possible melanoma growths that may also be observed in the in vivo experiments. PRCC plots over time are represented in Figures 8(a) and 8(b). Even if positive and negative PRCC correlations are somewhat expected, there is a small time window just after the treatment injection time where no correlation occurs. This may be explained by the fact that variations of the melanoma growth rate do not influence substantially (at least initially) the effectiveness of the treatment.

6. Conclusions

We presented a mathematical model, which reproduces the immune response against B16-melanoma induced by the combined administration of activated OT1 CTLs and Anti-CD 137 immunostimulatory monoclonal antibodies. The model uses delay differential equations to reproduce the presence of two different compartments: the injection point compartment where the treatment is administered, and the skin compartment, where the melanoma-Immune system competition occurs.

The model proved to be able to coherently reproduce the in vivo experiment results obtained with four vaccination strategies (untreated, only activated OT1 CTLs, only monoclonal Ab, OT1 CTLs + monoclonal Ab). Moreover, the model is able to qualitatively and quantitatively reproduce the time dynamics of melanoma under the administration of the combined treatment. Results show that activated CTLs + Anti-CD137 monoclonal combined treatment acts in two ways: directly by activated OT1 CTLs that are able to kill melanoma and antibodies that boost CTLs activities and indirectly by promoting activation of naïve OT1 CTLs thanks to the releasing of melanoma cells antigens.

Among some useful findings, sensitivity analysis underlined the important role of activated OT1 cytotoxic treatment, suggesting that it would be in principle possible to obtain similar effectiveness lowering the number of administered antibodies, which, however, remain fundamental to gain effectiveness. Such kind of suggestions may be useful for optimizing treatment effectiveness and minimizing the risk of side effects.

Future work will be focused on studying analytically a simplified model without delay and in comparing the obtained results with Sim-B16, an agent-based model developed to reproduce the same in vivo experiment [13].

Acknowledgments

The paper was partially supported by the INDAM-GNFM-Young Researchers Project-prot.n.43-Mathematical Modelling for the Cancer-Immune System Competition Elicited by a Vaccine and by University of Catania under PRA grant.

The author would like to thank Professor I. Melero and coworkers for supplying data.

References

- [1] R. A. Morgan, M. E. Dudley, J. R. Wunderlich et al., "Cancer regression in patients after transfer of genetically engineered lymphocytes," *Science*, vol. 314, no. 5796, pp. 126–129, 2006.
- [2] S. A. Rosenberg, N. P. Restifo, J. C. Yang, R. A. Morgan, and M. E. Dudley, "Adoptive cell transfer: a clinical path to effective cancer immunotherapy," *Nature Reviews Cancer*, vol. 8, no. 4, pp. 299–308, 2008.
- [3] I. Melero, I. Martinez-Forero, J. Dubrot, N. Suarez, A. Palazón, and L. Chen, "Palettes of vaccines and immunostimulatory monoclonal antibodies for combination," *Clinical Cancer Research*, vol. 15, no. 5, pp. 1507–1509, 2009.
- [4] J. L. Perez-Gracia, P. Berraondo, I. Martinez-Forero et al., "Clinical development of combination strategies in immunotherapy: are we ready for more than one investigational product in an early clinical trial?" *Immunotherapy*, vol. 1, no. 5, pp. 845–853, 2009.
- [5] I. Tirapui, A. Arina, G. Mazzolinii et al., "Improving efficacy of interleukin-12-transfected dendritic cells injected into murine colon cancer with anti-CD137 monoclonal antibodies and alloantigens," *International Journal of Cancer*, vol. 110, no. 1, pp. 51–60, 2004.
- [6] I. Tirapu, E. Huarte, C. Guiducci et al., "Low surface expression of B7-1 (CD80) is an immunoescape mechanism of colon carcinoma," *Cancer Research*, vol. 66, no. 4, pp. 2442–2450, 2006.
- [7] A. Palazón, A. Teijeira, I. Martínez-Forero et al., "Agonist anti-CD137 mAb act on tumor endothelial cells to enhance recruitment of activated T lymphocytes," *Cancer Research*, vol. 71, no. 3, pp. 801–811, 2011.
- [8] I. Melero, O. Murillo, J. Dubrot, S. Hervás-Stubbs, and J. L. Perez-Gracia, "Multi-layered action mechanisms of CD137 (4-1BB)-targeted immunotherapies," *Trends in Pharmacological Sciences*, vol. 29, no. 8, pp. 383–390, 2008.
- [9] J. Dubrot, F. Milheiro, C. Alfaro et al., "Treatment with anti-CD137 mAbs causes intense accumulations of liver T cells without selective antitumor immunotherapeutic effects in this organ," *Cancer Immunology, Immunotherapy*, vol. 59, no. 8, pp. 1223–1233, 2010.
- [10] I. Melero, S. Hervas-Stubbs, M. Glennie, D. M. Pardoll, and L. Chen, "Immunostimulatory monoclonal antibodies for cancer therapy," *Nature Reviews Cancer*, vol. 7, no. 2, pp. 95–106, 2007.
- [11] F. Ito, Q. Li, A. B. Shreiner et al., "Anti-CD137 monoclonal antibody administration augments the antitumor efficacy of dendritic cell-based vaccines," *Cancer Research*, vol. 64, no. 22, pp. 8411–8419, 2004.
- [12] K. F. May Jr., L. Chen, P. Zheng, and Y. Liu, "Anti-4-1BB monoclonal antibody enhances rejection of large tumor burden by promoting survival but not clonal expansion of tumor-specific CD8⁺ T cells," *Cancer Research*, vol. 62, no. 12, pp. 3459–3465, 2002.
- [13] F. Pappalardo, I. M. Forero, M. Pennisi, A. Palazon, I. Melero, and S. Motta, "SimB16: modeling induced immune system response against B16-melanoma," *PLoS ONE*, vol. 6, no. 10, Article ID e26523.
- [14] A. K. Laird, "Dynamics of tumor growth," *British Journal of Cancer*, vol. 13, pp. 490–502, 1964.
- [15] J. M. Mitchison, *The Biology of the Cell Cycle*, Cambridge University Press, 1971.

- [16] W. H. Clark, A. M. Ainsworth, E. A. Bernardino, C. H. Yang, C. M. Mihm, and R. J. Reed, "The developmental biology of primary human malignant melanomas," *Seminars in Oncology*, vol. 2, no. 2, pp. 83–103, 1975.
- [17] M. Pennisi, F. Pappalardo, and S. Motta, "Agent based modeling of lung metastasis-immune system competition," *Lecture Notes in Computer Science*, vol. 5666, pp. 1–3, 2009.
- [18] M. Pennisi, F. Pappalardo, A. Palladini et al., "Modeling the competition between lung metastases and the immune system using agents," *BMC Bioinformatics*, vol. 11, supplement 7, article S13, 2010.
- [19] Y. Lotan and C. G. Roehrborn, "Clearance rates of total prostate specific antigen (PSA) after radical prostatectomy in African-Americans and Caucasians," *Prostate Cancer and Prostatic Diseases*, vol. 5, no. 2, pp. 111–114, 2002.
- [20] D. Pardoll, "T cells take aim at cancer," *Proceedings of the National Academy of Sciences of the United States of America*, vol. 99, no. 25, pp. 15840–15842, 2002.
- [21] J. V. Peppard and E. Orlans, "The biological half-lives of four rat immunoglobulin isotypes," *Immunology*, vol. 40, no. 4, pp. 683–686, 1980.
- [22] H. Narazaki, Y. Zhu, L. Luo, G. Zhu, and L. Chen, "CD137 agonist antibody prevents cancer recurrence: contribution of CD137 on both hematopoietic and nonhematopoietic cells," *Blood*, vol. 115, no. 10, pp. 1941–1948, 2010.
- [23] S. Marino, I. B. Hogue, C. J. Ray, and D. E. Kirschner, "A methodology for performing global uncertainty and sensitivity analysis in systems biology," *Journal of Theoretical Biology*, vol. 254, no. 1, pp. 178–196, 2008.